

REPORT DOCUMENTATION PAGE

AFRL-SR-BL-TR-00-

18

Public reporting burden for this collection of information is estimated to average 1 hour per response, including gathering and maintaining the data needed, and completing and reviewing the collection of information, including suggestions for reducing this burden, to Washington Headquarters, Davis Highway, Suite 1204, Arlington, VA 22202-4302, and to the Office of Management and Budget, Paperwork Project, Washington, DC 20503.

0143

ing data sources,
er aspect of this
s, 1215 Jefferson

1. AGENCY USE ONLY (Leave Blank)		2. REPORT DATE 2/22/99		3. REPORT TYPE AND DATES COVERED Final Report for period 15 Jun 96 thru 31 May 98	
4. TITLE AND SUBTITLE Improved Prediction and Characterization of Contrails and Optically-Thin Cirrus				5. FUNDING NUMBERS P.I.N.: F49620-96-C-0024	
6. AUTHORS Andrew J. Heymsfield Larry Miloshevich					
7. PERFORMING ORGANIZATION NAME(S) AND ADDRESS(ES) University Corporation for Atmospheric Research/National Center for Atmospheric Research P.O. Box 3000 Boulder, CO 80307-3000				8. PERFORMING ORGANIZATION REPORT NUMBER Final Technical Report	
9. SPONSORING / MONITORING AGENCY NAME(S) AND ADDRESS(ES) USAF, AFMC Air Force Office of Scientific Research 110 Duncan Avenue, Suite B115 Bolling AFB, DC 20332-8080				10. SPONSORING / MONITORING AGENCY REPORT NUMBER	
11. SUPPLEMENTARY NOTES					
12a. DISTRIBUTION / AVAILABILITY STATEMENT Results of this research are published in peer-reviewed scientific journals and are in the public domain				12b. DISTRIBUTION CODE	
13. ABSTRACT (Maximum 200 words) This report summarizes research and results that pertain to AFOSR agreement no. F49620-96-C-0024. The aim of this research program has been to improve prediction of aircraft contrail and cirrus cloud formation, and to improve understanding of their optical and physical properties. Toward this end, the investigators have used analysis of data from research aircraft, balloon-borne ice crystal replicator sondes, and radiosonde relative humidity measurements, as well as theoretical and numerical modeling techniques. The five categories of research covered in this report are: <ol style="list-style-type: none"> 1) Improving Vaisala RS80-A radiosonde relative humidity measurements 2) Vertical distribution of cirrus microphysical and optical properties 3) Relative humidity conditions for the formation of cirrus and contrails 4) Variability of cirrus microphysical properties 5) Improved theory of contrail formation Research findings in each of these five categories resulted in at least one publication whose full or partial sponsorship by the AFOSR was acknowledged. The journal publications provide an in-depth discussion of the research conducted; this final report summarizes the findings.					
14. SUBJECT TERMS Vaisala RS80-A radiosonde measurements, cirrus microphysical properties, contrails formation				15. NUMBER OF PAGES 41 + reprints of publications	
				16. PRICE CODE	
17. SECURITY CLASSIFICATION OF REPORT UNCLASSIFIED	18. SECURITY CLASSIFICATION OF THIS PAGE UNCLASSIFIED	19. SECURITY CLASSIFICATION OF ABSTRACT UNCLASSIFIED	20. LIMITATION OF ABSTRACT UL		

NSN 7540-01-280-5500

Standard Form 298 (Rev. 2-89)
Prescribed by ANSI Std. Z39-1
298-102

DISTRIBUTION STATEMENT A
Approved for Public Release
Distribution Unlimited

22 February 1999

Major Paul Bellaire
AFOSR/NM
801 N Randolph Street, Rm 732
Arlington, VA 22203-1977

Dear Major Bellaire:

Attached is our final report on research accomplished under the proposal "Improved Prediction and Characterization of Contrails and Optically-Thin Cirrus" (grant F49620-96-C-0024), which I am submitting on behalf of Andy Heymsfield, who is currently engaged in a field experiment. The report explains our primary results, and copies or reprints of papers whose research was partially or fully supported by the AFOSR are attached. We hope you will agree that we have used our AFOSR funding productively.

I would like to specifically point out that result #1 in this report has immediate and practical use, in case you wish to forward the results to the appropriate person for implementation. We have developed corrections for relative humidity measurements from Vaisala RS80-A radiosondes (which is the type used by the AF). The measurement errors are substantial at cold temperatures, and our paper (currently in progress) explains the source of these errors and how to apply corrections that substantially improve their accuracy. The implications for operational contrail prediction (as well as other areas) are significant. I cannot send the full text of this paper immediately because it is not quite complete, but will send you a copy of the paper at the same time it is submitted for publication (in the next month or so). At that time I will also describe to you my ideas for helping the AF implement these corrections for both past and present radiosonde humidity measurements, as well as my ideas for pursuing correction of the remaining (but well-understood) measurement errors from these radiosondes.

We thank you for supporting our research, and particularly for your patience concerning preparation of this report. You will notice several areas in this report where further research would lead to significant results, and should the AFOSR be interested, we would be happy to discuss these areas and/or write a specific research proposal. Hopefully our mutual research interests will overlap again in the future.

Sincerely,



Larry Miloshevich

20000420 153

Final Report

Improved Prediction and Characterization of Contrails and Optically-Thin Cirrus

Andrew J. Heymsfield, Ilia P. Mazin, Larry M. Miloshevich, and Samuel J. Oltmans

This report summarizes research and results that pertain to AFOSR grant F49620-96-C-0024. The funding period of this grant was shortened from three years to two years as a result of changing priorities at AFOSR, and therefore the research conducted is a subset of that in our original proposal, as described in the document "Revised Statement of Work." This report summarizes our primary results. Attached are publications that resulted from AFOSR-sponsored research.

The aim of our research program has been to improve prediction of aircraft contrail and cirrus cloud formation, and to improve understanding of their optical and physical properties. Toward this end, we have used analysis of data from research aircraft, balloon-borne ice crystal replicator sondes, and radiosonde relative humidity measurements, as well as theoretical and numerical modeling techniques. Five categories of research are described below, each of which resulted in at least one publication whose full or partial sponsorship by the AFOSR was noted (papers are attached). These papers give an in-depth discussion of our research, but the results are summarized below.

1. Improving Vaisala RS80-A Radiosonde Relative Humidity Measurements

Through the combination of collaboration with Vaisala and analysis of a unique dataset we have identified the sources of relative humidity (RH) measurement error from Vaisala RS80-A radiosondes at temperatures below 0°C, and we have developed functional corrections for the errors. The RS80-A is the most widely used radiosonde in the world, including by the Air Force, and in addition to operational use of the measurements a large historical database exists. An introduction to these measurement errors titled "Undermeasurement of High Relative Humidities in the Upper Troposphere by Vaisala RS80-A Radiosondes" was presented at the 10th AMS Symposium on Meteorological Observations and Instrumentation (reprint enclosed). After the end of our AFOSR funding we continued this research because a unique opportunity arose to collaborate with the sensor designer at Vaisala, and in combination with our observational dataset we have nearly completed a joint paper which is by far the most thorough investigation of this sensor available, titled "Characterization and Correction of Relative Humidity Measurements from Vaisala RS80-A Radiosondes at Temperatures Below 0°C." Because this information is of immediate and practical use to the Air Force, a copy of this paper will be forwarded as soon as it is completed and submitted to the *Journal of Atmospheric and Oceanic Technology*. It will be apparent to the reader that this information has significant implications for the operational prediction of contrail formation, in addition to numerous other

areas such as climate research and validation of remote sensor retrievals.

This study was conceived following the 1991 NASA/FIRE-II experiment when the Vaisala RS80-A measurements in the upper levels of cirrus clouds were substantially below saturation with respect to ice (RH_i). These measurements were inconsistent with simultaneous collections of ice crystals from a balloon-borne Formvar replicator, which showed pristine ice crystal shapes with sharp edges indicating active ice crystal growth in an ice-supersaturated environment. Figure 1.1 shows simultaneous RH profiles from the NOAA cryogenic frost-point hygrometer and two RS80-A radiosondes. The measurement of ice-supersaturation by the hygrometer is consistent with the sharp-edged ice crystals measured simultaneously by the replicator in the upper portion of the cloud, as well as with ice-subsaturation in the lower portion of the cloud as indicated by the rounded and sublimating crystals. Radiosondes cannot measure ice-supersaturation because the surface of the sensor acts as a nucleation site upon which vapor condenses, and so the sensor is actually exposed to air that is at RH_i . Both RS80-A sensors measure 25-30% below RH_i in the supersaturated region of the cloud, and their close agreement with each other suggests an error in the sensor calibration. The error relative to the expected measurement of RH_i in this portion of the cloud increases with increasing height, suggesting a dependence on temperature. Below 10 km where the air is drier (5-25% RH), both radiosondes agree with the hygrometer to within a few %RH and they see similar structure in the RH field, further suggesting that the calibration error is a function of the ambient RH. The slower time-response of the radiosonde sensors relative to the hygrometer is apparent where the RH increases rapidly between 10 and 10.5 km.

Two correction approaches were developed. One approach focuses on characterizing individual sources of measurement error based on investigations conducted at Vaisala. It is shown that the dominant measurement error for the RS80-A results from inaccurate representation of the temperature-dependence of the sensor calibration in the data processing algorithm. Other measurement errors, including errors resulting from the temperature-dependence of the sensor time-response, are also described and characterized. A second empirical correction approach uses a dataset of simultaneous RH measurements from RS80-A radiosondes and the NOAA cryogenic frost-point hygrometer to develop a temperature-dependent statistical correction that represents average values of all sources of measurement error (in both instruments) under a wide variety of atmospheric conditions. Although these are operational measurements rather than a controlled intercomparison, the use of the hygrometer as an in-situ measurement standard whose calibration error is not temperature-dependent and whose time-response at cold temperatures is relatively fast improves upon previous intercomparisons where radiosondes are compared only to each other. We stress that these correction factors apply *only* to the Vaisala RS80-A radiosondes, not to radiosonde RH measurements in general, and specifically not to Vaisala RS80-H radiosondes (a detailed investigation of the RS80-H is in progress by Cole et al.).

Calibration chamber tests were conducted by Vaisala to investigate the calibration error of RS80-A sensors over a wide range of temperatures by measuring sensor response under conditions

of ice-saturation. Since the ice-cap experiment was conducted in a steady-state, sensor time-response was not a factor, and differences between the measured RH and the ambient RH_i were due solely to the calibration error that results from processing the data using a linear temperature-dependence algorithm that is increasingly inaccurate with decreasing temperature. The experimental data and the resulting %RH correction, $C(T)$, for calibration error at ambient RH_i is shown in Fig. 1.2(A) and is given by a polynomial curve fit to the data:

$$C(T) = a_0 + (a_1 \times T) + (a_2 \times T^2) + (a_3 \times T^3) + (a_4 \times T^4) + (a_5 \times T^5), \quad (1)$$

where the coefficients are: $a_0 = 0.5281$; $a_2 = 0.0329$; $a_3 = 5.9578 \times 10^{-5}$; $a_4 = 1.4305 \times 10^{-4}$; $a_5 = 8.395 \times 10^{-7}$; and $a_5 = 1.8356 \times 10^{-8}$.

This is the %RH that must be added to normally-processed data for measurements under ambient conditions of RH_i (curve 'C' in Fig. 1.2), to account for the difference between the measured RH (curve 'M', given by $RH_{max} = RH_i - C(T)$) from the linear temperature model used in the normal data processing, and the true ambient RH (RH_i). The amount of correction (ΔRH) for any measured value (RH_{meas}) is given by linearly rescaling RH_{meas} to give the correct saturation value (i.e., $\Delta RH = \frac{RH_{meas}}{RH_{max}} \times C(T)$). Then a corrected measurement ($RH_{corr} = RH_{meas} + \Delta RH$) at temperature T ($^{\circ}\text{C}$) can be written as:

$$RH_{corr} = RH_{meas} \times F(T), \quad \text{where} \quad F(T) = 1 + \frac{C(T)}{RH_i(T) - C(T)} \quad (2)$$

The correction factor $F(T)$, shown in Fig. 1.2(B), corrects for calibration error resulting from the use of a linear temperature-dependence in the data processing to represent the actual nonlinear temperature-dependence of the sensors (which was done by Vaisala for historical reasons). The correction begins to increase substantially with decreasing temperature below about -30°C . $F(T)$ is essentially 1.0 above -20°C (i.e., no correction needed), and ranges from about 1.1 at -35°C to 1.35 at -50°C , 1.8 at -60°C , and 2.25 at -65°C . Since the calibration correction is linearly proportional to the measured RH, the calibration error is fairly small in terms of %RH for dry ambient conditions, but can be quite large for moist ambient conditions at cold temperatures. This is the primary source of measurement error by the RS80-A at cold temperatures.

A second source of measurement error results from the increasing time-constant with decreasing temperature for the sensor response to changes in the ambient RH. The time-lag error for a given measurement is a function of the temperature, the rate of change of the ambient RH, and the entire history of the temperature and RH profiles being measured. Time lag results in a "smoothing" of the RH profile, where details in the RH structure are lost to a degree that increases as the temperature decreases. Quantifying and correcting for time-lag error in operational measurements is possible and we have conducted preliminary investigations, but the topic is beyond the scope of the present study. If the Air Force is an interested sponsor, we will

pursue correction for time-lag (and the other remaining measurement errors), in order to produce a complete and very accurate treatment of RH corrections.

Example calculations based on time-constant information from Vaisala show the expected temperature-dependence of time-lag errors (Fig. 1.3). The measured RH (RH_m) for a specified ambient RH (RH_a) and temperature profile is simulated for three different initial temperatures (T_0). A cloud layer of thickness 2 km at RH_i between dry layers at 10% RH is simulated, where RH_a in the transition regions varies linearly over a distance of 0.5 km. The left panels show the simulated sensor response and the extent to which the “smoothing” effect of time-lag error worsens with decreasing temperature (note that the region of decreasing RH_a in each profile has the same slope as the region of increasing RH_a but is about 15°C colder). The right panels show that the measurement error (i.e., $RH_m - RH_a$) depends strongly on temperature and is positive or negative depending on whether RH_a is increasing or decreasing. The RH_a and temperature conditions in Fig. 1.3 when $T_0 = -40^\circ\text{C}$ (center panels) are similar to the profile shown in Fig. 1.1, and the observed and simulated time-lag effects are not dissimilar. The simulated conditions represent realistic atmospheric rates of change in RH, though toward the extreme end of what is observed and therefore give a reasonable idea of magnitudes of time-lag errors near the upper limit of those that can be expected. These near-maximum time-lag errors vary with temperature from about $\pm 5\%$ RH at -20°C to $\pm 15\%$ RH at -40°C , $\pm 25\%$ RH at -50°C , $\pm 30\%$ RH at -60°C , and $\pm 35\%$ RH at -70°C . Typical errors will be considerably less, perhaps a few %RH at any temperature if RH_a is changing slowly (as occurs where $RH_a = RH_i$). Note that RH_m can exceed RH_i , because RH_i decreases with decreasing temperature and RH_m lags behind. It is obvious that the ability to resolve fine structure in the ambient RH profile decreases with decreasing temperature.

Other lesser sources of RS80-A measurement error were investigated, leading to an estimate of the accuracy of calibration-corrected data, apart from time-lag considerations. Total random production uncertainty in the measurement is $\pm 2\%$ RH at the 1σ (68%) confidence level and $\pm 4\%$ RH at the 2σ (95.5%) confidence level, independent of temperature or RH. Age-dependent errors leading to a dry bias may result from chemical contamination of the sensor polymer (~ 0 -2% RH), and a correction for this error is being developed (Cole et al., in preparation). Aging of the sensor polymer leads to a moist bias error (~ 0 -5% RH), but this error is eliminated if the pre-launch ground check correction is performed. The RS80-A, as any solid-state sensor, is incapable of measuring ice-supersaturation.

A statistical empirical approach to correcting RS80-A data was also developed, based on analysis of a dataset of simultaneous in-situ measurements by RS80-A radiosondes and the NOAA cryogenic frost-point hygrometer, which quantifies the overall measurement error for all sources of error combined, under a wide variety of atmospheric conditions. The temperature-dependence of the measurement error is clearly seen in the dataset (Fig. 1.4) by comparing the peak RH vs temperature from the two instruments (due largely to the calibration error).

The statistical correction, $G(T)$, is derived from the ratio of corresponding measurements from the Vaisala radiosondes (RH_v) and the cryogenic hygrometer (RH_c), where Fig. 1.5(A) shows curves for the mean ratio and the standard deviation in each 1°C temperature bin. The correction factor $G(T)$ at a given temperature is the reciprocal of these mean values, because the corrected mean values will be 1.0 if multiplied by $G(T)$ (i.e. $RH_v = RH_c$ on average). These correction values in each 1°C temperature bin are shown in Fig. 1.5(B), and the correction $G(T)$ is a curve fit through these points. A corrected RH_v measurement (RH_{corr}) is then given by:

$$RH_{corr} = RH_v \times G(T), \quad (3)$$

where $G(T)$ is a fourth-order polynomial with the following coefficients: $a_0 = 0.96243$; $a_1 = 0.0064011$; $a_2 = 9.4128 \times 10^{-4}$; $a_3 = 1.9461 \times 10^{-5}$; and $a_4 = 1.7515 \times 10^{-7}$. The ratio of the corrected RS80-A measurements to the corresponding RH_c measurements is shown in Fig. 1.5(C).

The statistical correction $G(T)$ is linearly proportional to the measured RH_v and accounts for the *average* of all sources of measurement error at a given temperature, for the range of mid-latitude continental atmospheric conditions. Sources of measurement error that are biases or are not linear functions of RH_v (e.g., chemical contamination, lack of ground check correction, sensor drift at high RH), or that have complicated dependences (e.g., time-lag), lead to large dispersion in the dataset and consequently large uncertainty in the corrected measurements if $G(T)$ is applied to a single profile. The average correction factor is slightly less than 1.0 for temperatures above -13°C , and ranges from about 1.1 at -20°C to 1.4 at -40°C , 2.0 at -60°C , and 3.6 at -70°C . $G(T)$ should not be used outside the temperature range of validity, 0 to -70°C , because extrapolation of the polynomial curve is meaningless and gives enormous errors. The fractional uncertainty in the *mean* of corrected RH values (i.e., when $G(T)$ is applied to a large dataset) is mostly due to random uncertainty in the hygrometer frostpoint measurement and the RS80-A air temperature measurement, and ranges from 0.06 at 0°C to 0.12 at -70°C (i.e., 6 to 12% of the measured value). The fractional uncertainty in a single corrected measurement, if characterized by the 75th percentile of the distribution at a given temperature, and generally ranges from 0.2-0.4.

Analysis similar to the above was performed on the dataset *after* applying $F(T)$ to the RS80-A measurements to remove the calibration error and assess the “residual error” from the *average* of the remaining sources of measurement error (mainly the *average* time-lag error). These results are shown in Fig. 1.6, where the “residual correction $G'(T)$ ” is compared to $G(T)$ (the dashed curve in Panel B). Below about -45°C it is seen that the calibration error dominates over the other errors, on average. $G'(T)$ is a maximum of 1.25 at -45°C , with uncertainties for mean or individual corrected values that are essentially equal to those for $G(T)$.

Application of the $F(T)$ and $G(T)$ corrections to the dataset is shown in Fig. 1.7 (Panels C and

D). Note that the calibration correction results in peak corrected RH values that very nearly follow the RH_i curve, because that is the maximum RH detectable by the sensors; whereas the $G(T)$ correction partially recovers conditions of ice-supersaturation, because these conditions were included in the dataset from which $G(T)$ was derived.

An example application of the $F(T)$ and $G(T)$ corrections to two RS80-A/hygrometer profiles, including the profile shown in Fig. 1.1, is illustrated in Fig. 1.8. Both profiles contain measurements in both moist and dry layers, and both passed through cirrus clouds where the expected response of the RS80-A in supersaturated air is to measure approximately RH_i . Note that the accuracy of $G(T)$ appears better than $F(T)$ in the supersaturated regions for these particular profiles, but the reverse may be true for other profiles due to the considerable dispersion in the dataset from which the *average* $G(T)$ correction is derived. $G(T)$ overestimates RH_c in Panel B between -25 and -40°C. After some period of time within the cloud in both cases when time-lag error becomes minimal (see Fig. 1.3) and the sensor should be measuring very close to RH_i , $F(T)$ shows a dry bias of 5-7% RH, consistent with the likely need for a few %RH correction for chemical contamination, after which the measurements are within their random uncertainty. The $G(T)$ correction partially recovers the presence of ice-supersaturation in Panel B because the presence of supersaturation on average is represented in the dataset. Note that the time-lag effect when RH_c is increasing rapidly at about 10 km altitude in Panel A is partially recovered by $G(T)$, which includes average time-lag effects in the derivation.

In summary, the correction for calibration error, $F(T)$, should be applied to all RS80-A measurements, where the dependences and approximate magnitudes of the remaining sources of measurement error (mainly time-lag and possible bias errors) were discussed. The statistical correction ($G(T)$ or $G'(T)$) compensates for the average of all sources of measurement error, but is best applied to large datasets where it gives accurately corrected mean values, and considerable uncertainty exists if it is applied to a single profile. Future individual corrections for contamination error and time-lag can further improve the accuracy and reduce the uncertainty in corrected RS80-A measurements. Reliable RH measurements at cold temperatures throughout the troposphere, suitable for climate studies or remote sensor validation, are possible with the Vaisala RS80-A if corrections are applied.

2. Vertical Distribution of Cirrus Microphysical and Optical Properties

We have conducted detailed quantitative analysis of three vertical profiles of cirrus cloud microphysical properties acquired with our ice crystal replicator, which is a balloon-borne cloud sampling instrument that collects and preserves ice crystals using the Formvar replication technique. Its primary advantages over other microphysical sampling techniques are that the profiles show the variability of cirrus microphysical properties throughout the vertical cloud column, and the imaging resolution of about 2 μm preserves detailed ice crystal shapes, which is very important for understanding cloud radiative properties.

From the analyzed replicator data we determined the vertical distribution of cirrus microphysical

properties for these case studies, and calculated the vertical variability of cloud radiative properties. We also began studies aimed at parameterizing the cloud radiative properties and their dependence on ice crystal size, shape, and position within the cloud. This preliminary analysis for two of the case studies was presented at the AMS Conference on Light Scattering by Nonspherical Particles in an article titled "Nonspherical Ice Particles in Cirrus Clouds" (reprint attached), and a more thorough study for journal publication is in order. Some specific results are summarized below. Additional analysis from the three analyzed profiles is given on our web site:

<http://www.mmm.ucar.edu/science/cirrus> (click on any of the FIRE-II studies).

This study examined the vertical distribution of the particle sizes, shapes, and locations in two cirrus clouds that contributed most to the extinction coefficients and cloud optical depth, and hence to the cloud radiative properties. Profiles through the clouds of ice crystal concentration, mean diameter, effective radius (r_e), and optical depth (τ) are shown in Figs. 2.1 and 2.2. Ice crystal size distributions at each level in the cloud where the replicator data was analyzed are shown in Figs. 2.3 and 2.4. Example ice crystal replicas showing the crystal shapes characteristic of the location in the vertical cloud column are shown in Figs. 2.5 and 2.6, showing the characteristic 3-layer structure described by Heymsfield and Miloshevich (1995), where small crystals are found near cloud top, larger crystals with pristine crystalline shapes indicating growth in conditions of ice-supersaturation are found in the mid-cloud, and rounded crystals that are sublimating in ice-subaturated air are found in the lower portion of the clouds.

The main findings of this study are summarized as follows:

- Mean particle size increases downward in both clouds from tens of microns at cloud top to 150-200 μm in the mid-cloud region, with maximum crystal sizes near cloud base of about 600 μm . This profile shape is consistent with statistical studies of the vertical distribution of radar reflectivity factor measured by Mace, and offers the possibility of parameterizing the vertical distribution of particle sizes in cirrus, although a statistically greater number of analyzed cases is needed to assess the generality of this conclusion.
- Ice crystal cross-sectional areas are measured directly by the replicator, and the calculated "area ratios" showed a tendency toward increasing circularity of crystals with decreasing size. The "area ratio" of an ice crystal (the ratio of the actual cross-sectional area of a crystal to the area of a circle which encompasses its maximum diameter) is a measure of circularity of the cross-section and is thus an important parameter in determining the light-scattering properties of the crystal. Figure 2.7 shows the area ratio of all crystals analyzed in the two case studies as a function of the maximum crystal diameter, and curves show the mean area ratio for crystals in the upper, middle, or lower portion of the cloud. There is a distinct trend throughout the cloud for crystals to be less spherical as their size increases, and also a distinct trend for crystals of a given diameter to be more spherical in the upper portion of the clouds than in the lower portion. These observations suggest possibilities for parameterizing cirrus microphysical and

radiative properties, although a statistically greater number of analyzed cases is needed to assess the generality of this conclusion. However, it is also noted that area ratios varied widely, and so a single crystal shape or aspect ratio may not adequately represent cirrus clouds in radiative transfer calculations.

- Crystal sizes that contribute most to the extinction coefficients increase downward, from $<50 \mu\text{m}$ at cloud top to $>150 \mu\text{m}$ at mid-cloud and lower levels. Figure 2.8 shows the cumulative cross-sectional area of all particles having a diameter less than D , for three levels in the 25 Nov. cloud (cloud top, mid-cloud, and cloud base). The dashed line gives the diameter of the median cross-sectional area ($D_{0.5}$), where half the optical extinction in the cloud (which is proportional to the total particle cross-sectional area) is contributed by particles smaller than $D_{0.5}$ and half the extinction is from particles larger than $D_{0.5}$. Vertical profiles of $D_{0.5}$ (and also $D_{0.2}$ and $D_{0.8}$ through both clouds are shown in Fig. 2.9. This vertical distribution of optical extinction in cirrus may also be amenable to parameterization, but a statistically greater number of analyzed cases is needed to assess the generality of this conclusion.

- The cloud optical depth is half what it would be if calculated from the size distributions assuming that the crystals had circular cross-sections (a common assumption in simplistic radiative transfer calculations), so the effective area ratio for each cloud as a whole is about 0.5. Figure 2.10 shows the contributions in the vertical to the total cloud optical depth (τ) from the directly-measured particle cross-sectional areas, integrated from cloud top downward (where the vertical coordinate is normalized position in the cloud, and the total optical depth as would be measured by a sunphotometer on the ground is the value of τ at $Z/Z_0 = 0$). The curve labeled "S" is the optical depth profile calculated from the size distribution assuming the particles are spheres. The numbered profiles show the contribution to τ from crystals having an area ratio less than the labeled value. It is apparent that on average the crystals are far from spherical, and that assuming spherical crystals leads to a factor of two error in calculated optical depth. The ratio τ/τ_S as a function of height is a potentially useful optical property of cirrus and its vertical distribution may be amenable to parameterization, but a statistically greater number of analyzed cases is needed to assess the generality of this conclusion.

- Particles $<50 \mu\text{m}$ contribute minimally to the total cloud optical depth, and about two-thirds of the contribution to τ in both clouds is from particle sizes in the range 50-250 μm . This observation opposes speculations that small ice crystals near the tops of cirrus may dominate the optical properties. Figure 2.11 shows the fractional cumulative contribution to the total cloud optical depth from crystals with diameters smaller than a given value. The crystal size ranges and their relative contributions to the cloud optical depth is a potentially parameterizable cirrus optical property, but again, more analyzed cases are needed to assess the generality of this conclusion.

- Further study in this area based on similar analysis of additional replicator profiles and on radiative transfer calculations is in order, toward assessing the generality of these results and

preparing a thorough study for journal publication. If the Air Force is an interested sponsor, it would make this further study possible.

3. Relative Humidity Conditions for the Formation of Cirrus and Contrails

The temperature-dependent relative humidity (RH) conditions in the atmosphere required to nucleate ice crystals ($RH_{nuc}(T)$) were investigated using measurements acquired in orographic wave cloud and cirrus environments. High ice-supersaturations in clear air, conducive to the maintenance of aircraft contrails yet below RH_{nuc} and therefore insufficient for cirrus formation, are not uncommon in the atmosphere, as illustrated in Fig. 3.1 by a contrail produced by the NASA DC-8 during the SUCCESS experiment that formed upwind of an orographic wave cloud. Orographic wave clouds are ideal for studying ice nucleation conditions because the airflow is smooth and laminar, and the RH increases continually as the temperature decreases in the ascending air upwind of the cloud until RH_{nuc} is reached at the cloud edge. The nucleation of ice crystals in the cloud in Fig. 3.1 is seen in Fig. 3.2, where the RH is plotted along the aircraft track in an upwind-to-downwind cloud penetration. The labeled points indicate the first detection of cloud particles by the following microphysical instrumentation (with size detection thresholds given in parentheses): ‘M’=MASP (0.5 μm), ‘V’=VIPS (5-10 μm), ‘C’=CVI (5-10 μm), ‘P’=PVM (~ 5 μm), ‘O’=visually observed cloud edge from on-board flight notes. The dashed curve is particle concentration from the CVI, showing that the cloud edge is abrupt and suggesting that ice crystals nucleate in the updraft upwind of first-detection by the MASP and grow rapidly until detected by instrumentation with larger detection thresholds. S^* is the peak RH, where the vapor supply rate from the updraft is equal to the vapor depletion rate from the growing ice crystals. Ice-saturation at this temperature (-65°C) is 55% RH (bold dashed line), and RH_{nuc} is between 70% RH (the RH measured upwind of the cloud, where the contrail in Fig. 3.1 persisted in clear air), and 88% RH (where the MASP first detected 0.5 μm ice crystals).

Further insight into the observed high RH values needed for ice nucleation is given by calculations shown in Fig. 3.3 of the equilibrium vertical velocity (U_{eq}) required to balance vapor depletion from a given ice crystal concentration (N) and ice-water content (IWC), when the RH is at RH_{nuc} as determined by Heymsfield and Miloshevich (1995), at temperatures of -40 or -60°C . The curves indicate three values of IWC at each temperature, given in terms of the temperature-dependent “potential adiabatic IWC” (IWC_{ad}), which is the IWC that results from complete conversion to ice of the water vapor between RH_{nuc} and ice-saturation (RH_i). Values greater than IWC_{ad} might result from ice crystal fallout into a parcel from above, and values less than IWC_{ad} might exist shortly after ice nucleation begins or in cloud top parcels if ice crystal fallout occurs. The following conclusions can be drawn from scrutiny of Fig. 3.3:

- Very high in-cloud RH values may occur if the vertical velocity is high, the crystals are small, or the IWC is low. For example, shortly after ice nucleation, if the IWC is $0.1 \times IWC_{ad}$ and the ice crystals are 10 μm diameter (at $N=700 \ell^{-1}$ in Fig. 6), U_{eq} is about 20 cm s^{-1} . In a wave cloud environment ($U > U_{eq}$) the RH would continue to rise above RH_{nuc} (and presumably ice

nucleation would continue); if vertical velocities are weak ($U < U_{eq}$) vapor depletion would exceed vapor supply and the RH would fall below RH_{nuc} (and presumably ice nucleation would cease).

- Continued or renewed ice nucleation in an existing cirrus is most likely to occur at cloud top, where fallout of ice crystals leads to a lower IWC and U_{eq} at cloud top and to a higher IWC and U_{eq} below cloud top.
- Far greater vertical velocities are required to maintain RH_{nuc} at -40 than -60°C . It is much more likely to observe $RH > RH_{nuc}$ at colder temperatures.

We expanded on earlier work by Heymsfield and Miloshevich (1995) that determined the ice nucleation condition $RH_{nuc}(T)$ in the temperature range -35 to -56°C . We used RH measurements from aircraft during the FIRE-II and SUCCESS experiments, plus balloon-borne data, to investigate RH_{nuc} at colder temperatures and to investigate whether its value depends on the sampling environment (continental vs maritime), where a lower limit to RH_{nuc} is given by the upper limit of RH measured in clear air in these datasets (i.e., conditions where no ice crystals have nucleated). These results were presented in a paper published in *Geophysical Research Letters* titled "Upper-tropospheric Relative Humidity Observations and Implications for Cirrus Ice Nucleation" (reprint attached).

The RH measurements indicate that high ice-supersaturations in the upper troposphere are not uncommon, both in clear air and in clouds. The FIRE-II and balloon-borne data show that the cirrus ice nucleation condition, $RH_{nuc}(T)$, is consistent with Heymsfield and Miloshevich's (1995) $RH_{hn}(T)$ curve in continental environments down to -55°C , but RH_{hn} should not be extrapolated to lower temperatures. The SUCCESS data indicate that RH_{nuc} below -55°C is between 70 and 88%. RH_{nuc} may also depend on characteristics of the aerosols. Perhaps a minimum of two RH_{nuc} relations are needed — representing continental and maritime airmasses — but much more data are needed to assess particularly the maritime relation. Uncertainty in observing RH_{nuc} increases at cold temperatures because ice crystal growth rates are very slow and the RH may rise substantially before ice crystals are detectable by most microphysical instrumentation. A well-conceived experiment in orographic wave clouds, with accurate RH measurements and microphysical instrumentation with a submicron detection threshold, may provide a relatively simple dynamical environment for further study of continental ice nucleation conditions. If the AFOSR is an interested sponsor, Colorado State University is planning just such an experiment, and we could contribute much to further research on ice nucleation conditions if funded to participate.

4. Variability of Cirrus Microphysical Properties

An article entitled "Mid-latitude and tropical cirrus microphysical properties" (copy attached) has been accepted for publication in a book on Cirrus Clouds to be published by the Optical Society of America. In this article, cirrus cloud microphysical data acquired in mid-latitude and tropical locations by many researchers have been summarized, and the principal instruments and

measurement techniques used to collect the data have been described. The locations of all cirrus measurements assessed in this paper are shown in Fig. 4.1. Some of the principal findings are outlined below.

- Ice particle shapes vary considerably from one cloud to another (Figure 4.2). Polycrystals, especially bullet rosettes, are the predominant ice particle form in mid-latitude, in-situ generated cirrus, although columns and single bullets are found frequently. There is some suggestion that columns predominate with cloud top temperatures below -55 or -60°C. Near cloud base, crystal edges round in response to sublimation. Particles in anvils can be aggregated and rimed and shapes can be more complex.
- Cirrus cloud properties, for example concentration, extinction coefficient, and ice water content, can be highly variable from one cloud to another and within a single cloud. However, there does appear to be a tendency for the mean and maximum crystal size, extinction coefficient and ice water content to increase with temperature (Figures 4.3-4.6).
- Ice crystals smaller than 100 μm dominate the number concentration, especially near cloud top where the predominant ice particle nucleation occurs. Ice particle size tends to increase downward to near cloud base. The lowermost parts of cirrus tend to be sublimation regions.
- While small ice crystals dominate extinction near cloud top, larger particles in the mid and lower-cloud levels are responsible for most of the cloud optical depth on average. Similar findings are noted for ice water content.
- Parameterizations of the size spectra in terms of the ice water content and temperature have been developed. They are broad averages and cannot represent the variability from one cloud to another.
- Most of the cirrus cloud microphysical data have been acquired with Particle Measuring Systems 2D imaging probes. The concentrations below 100 μm , and the derived microphysical properties from these probes, have been significantly underestimated for temperatures below -55°C. Probes have been developed in recent years to provide habit and concentration information in the smaller sizes.

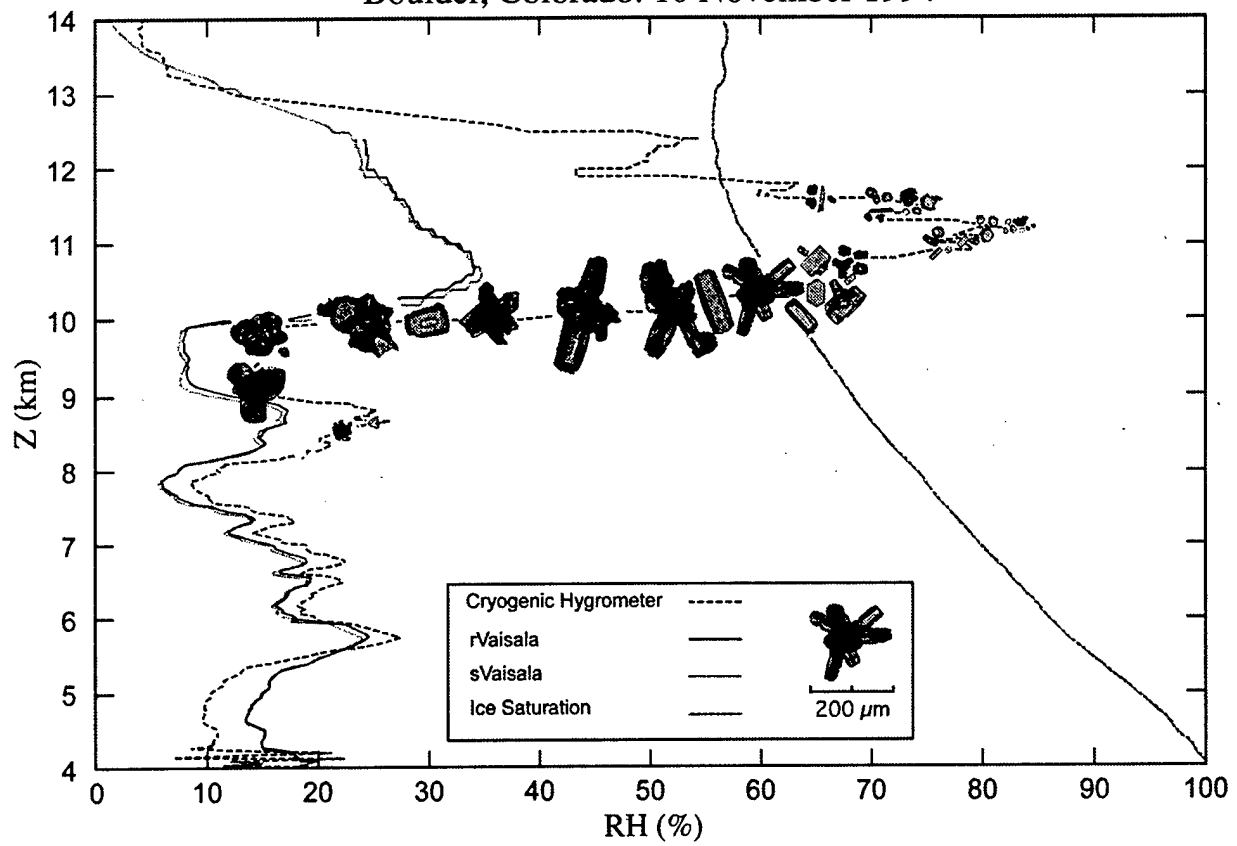
5. Improved Theory of Contrail Formation

Two articles on contrail formation were prepared as part of our Air Force funded research. The first article was prepared by Ilia P. Mazin, drawing upon his extensive background with contrail studies in the former Soviet Union. The article briefly describes the research on contrails performed in the former Soviet Union and includes work on the theory of formation and evolution of contrails, as well as the results of special experimental flights and questionnaires filled out by military pilots. The data were collected mainly by I.P. Mazin and A.Kh. Khrgian and published in special editions in the 1950s, unknown to a wide circle of meteorologists. A generalization of the Appleman theory is proposed, allowing the determination of atmospheric conditions favorable for the formation of contrails with arbitrary flight regimes, if the efficiency

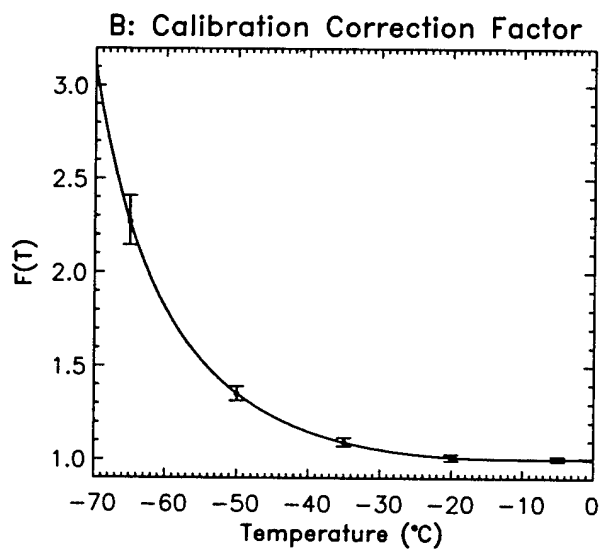
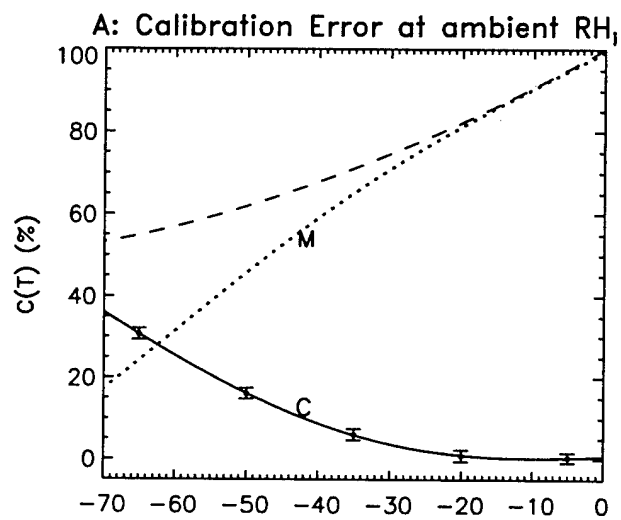
of the aircraft engines is known. The increased efficiency of aircraft engines extends the area favorable for the formation of contrails. Equations for evaluating the lifetime of contrails are given.

The second article, "On the Theory of Exhaust Jet Aircraft Condensation Trails", was published by Ilia P. Mazin and Andrew J. Heymsfield, in *Meteorology in Russia*, 1998, **9**, pp 5-14, and also submitted to *Geophys. Res. Letters* (attached). The theory of aircraft contrail formation originally developed in the 1950's in the United States by Appleman and in Russia by Mazin is generalized to account for energy loss by a jet aircraft engine, e.g., not all of the fuel used by a jet engine is converted into heat as is usually assumed. The Appleman contrail factor C is transformed into the contrail condensation parameter (CCP) which is $k = \frac{100 C}{f \epsilon}$, where ϵ is the energy loss coefficient, and $f\%$ is the minimum relative humidity with respect to water at which the processes of condensation begins in a plume. These new results are compared to Appleman's results in Figure 5.1. Appleman's contrail threshold formation temperatures T_{th} is estimated to increase by about 9°C . The condition $T_a < T_{th}$, where T_a is the air temperature is necessary but not sufficient for the formation of visible and in particular persistent contrails; another requirement is that the ambient vapor density is equal to or exceeds ice saturation. Some problems and objectives of further contrail investigations are examined. When considering possible inadvertent anthropogenic influence upon the climate, one of the most important tasks is to study the statistics of the existence of layers in the upper troposphere that are supersaturated with respect to ice. Our other research described earlier has contributed significantly to this latter task.

Boulder, Colorado: 10 November 1994

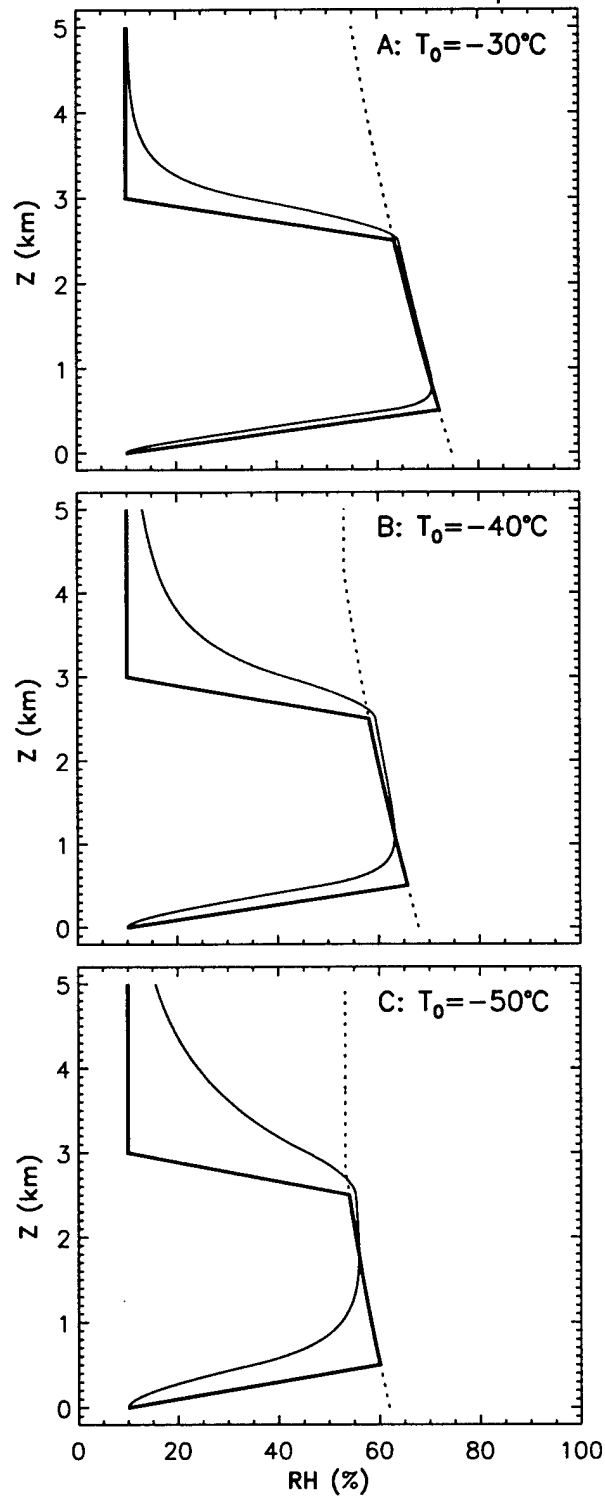


1.1



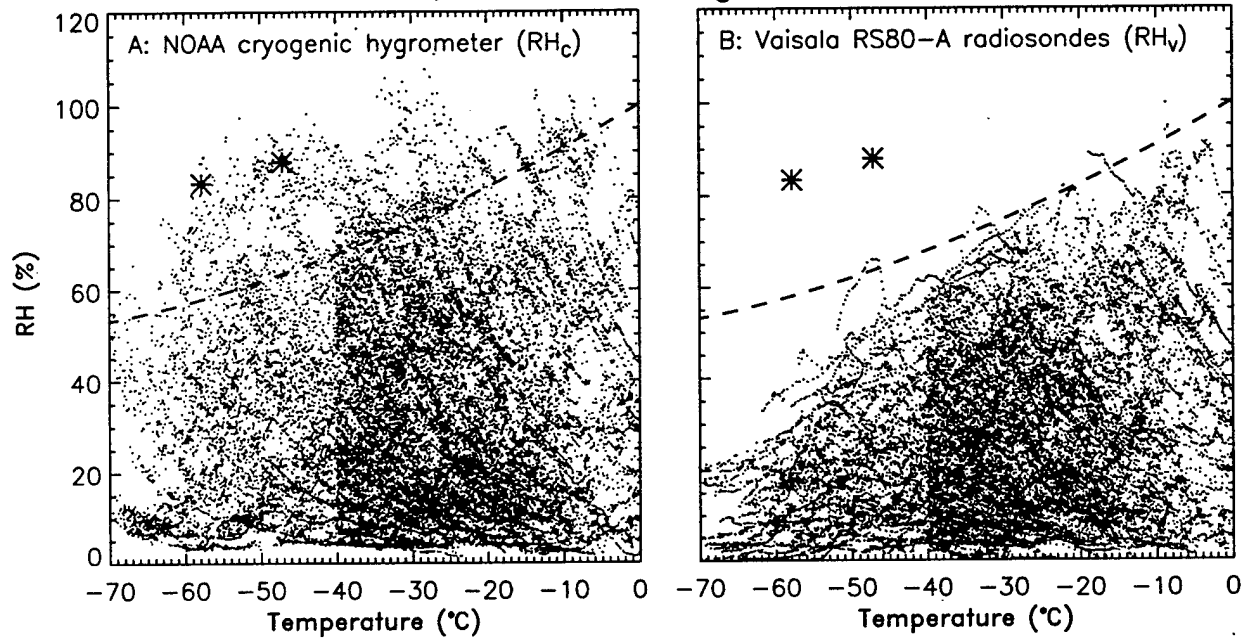
1.2

Simulated RS80-A Time Response



1.3

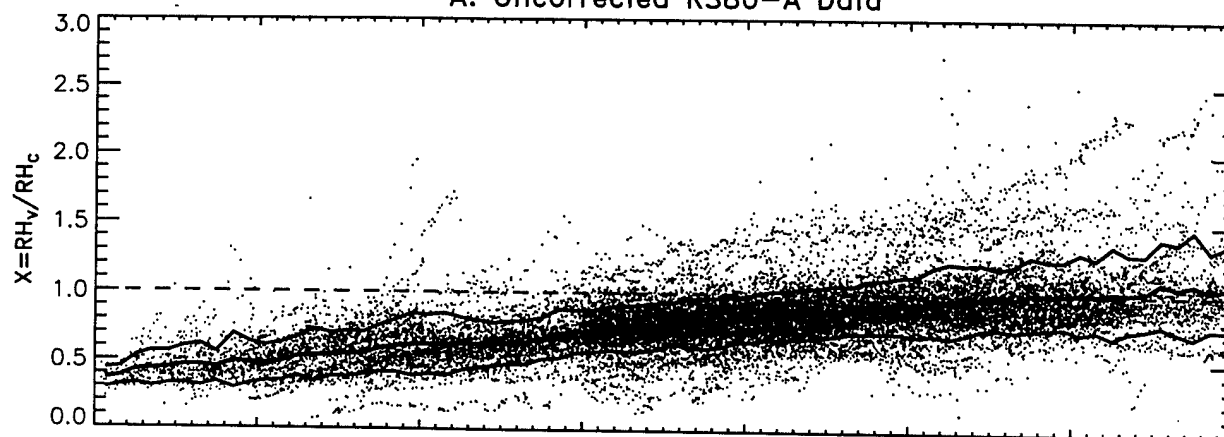
Boulder, CO Soundings: 1991-1998



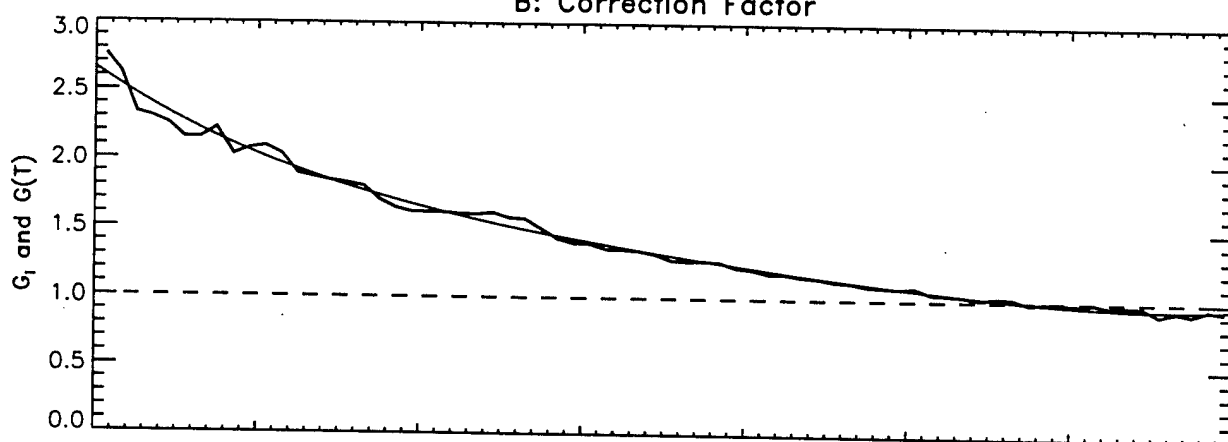
1.4

G.o4T0-70m1fp0Cr100w1s1u1o130.all (Final)

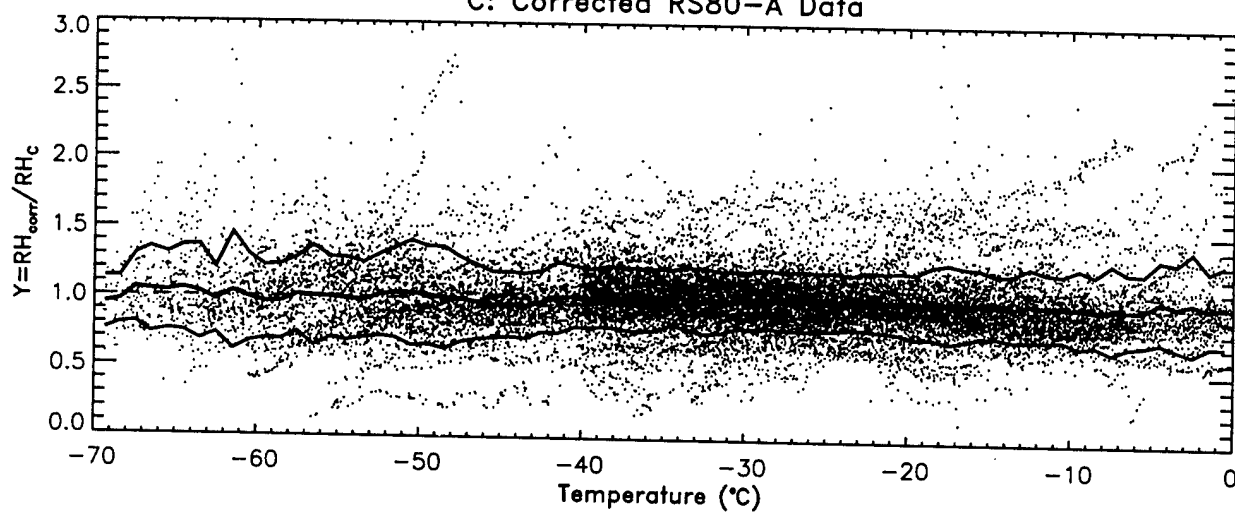
A: Uncorrected RS80-A Data



B: Correction Factor

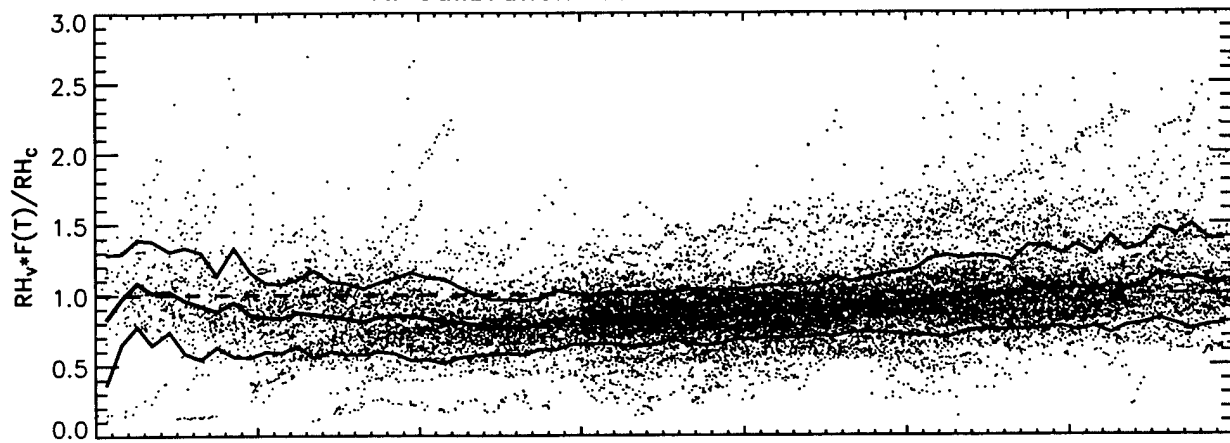


C: Corrected RS80-A Data

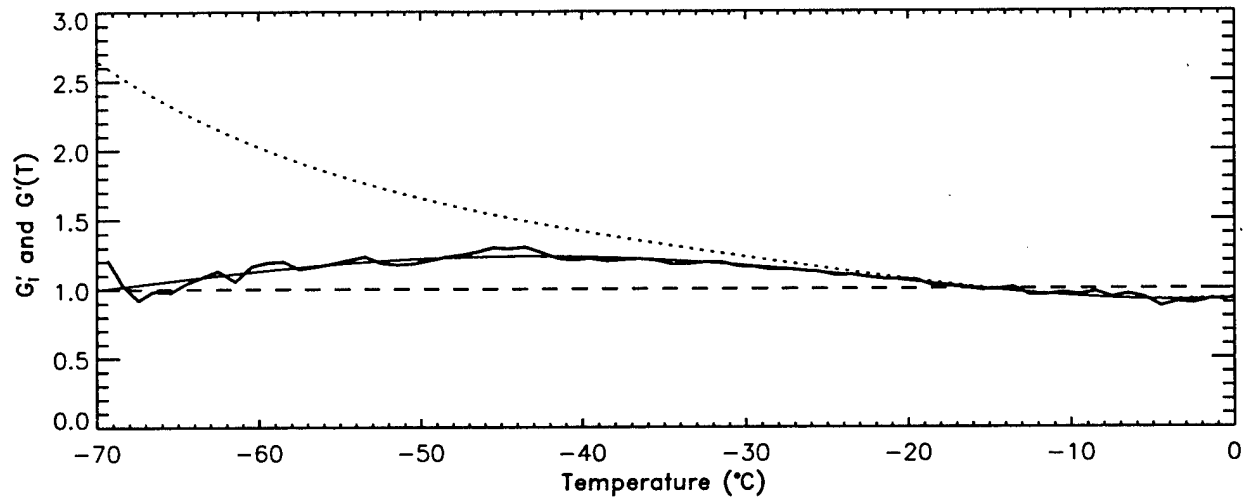


1.5

A: Calibration-corrected RS80-A Data

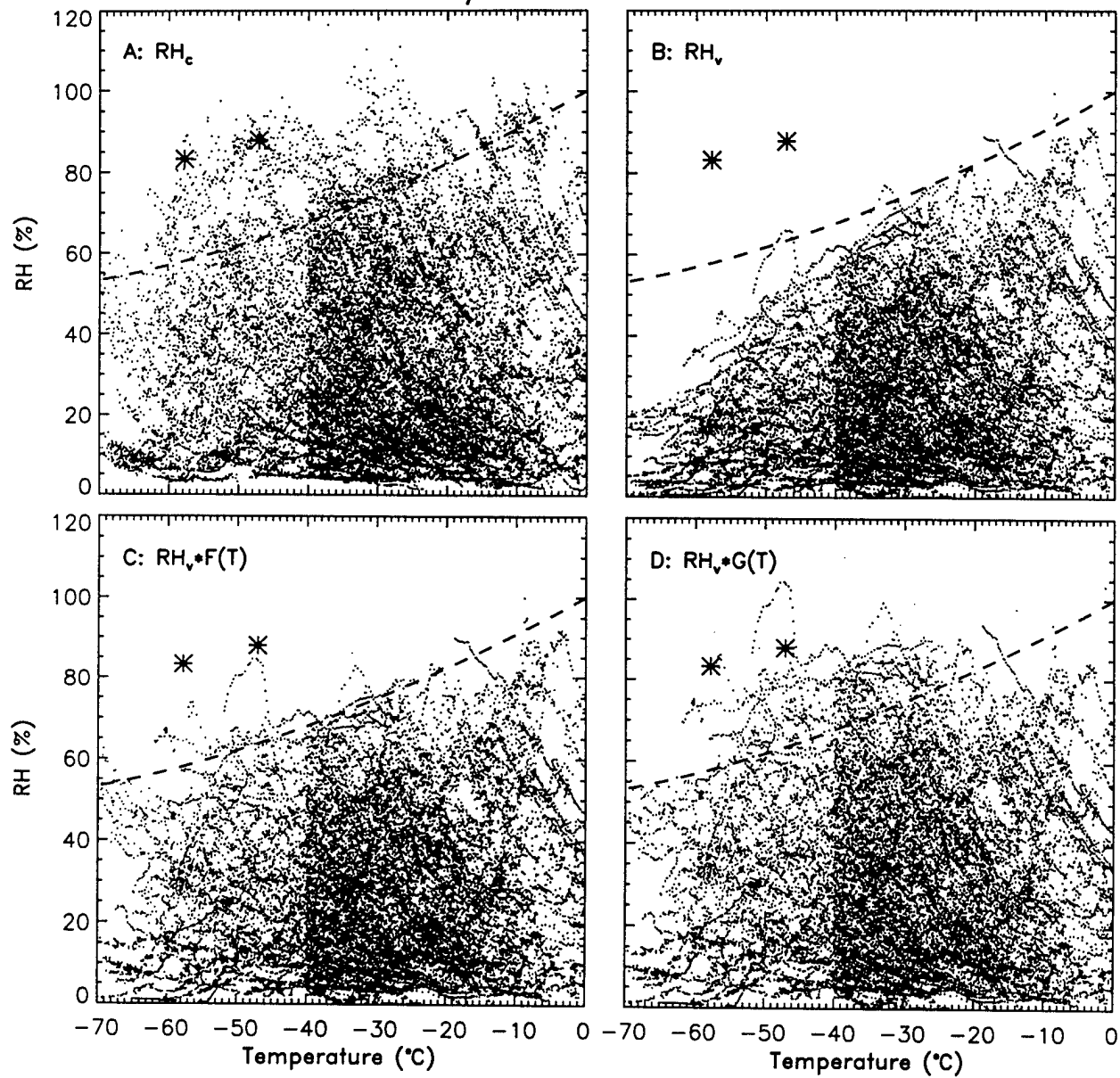


B: Residual Correction Factor



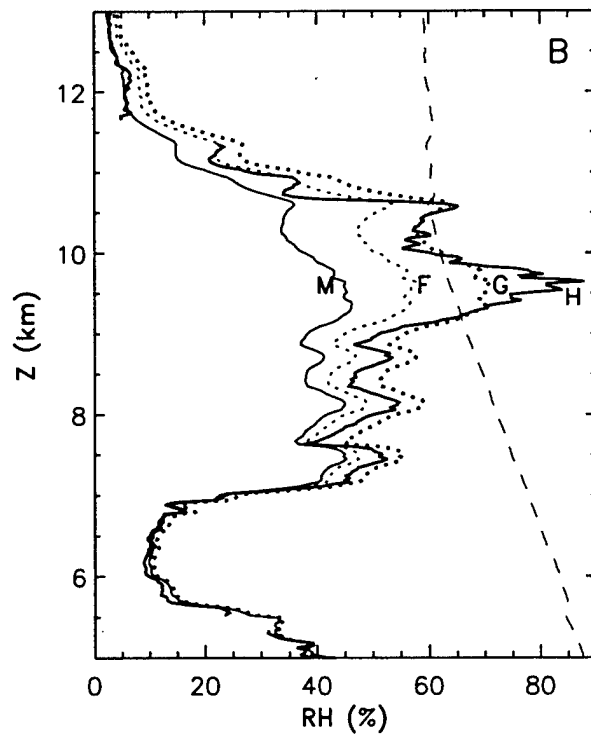
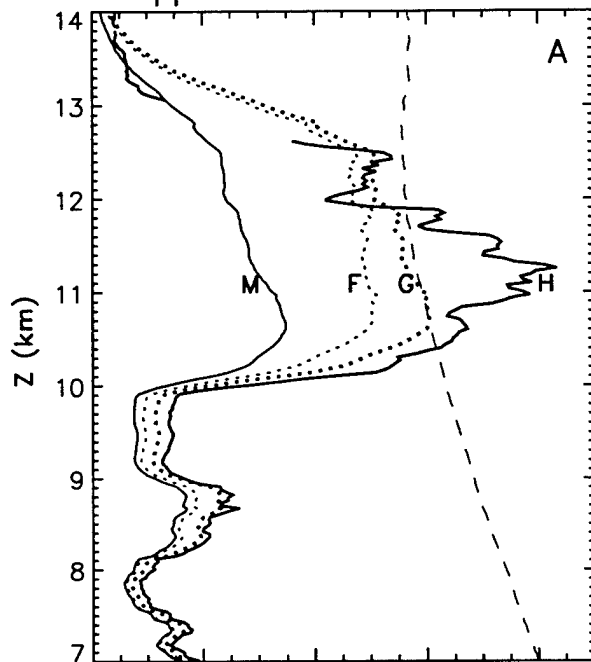
1.6

Summary of Corrected Dataset



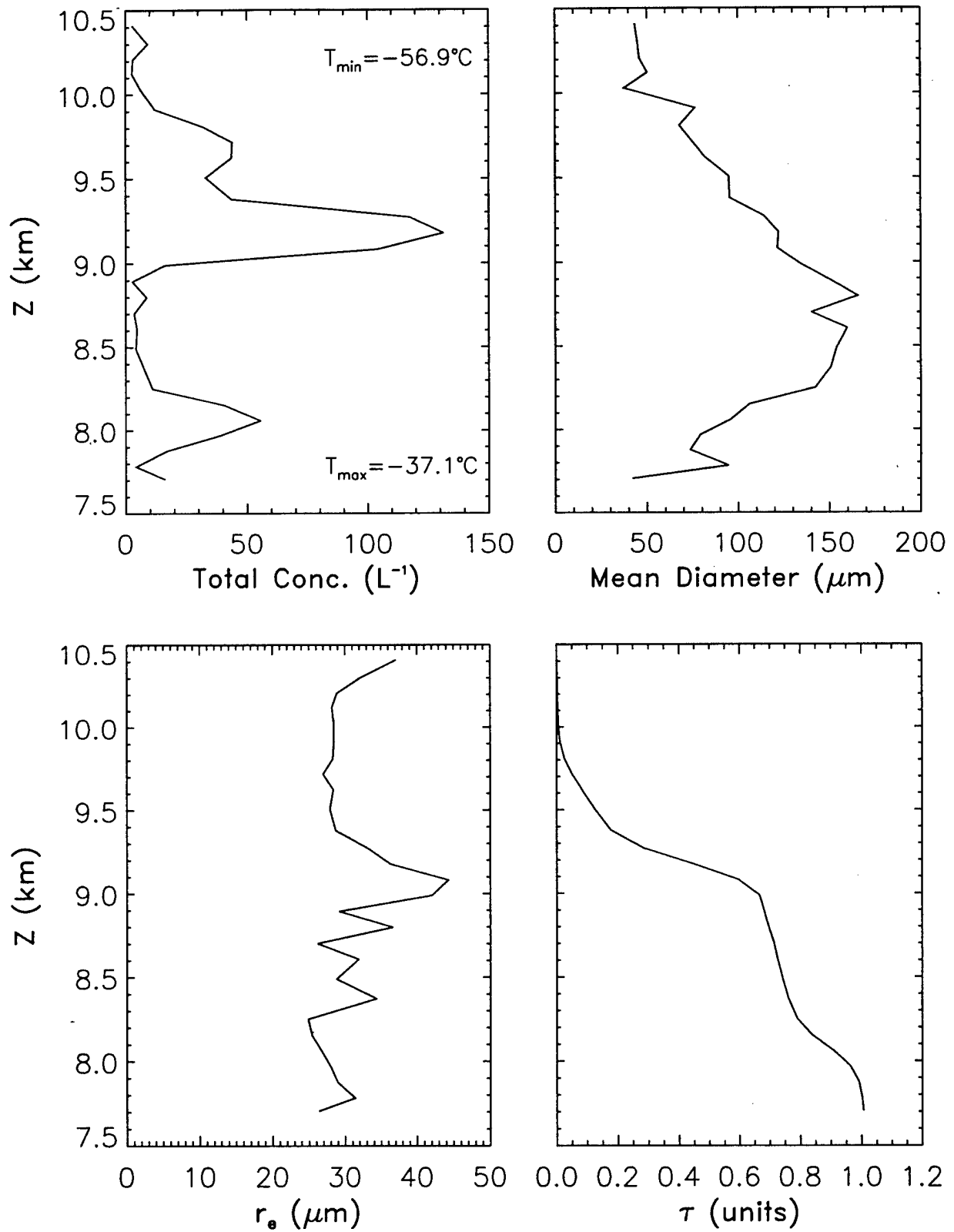
1.7

Application of Corrections



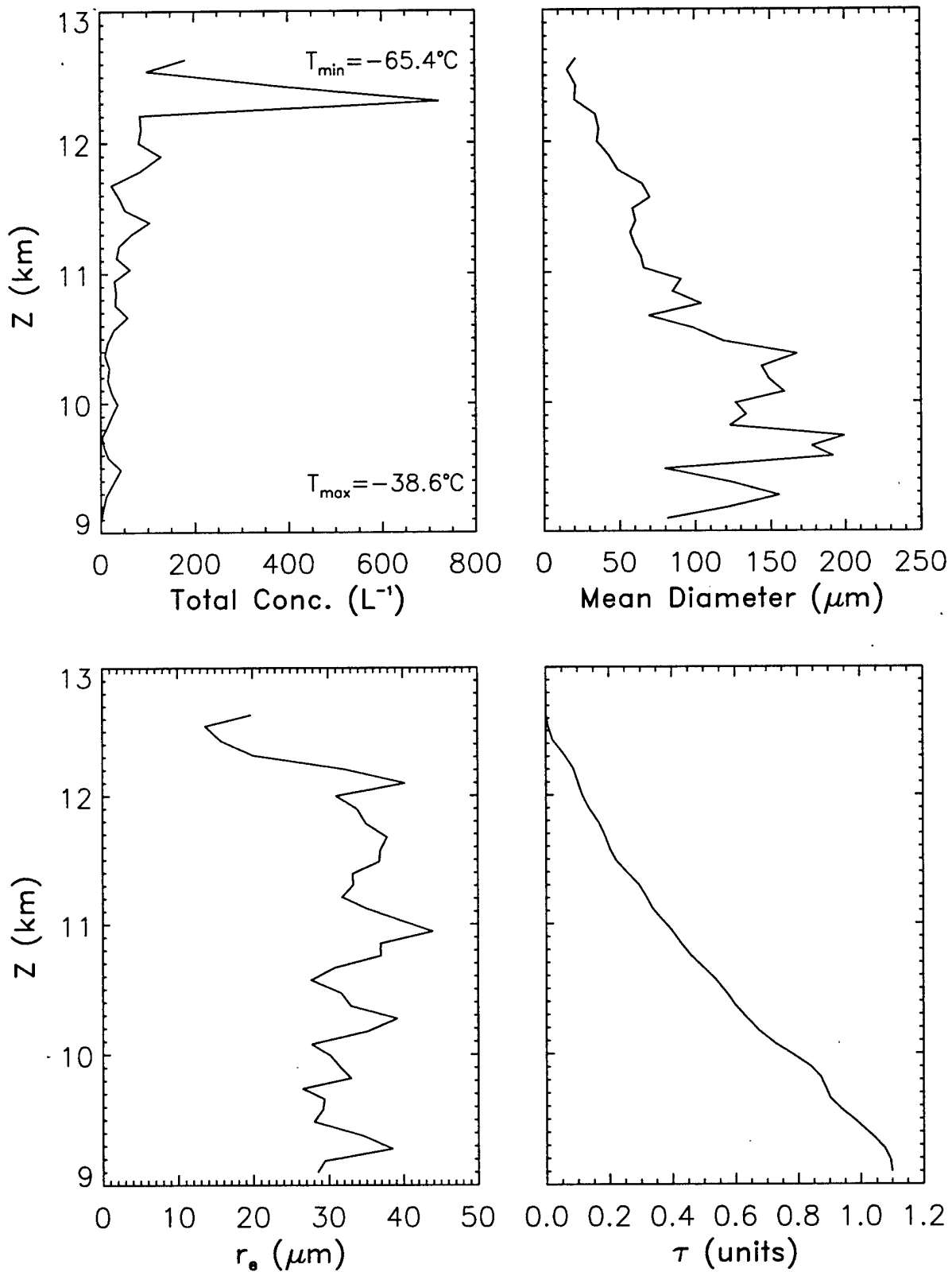
1.8

Replicator - FIRE - 25 Nov. 1991



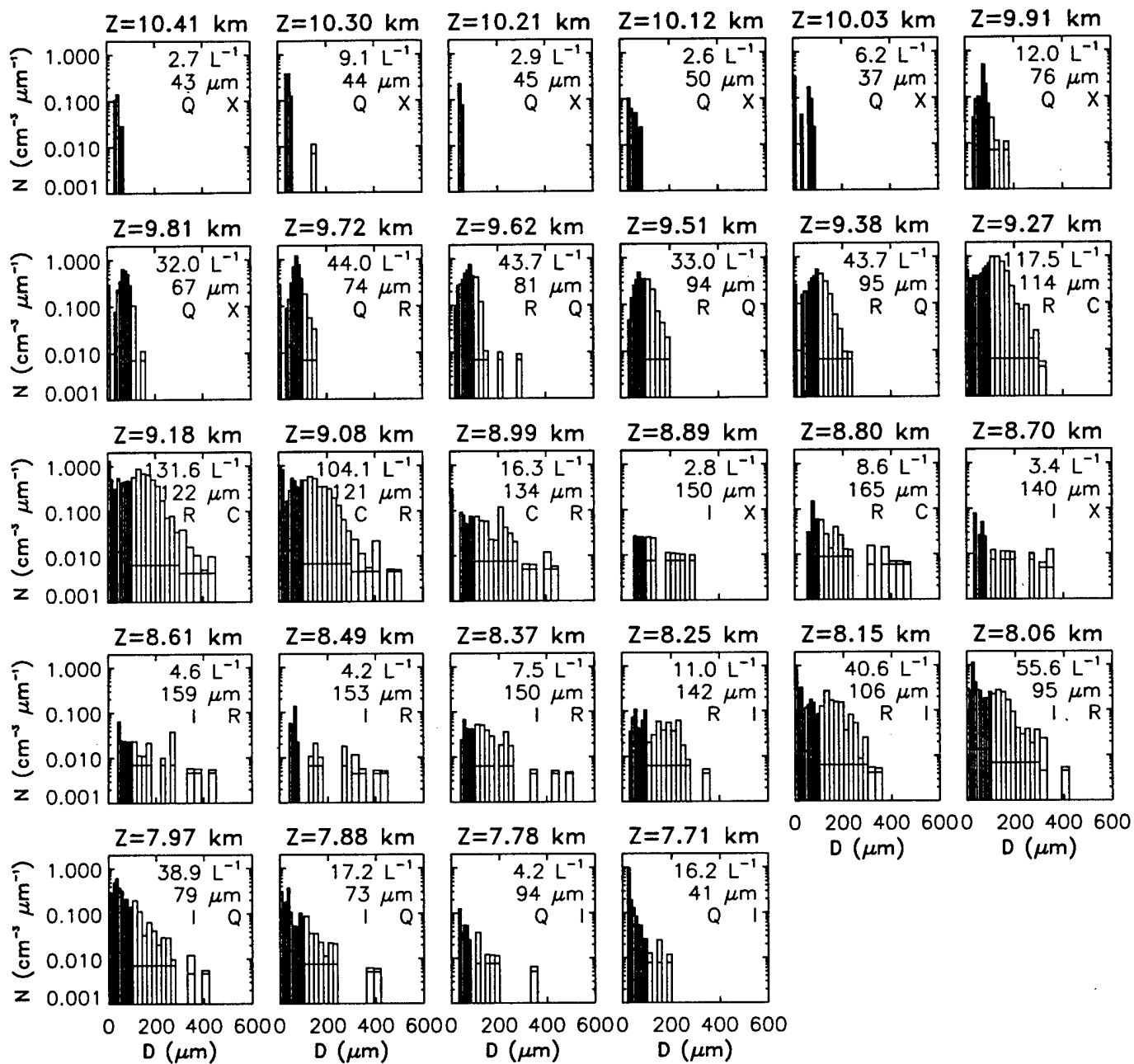
2.1

Replicator - FIRE - 5 Dec. 1991

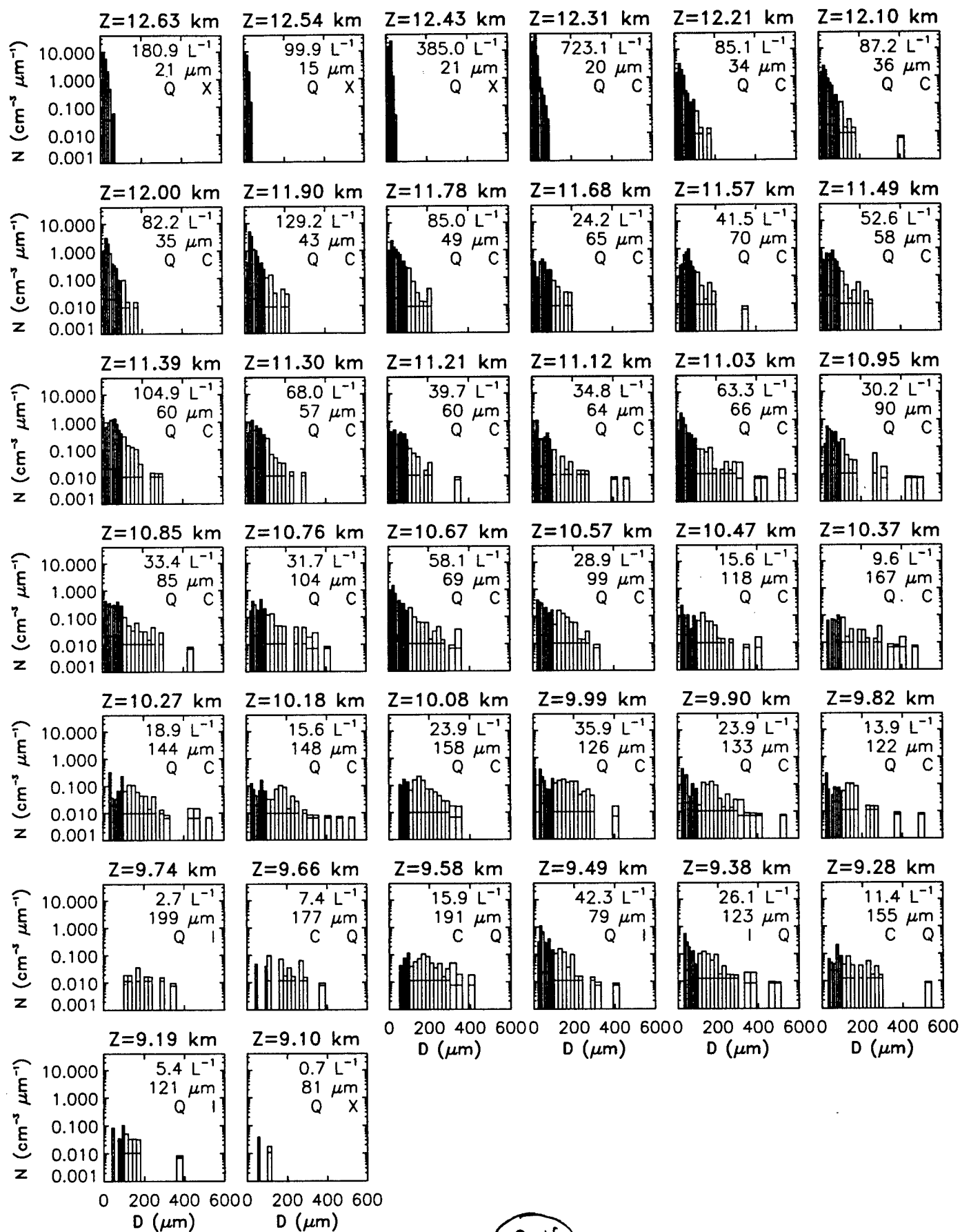


2.2

Replicator Size Spectra: FIRE: 25 Nov. 1991



Replicator Size Spectra: FIRE: 5 Dec. 1991



2.4

25 Nov 1991 Replicator Profile

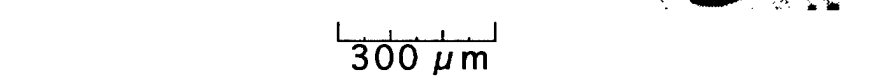
-55°C

-50°C

-45°C

-40°C

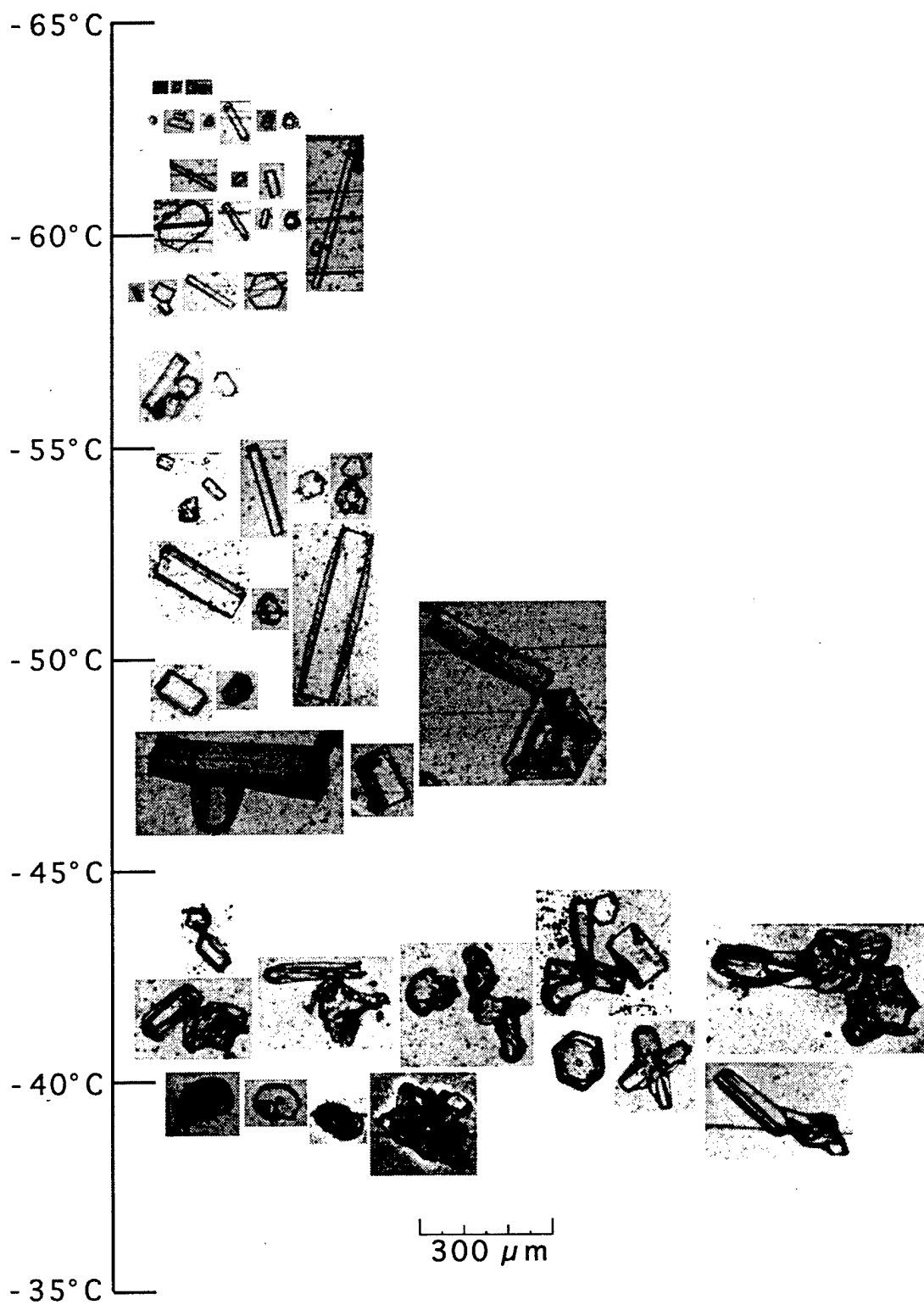
-35°C



300 μ m

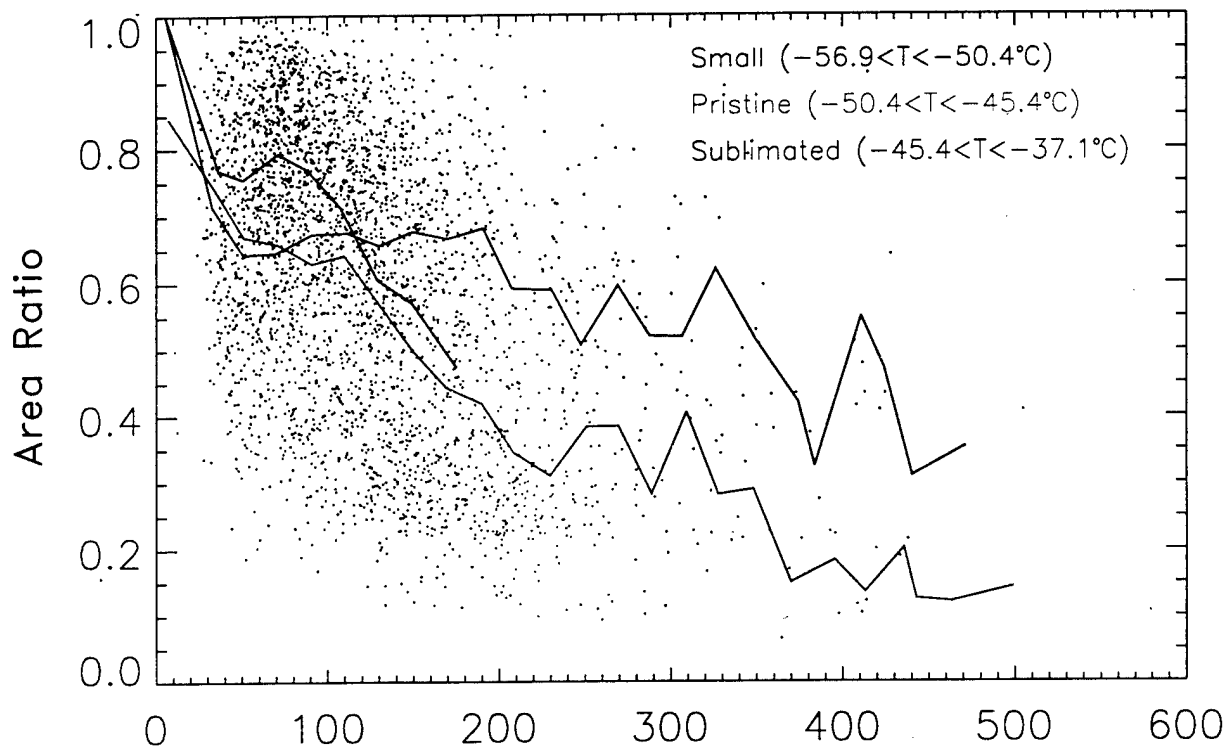
2.5

5 Dec 1991 Replicator Profile

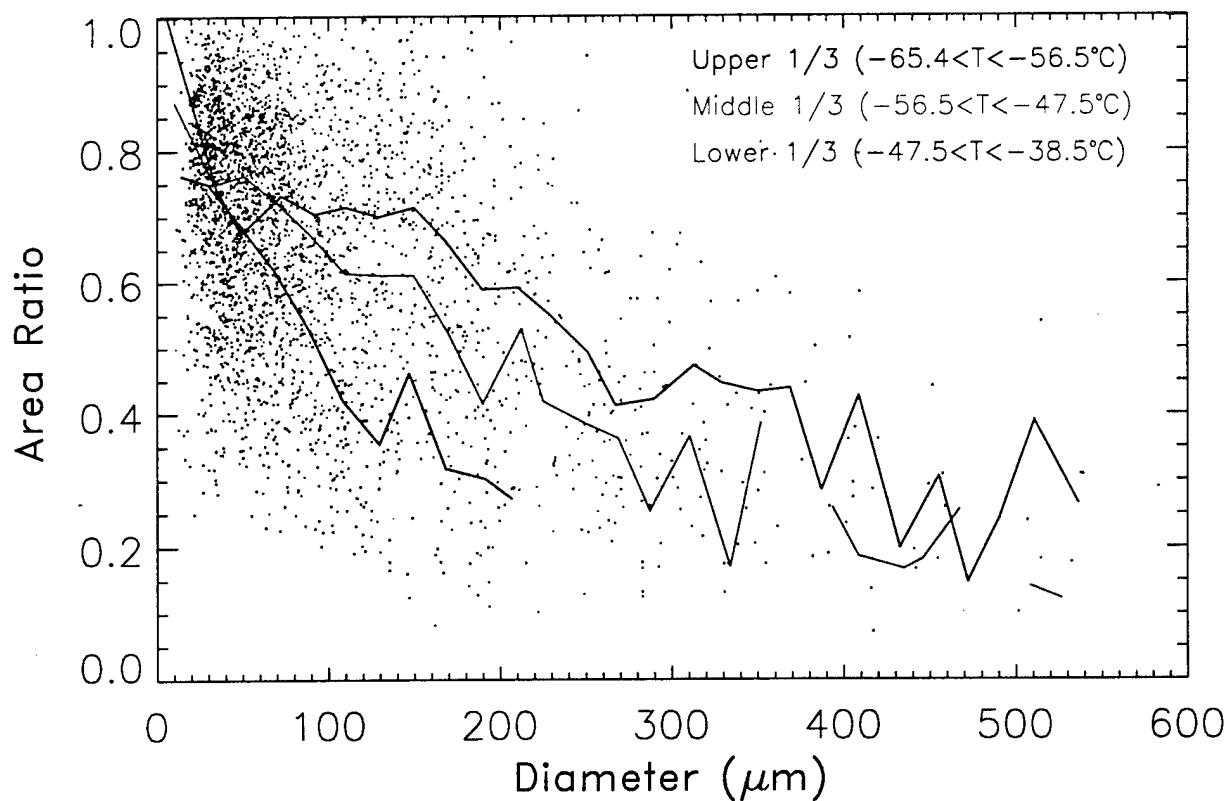


2.6

FIRE - 25 Nov. 1991

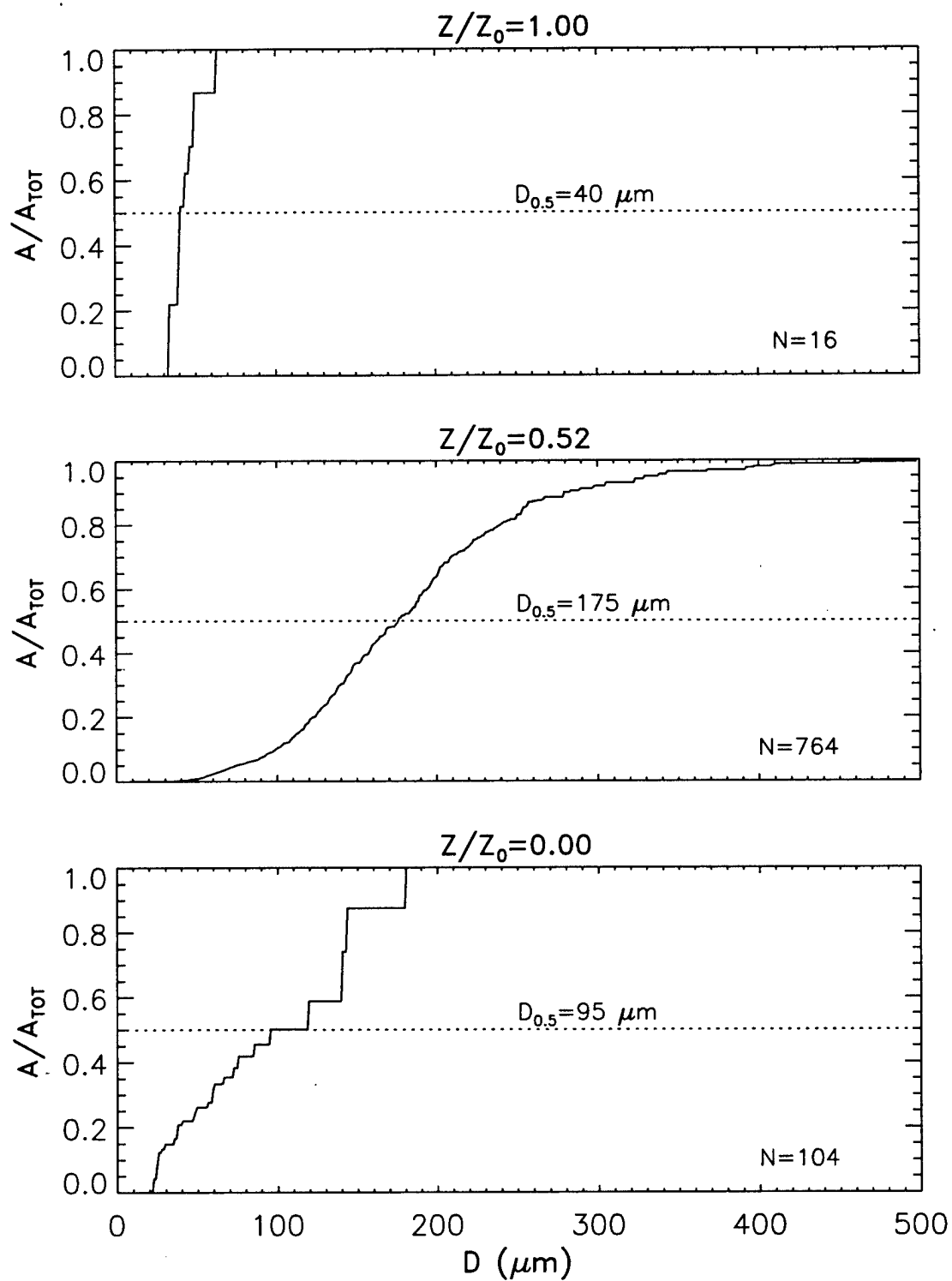


FIRE - 5 Dec. 1991



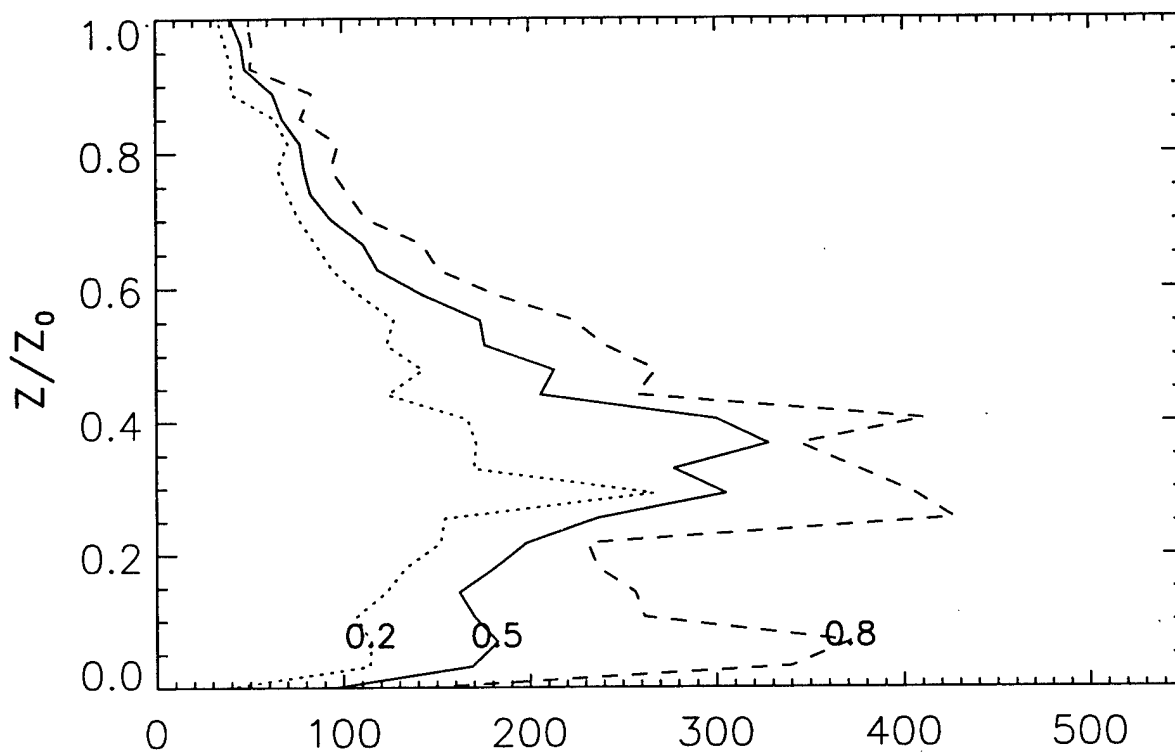
2.7

Cumulative Cross-Sectional Area – 25 Nov 1991
28 Levels Analyzed

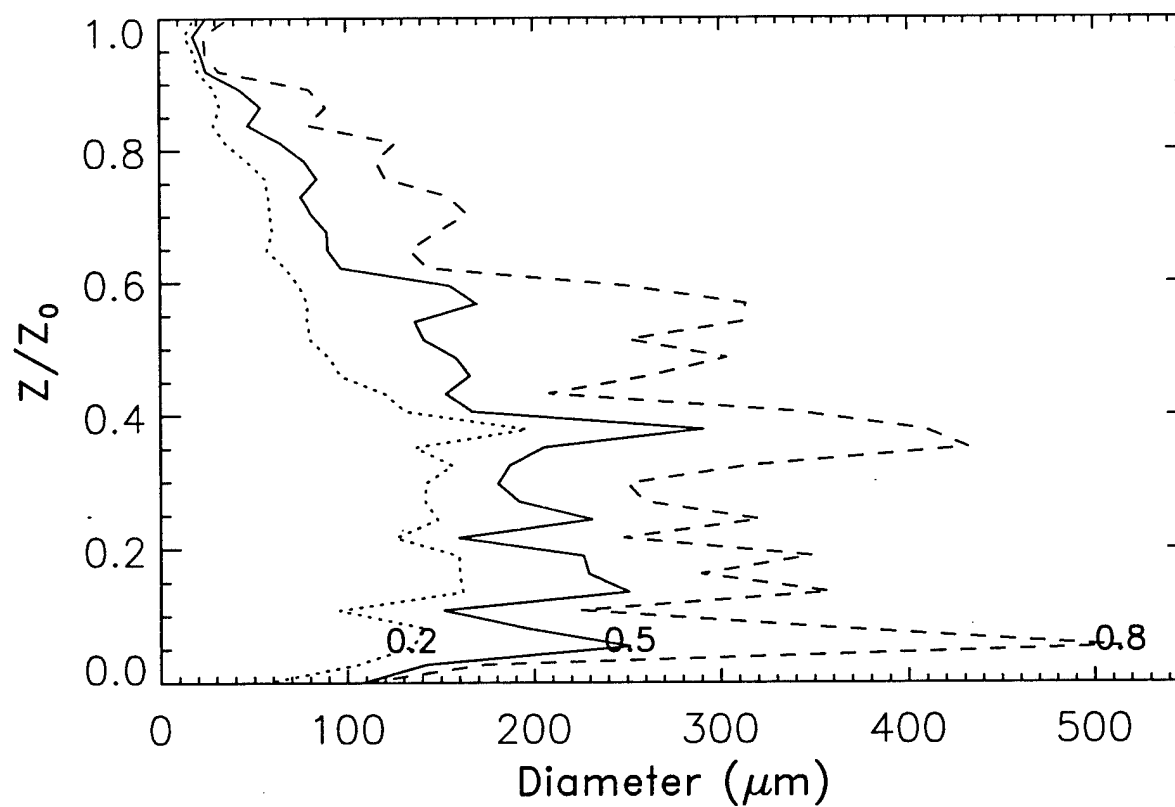


2.8

FIRE - 25 Nov. 1991

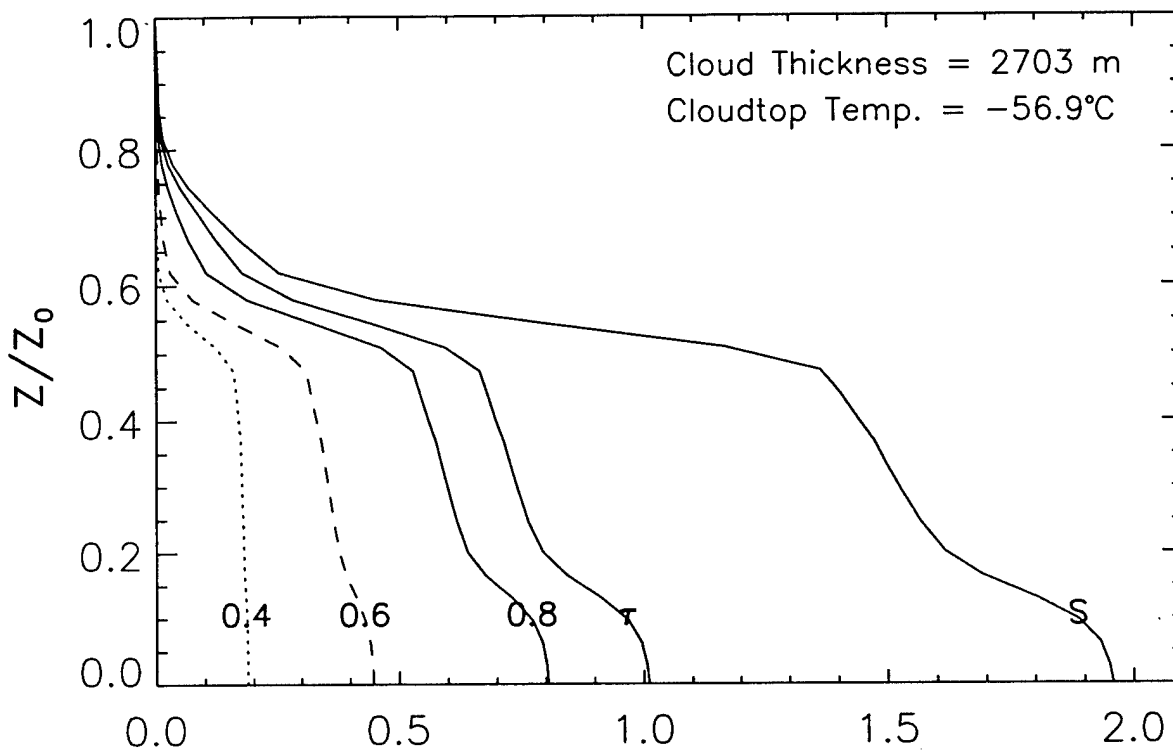


FIRE - 5 Dec. 1991

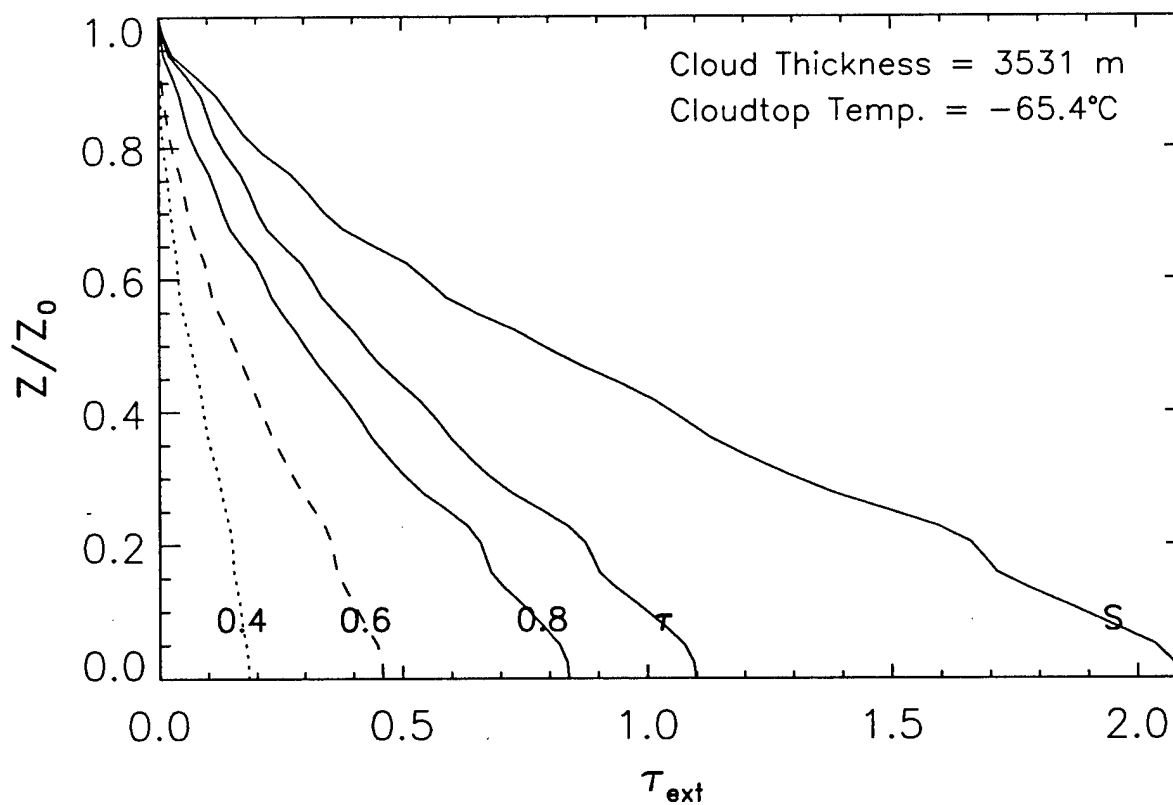


2.9

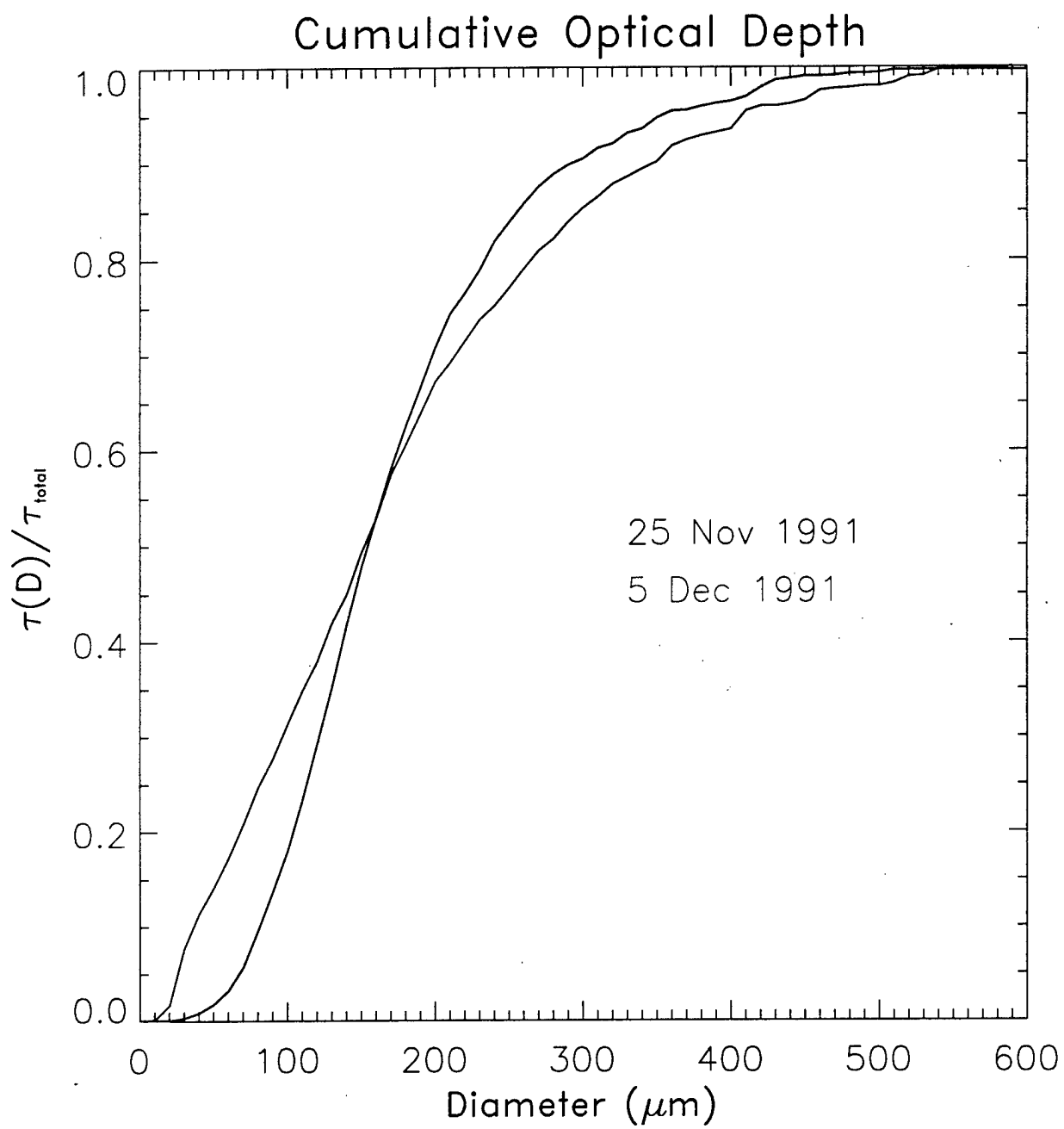
FIRE - 25 Nov. 1991



FIRE - 5 Dec. 1991



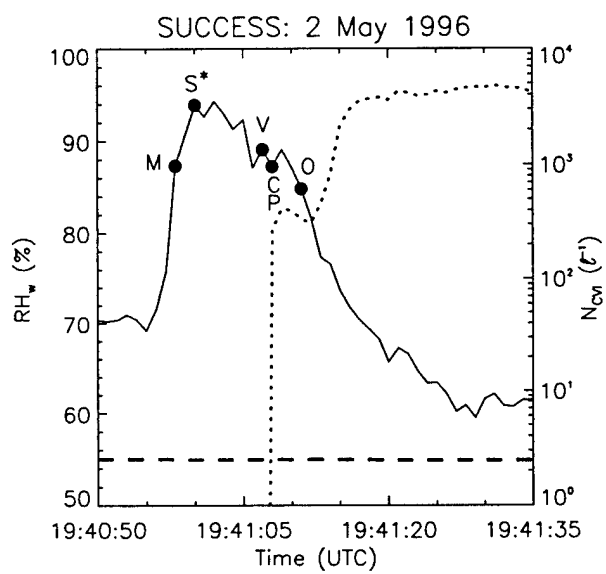
2.10



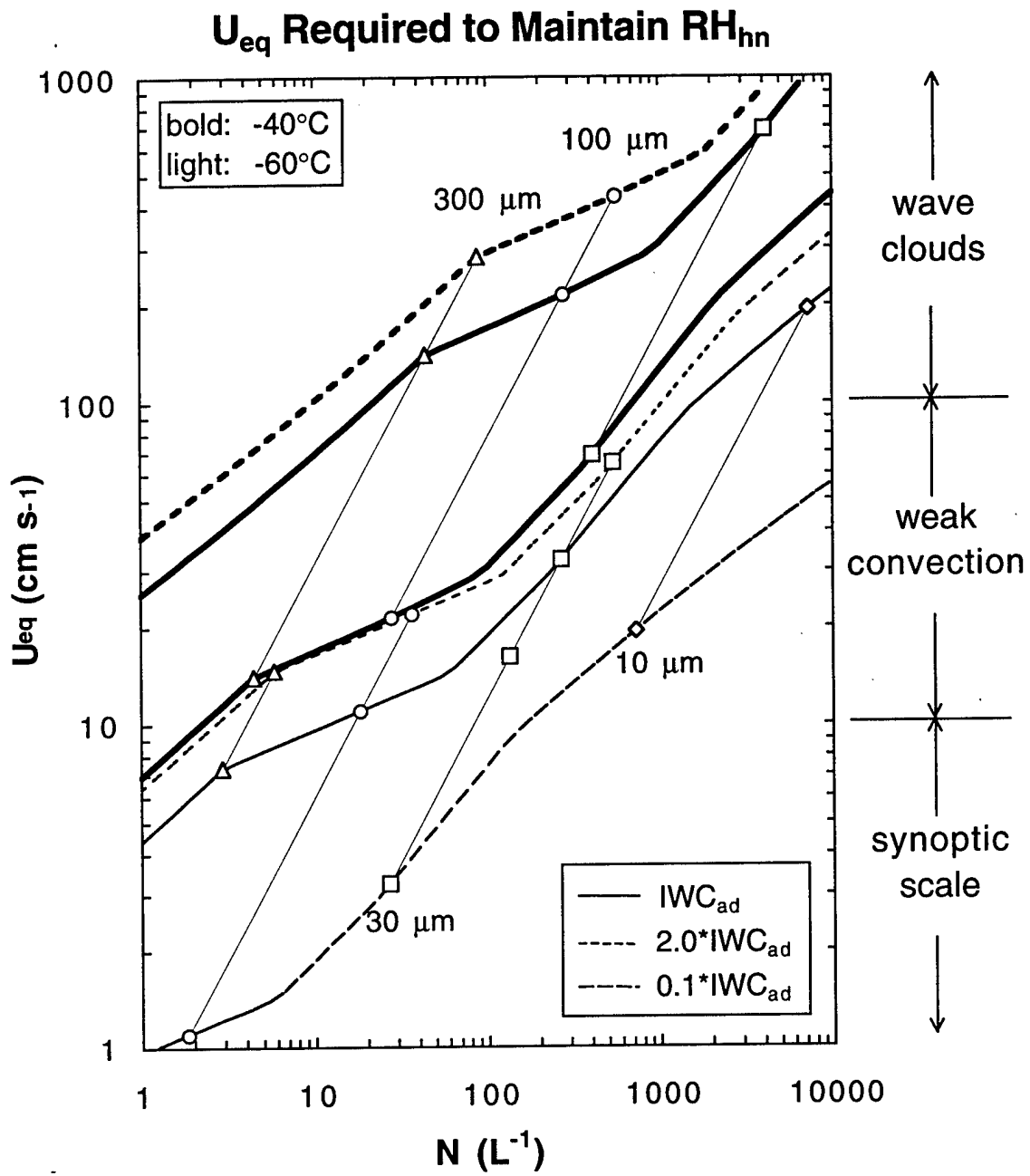
2.11



3.1

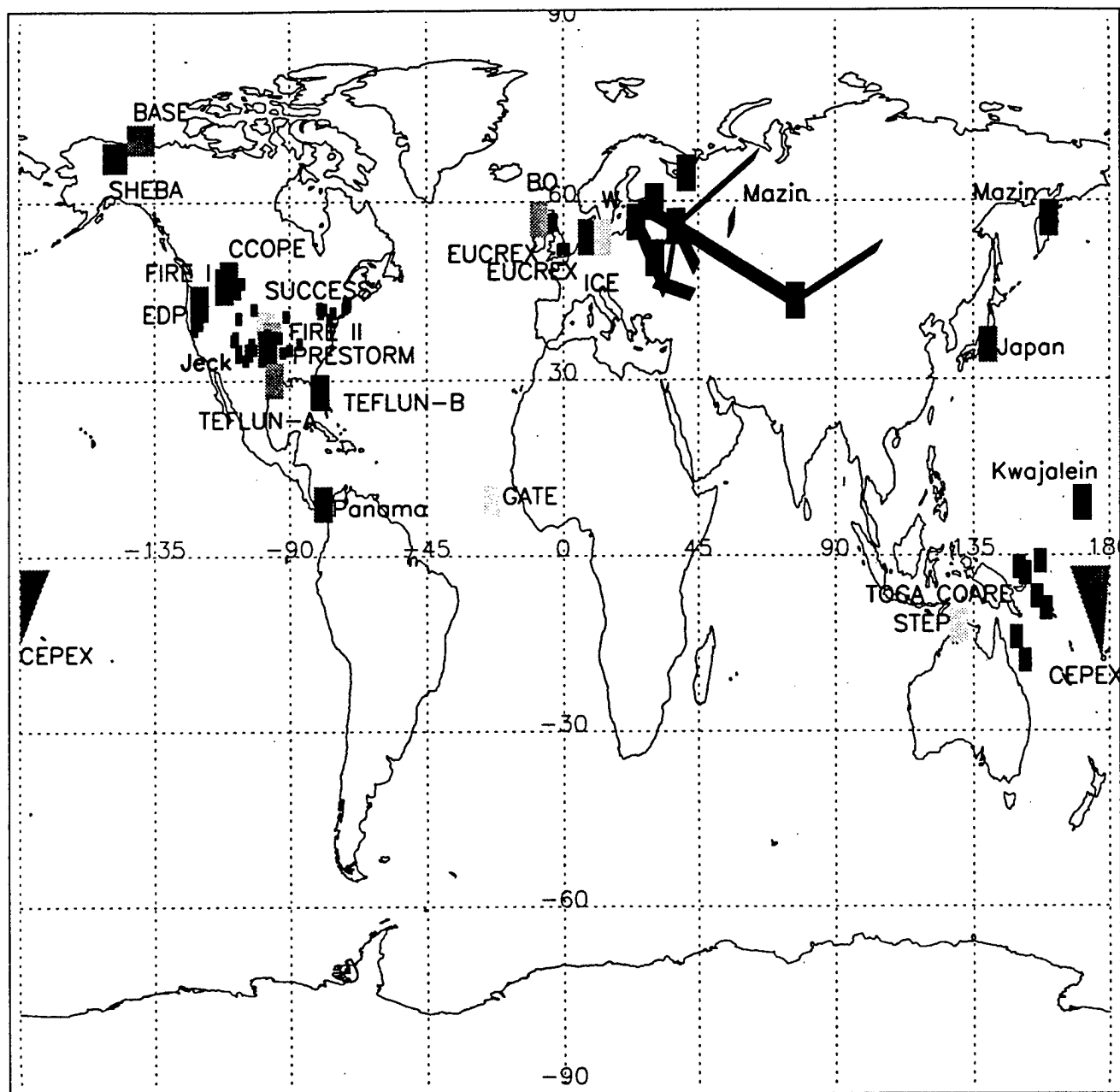


3.2



3.3

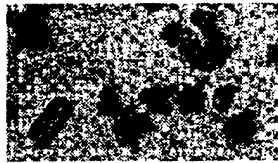
Heymsfield and McFarquhar, Fig. 1, top



Weickmann	Kwajalein	EDP	GATE	Mazin	Jeck
BO	Panama	CCOPE	PRESTORM	FIRE I	ICE
Japan	STEP	FIRE II	TOGA COARE	EUCREX	CEPEX
BASE	SUCCESS	SHEBA	TEFLUN-A	TEFLUN-B	

4.1

CIRRO CUMULUS

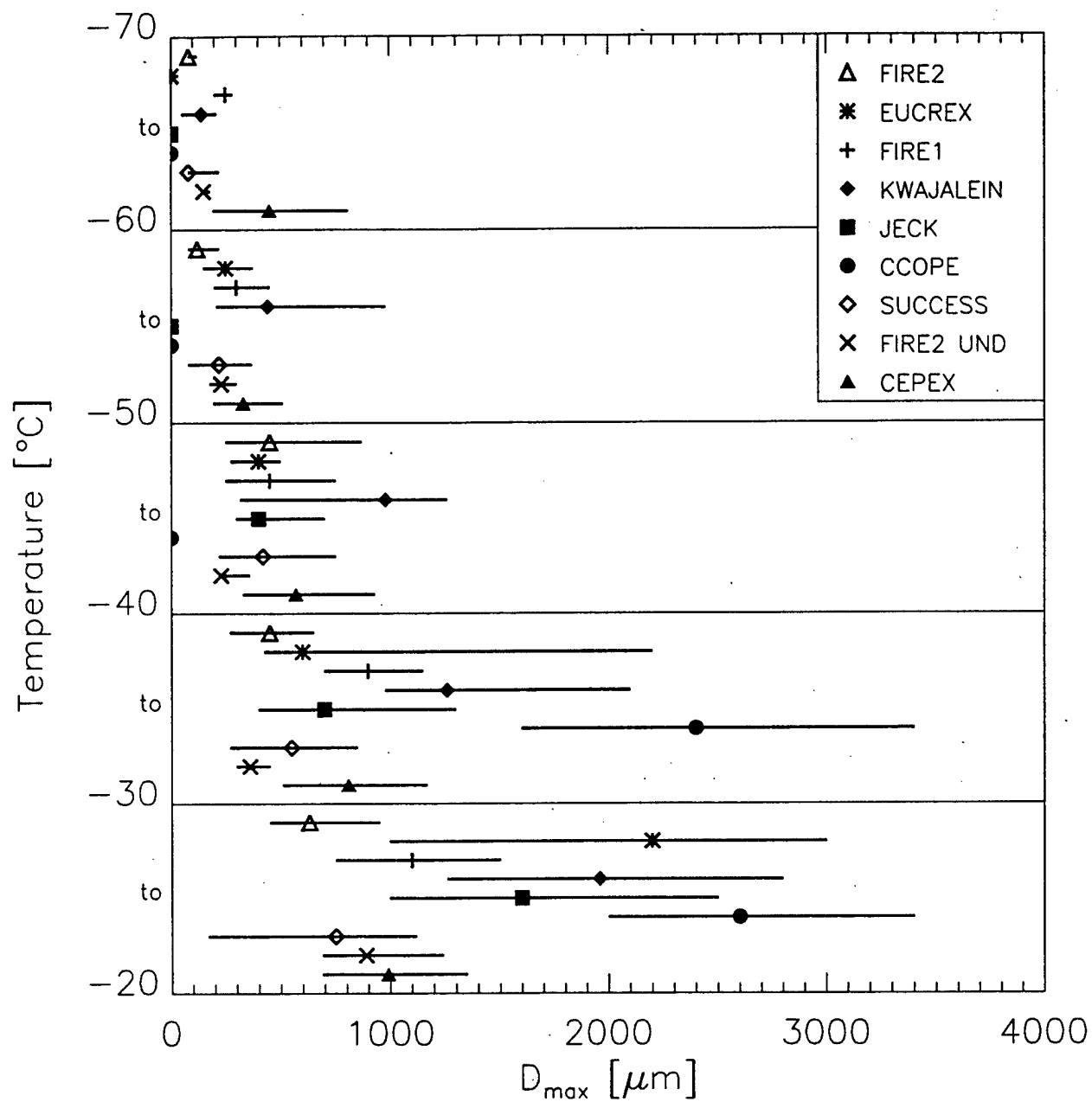


CONVECTIVE CIRRUS



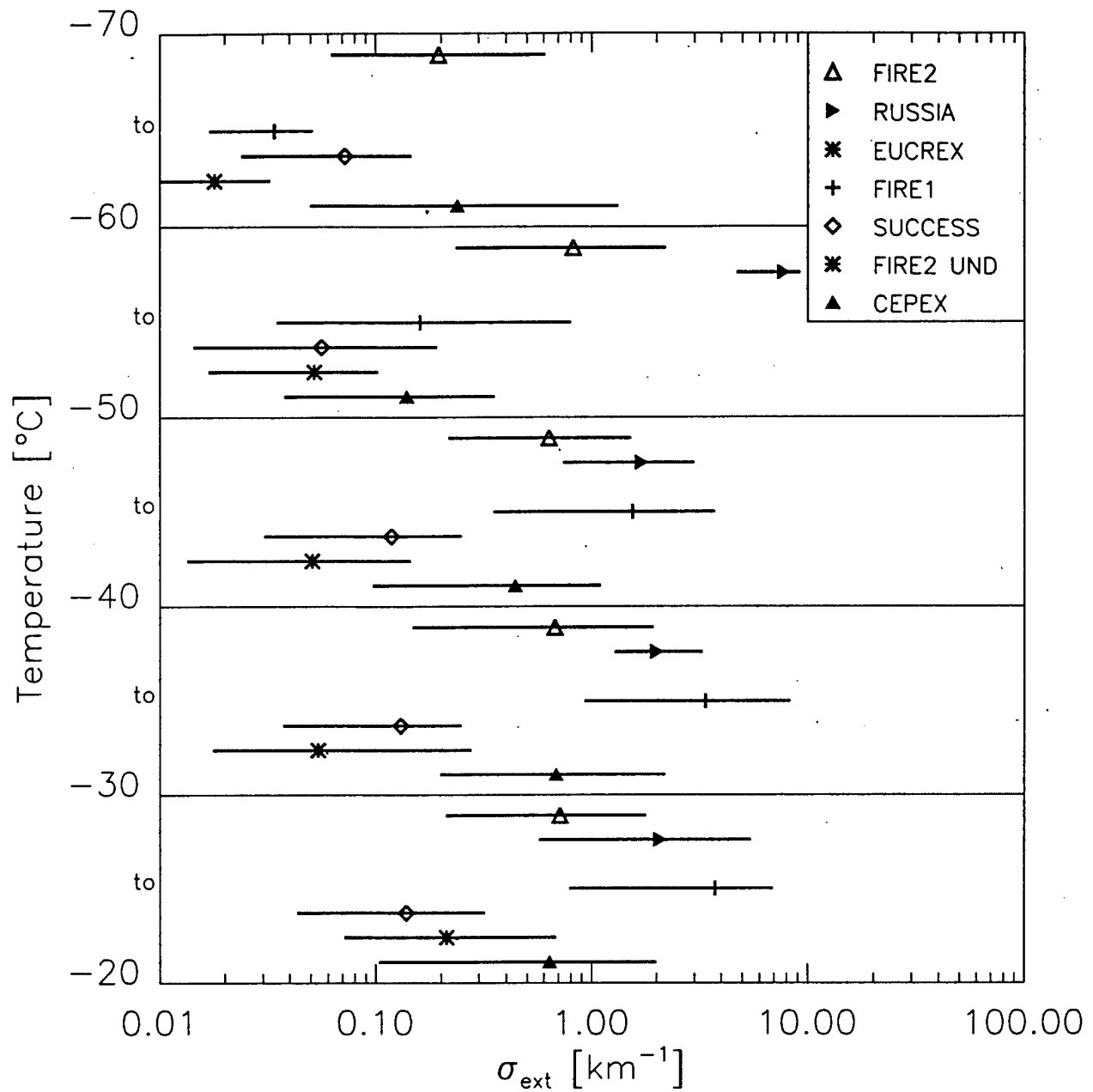
CIRRUS DENSUS





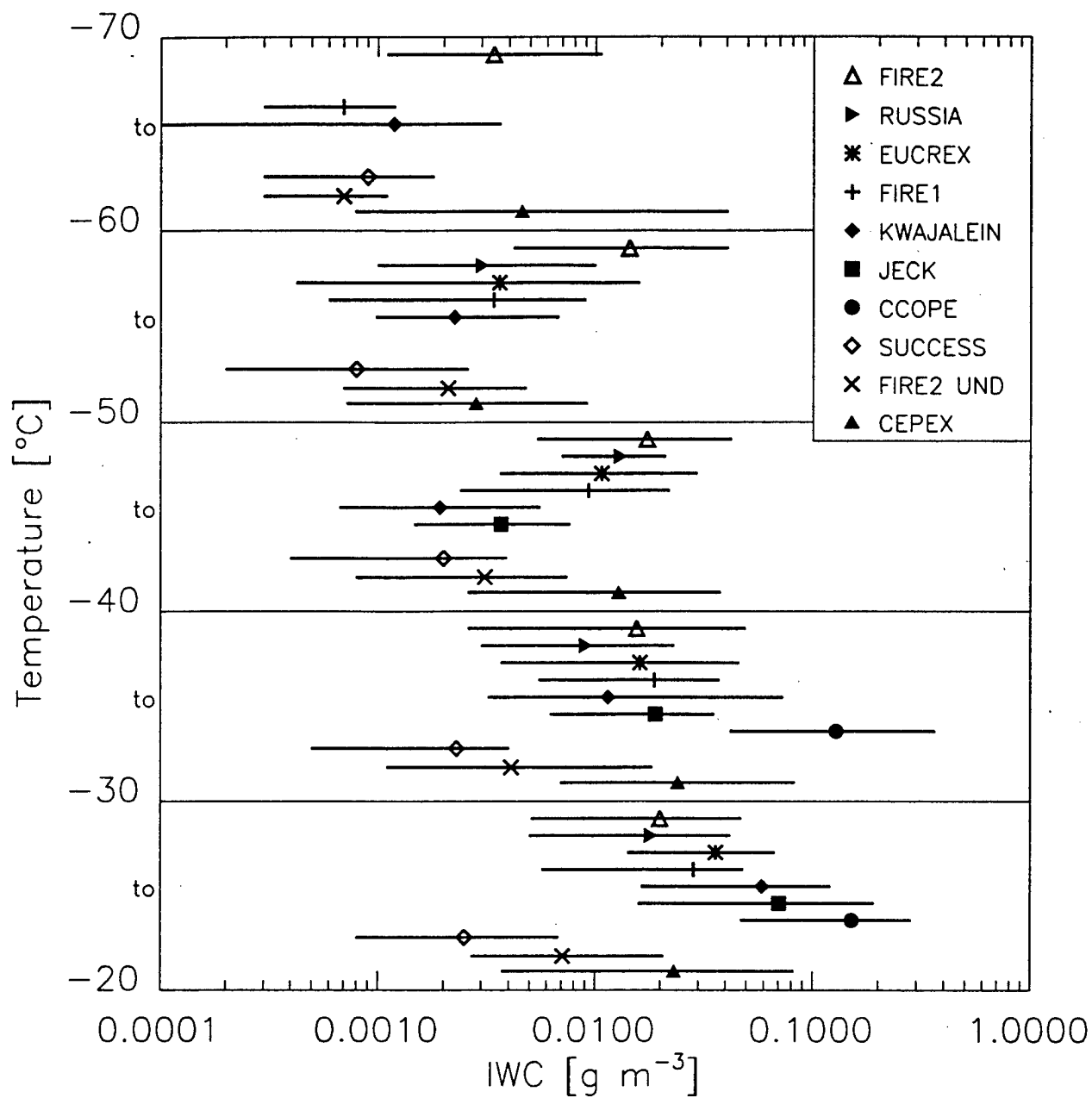
Heymsfield and McFarquhar, Fig. 7, bottom

4.3



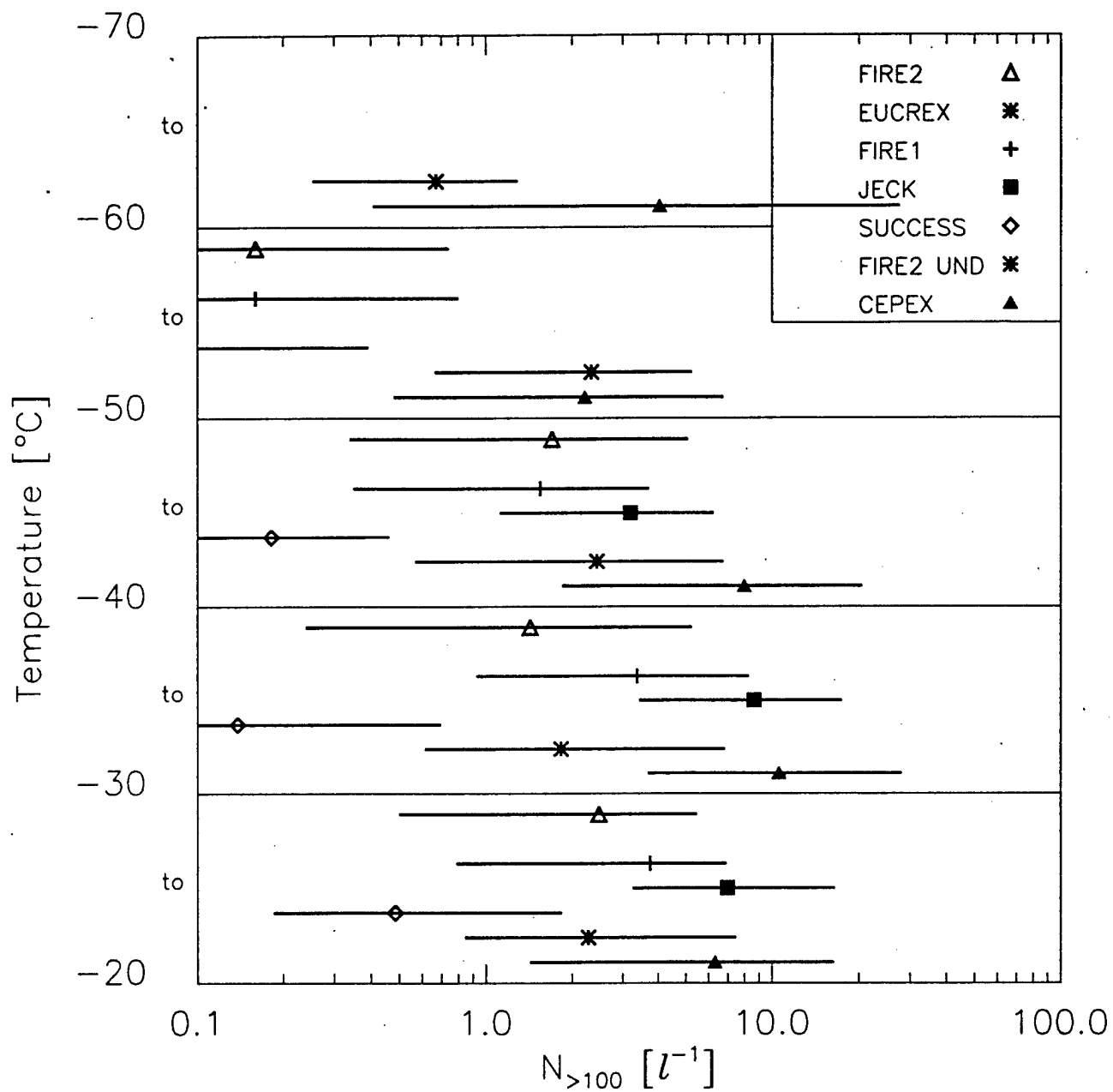
Heymsfield and McFarquhar, Fig. 8, bottom

4.4



Heymsfield and McFarquhar, Fig. 9, bottom

4.5



Hegmsfield and McFarquhar, Fig. 6, bottom

4.6

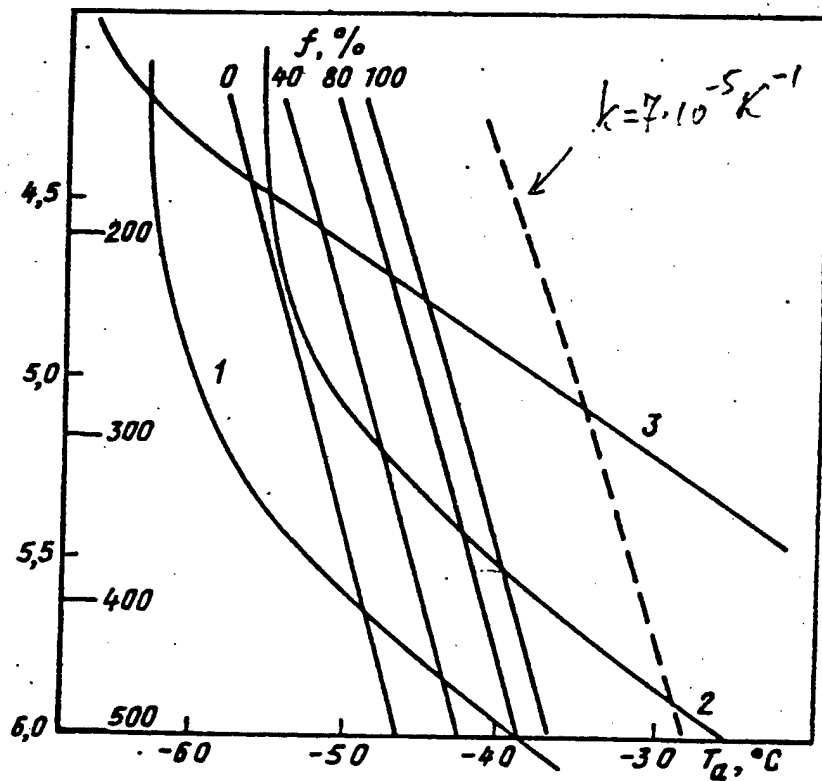


Figure 2. Diagram for determining maximum temperature of the atmosphere at which water vapor condensation is possible in the mixture of the exhaust with the air. Solid lines according to Appleman $k = 3.36 \times 10^{-5} \text{ K}^{-1}$, ($f_1 = 100\%$, $\varepsilon = 1$) dashed lines for the cases when $k = 7 \times 10^{-5} \text{ K}^{-1}$, ($f_1 = 70\%$, $\varepsilon = 0.7$). Each line $\text{RH} = 0; 40; 80$ and 100% divides all the area into two parts: left one where the processes of vapor condensation with given humidity take place and the right part where vapor condensation with given humidity of the atmosphere is impossible.

5.1

2.10

UNDERMEASUREMENT OF HIGH RELATIVE HUMIDITIES IN THE UPPER TROPOSPHERE BY VAISALA RS80-A RADIOSONDES

Larry M. Miloshevich and Andrew J. Heymsfield

National Center for Atmospheric Research, Boulder, Colorado

Samuel J. Oltmans

National Oceanic and Atmospheric Administration, Boulder, Colorado

1. INTRODUCTION

Accurate upper-tropospheric profiles of relative humidity (RH) are important to the research community for initializing numerical models, determining the temperature-dependent RH at which ice clouds are initiated, operationally predicting the formation of aircraft contrails, developing and validating radiative transfer algorithms, and validating remotely-sensed retrievals of moisture profiles. Lorenc et al. (1996) have shown that fractional cloud cover from a Numerical Weather Prediction model is very sensitive to the RH field, and assimilation of RH measurements from Vaisala radiosondes leads to underprediction of clouds and precipitation. Crook (1996) has shown that quantitative precipitation forecasts from summertime convection in Colorado are extremely sensitive to the model initialization conditions, where a 5% error in RH may over or underpredict precipitation amounts by factors of 2 or 3. A series of WMO-sponsored water vapor intercomparisons (e.g., Ivanov et al. 1991) show that variability between sondes of the same manufacturer are small, but wide differences are noted between sondes of different manufacturers, yet few studies have been conducted to assess the absolute measurement errors from operational radiosonde RH data.

Errors in the measurement of RH by Vaisala RS80-A radiosondes have been reported to increase with decreasing temperature (Anderson 1994). This paper seeks to characterize a consistently observed undermeasurement of RH by RS80-A radiosondes under conditions of high RH and cold temperature, typical of cirrus-forming conditions in the upper troposphere. Although Vaisala manufactures the more accurate "H-sensor", a study of the A-sensor is nonetheless relevant because the possibility exists to partially correct an enormous amount of historical RH data, and because RS80-A radiosondes are still widely used, in part because significant expense is involved in converting to the RS80-H data acquisition and processing system.

The Vaisala "humicap" RH sensors (both the A-polymer and the H-polymer) are capacitance-type sensors whose temperature-compensated capacitance is proportional to the RH with respect to liquid water. The A-sensors are individually factory-calibrated at +25°C and 75% and 0% RH, and are *checked but not calibrated* at +45 and -30°C at the ambient RH. The calibration curve is a second-order polynomial stated by the manufacturer to be valid between +65 and -20°C (whereas a more elaborate calibration involving ten coefficients is given for the H-sensor). This quadratic temperature-dependence may be inadequate outside this temperature range (see Fig. 4 in Anderson 1994), and RH measurement errors below -20°C may result in part from an inappropriate extrapolation of the calibration curve.

2. OBSERVATIONS

This study was initiated because detailed microphysical measurements from balloon-borne Formvar cloud particle replicators (Miloshevich and Heymsfield 1997) showed pristine ice crystals in the upper levels of cirrus clouds (indicating active ice crystal growth in an ice-supersaturated environment), while simultaneous RH measurements from Vaisala RS80-A radiosondes on the same balloon packages measured substantial ice-subsaturation (Heymsfield and Miloshevich 1995). Figure 1 shows simultaneous RH measurements from two RS80-A radiosondes and the NOAA/CMDL cryogenic frost-point hygrometer (Vömel et al. 1995), launched in tandem with the replicator. The Vaisala RH measurements are in reasonable agreement with those from the cryogenic hygrometer when the RH is low and the temperature is relatively warm, but in comparison to the cryogenic hygrometer both Vaisala sensors severely undermeasure the high RH conditions in the upper troposphere. Simultaneous microphysical measurements from the replicator show pristine and sharp-edged crystals in the upper portion of the cloud, confirming that crystals are not sublimating and the environment is at least ice-saturated. Four colaunches of the cryogenic hygrometer, replicator, and two RS80-A radiosondes into clouds show the same general characteristics illustrated in Fig. 1. The time-constant

* Corresponding author address: Larry Miloshevich,
NCAR/MMM, P.O. Box 3000, Boulder, CO 80307;
e-mail: milo@ncar.ucar.edu

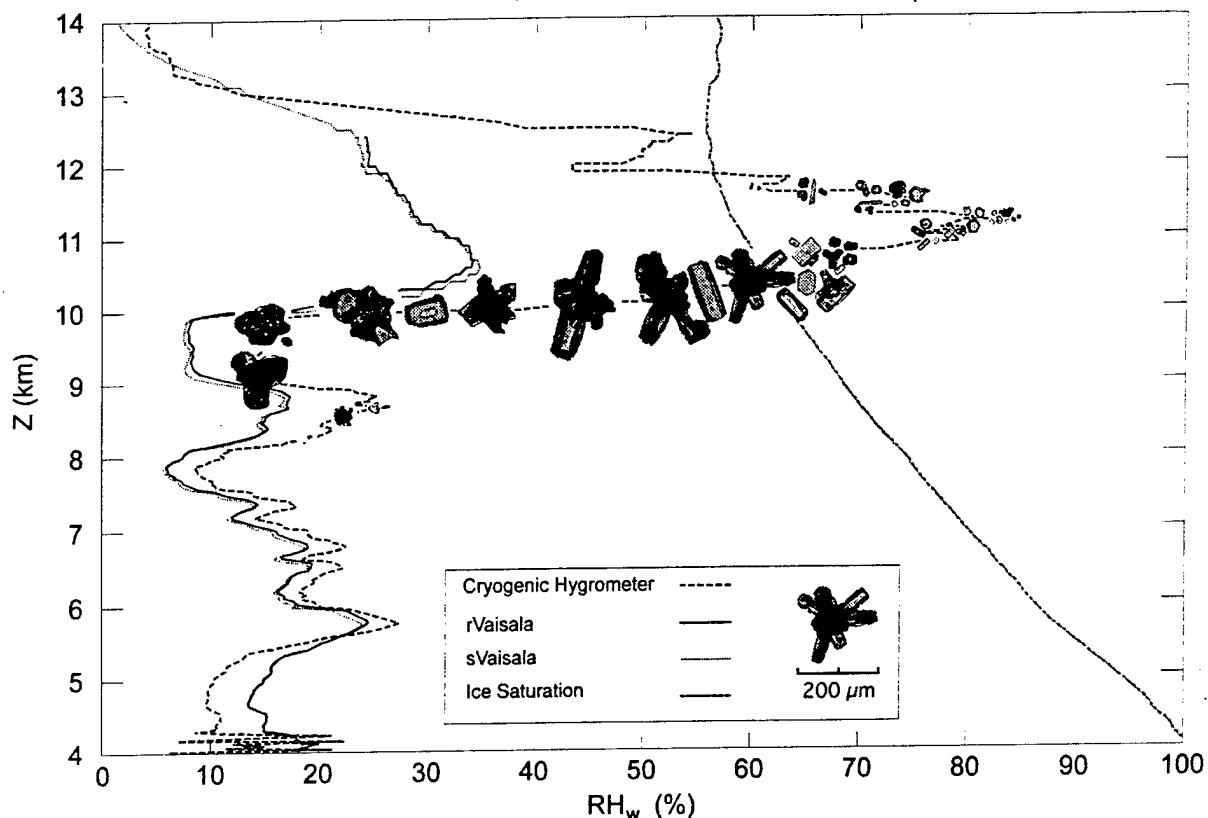


Figure 1. RH profiles through a cirrus cloud measured simultaneously by the NOAA balloon-borne cryogenic hygrometer and two Vaisala RS80-A radiosondes. Superimposed ice crystal replicas from the NCAR balloon-borne replicator show the qualitative cloud microphysical properties. An ice-saturation curve is also shown.

of the A-sensor varies from about 1 s at 0°C to 10 s at -20°C to 100 s at -43°C (Salasmaa and Kostamo 1975), and it will therefore lag behind the faster-response cryogenic hygrometer when the RH is changing rapidly at cold temperatures. However, over the 350 s time period required to sample the cloud in Fig. 1 between 10.3 and 11.8 km altitude, where ice-supersaturation is confirmed by the cryogenic hygrometer and the replicator, both A-sensors measure at least 25% ice-subsaturation, indicating that time-response does not account for the discrepancy. Note that a solid-state sensor may be inherently incapable of sensing ice-supersaturation because the surface of the sensor acts as a nucleation site upon which vapor condenses, such that air passing over this porous ice coating will be saturated with respect to ice (Anderson 1994).

The cryogenic hygrometer gives an absolute measure of vapor density based on the chilled mirror principle, where the temperature of a mirror is controlled to maintain a small and constant layer of frost coverage (below 0°C) that is optically detected. The mirror temperature under these conditions equals the frost-point temperature of the

air, and the RH is then derived from the air temperature measured by the RS80. The mirror can either be electrically heated or rapidly cooled by a cryogenic liquid that has a temperature between 30 and 90°C below the frost point to maintain the constant frost coverage, and the instrument is capable of measuring ice-supersaturation. The accuracy of the frost-point measurement is estimated to be $\pm 0.5^\circ\text{C}$, which corresponds to about $\pm 5\%$ RH in the upper troposphere. Additional uncertainty of comparable magnitude arises from the RS80 air temperature measurement used in the calculation of RH.

Figure 2 shows RH versus temperature data from five years of monthly combined launches of the NOAA cryogenic hygrometer (Panel A) and Vaisala RS80-A radiosondes (Panel B). The occurrence of substantial ice-supersaturation in the upper troposphere is not uncommon (Panel A), consistent with similar findings by Heymsfield and Miloshevich (1995) based on airborne cryogenic hygrometer measurements, and by Heymsfield et al. (1997) based on diode laser hygrometer measurements. The simultaneous RS80-A measurements

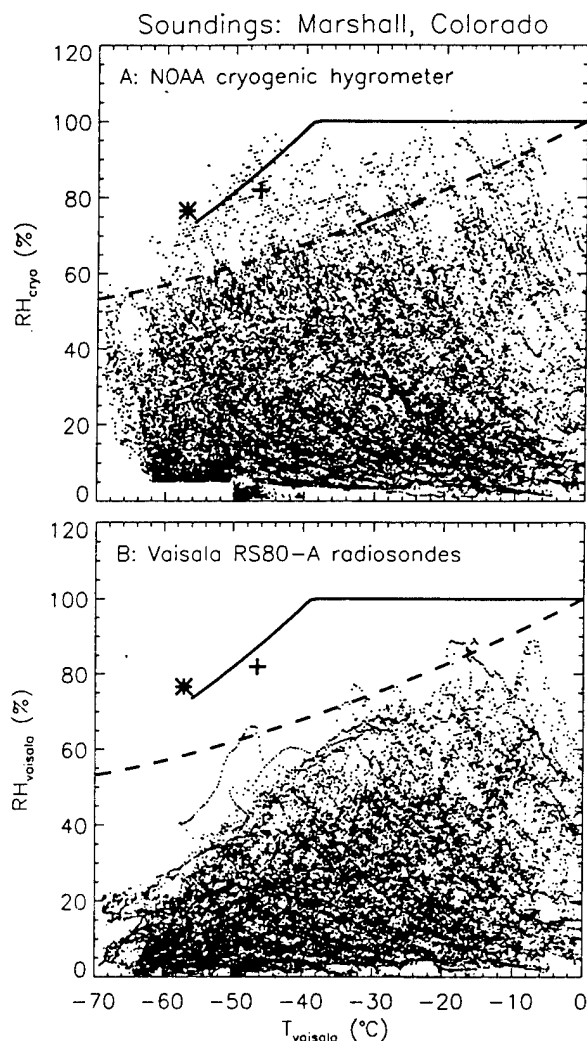


Figure 2. RH vs. temperature data from monthly combined launches of the NOAA cryogenic hygrometer (Panel A) and Vaisala RS80-A radiosondes (Panel B) between 1991 and 1996. Reference curves are ice-saturation (dashed), and the RH required to nucleate ice crystals homogeneously in orographic wave clouds (Heymsfield and Miloshevich 1995) (solid). Symbols show the peak RH measured by the cryogenic hygrometer for two flights when replicator data was also collected.

generally do not reach ice-saturation, and the RS80-A increasingly undermeasures the RH at decreasing temperatures, as judged by an imaginary envelope which overlies the bulk of the data in Panel B. The symbols show the peak RH measured by the cryogenic hygrometer during two launches where simultaneous replicator measurements showed that ice crystals were pristine and sharp-edged, confirming that the environment was at least ice-saturated.

Figure 3 shows the subset of Vaisala RH measurements (RH_v) from Fig. 2B whenever the

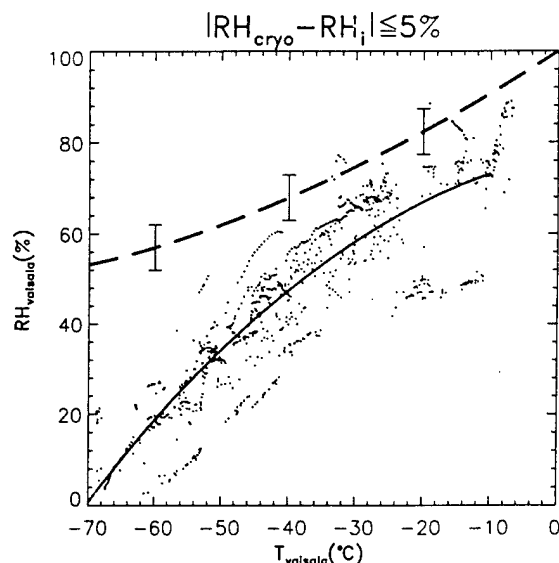


Figure 3. Vaisala RH vs. temperature measurements from the data shown in Fig. 2 for all instances when the cryogenic hygrometer measured RH values (RH_{cryo}) within $\pm 5\%$ of ice-saturation (RH_i). The dashed curve is RH_i , and vertical bars indicate the $RH_i \pm 5\%$ bounds for RH_{cryo} . The solid curve is a best-fit second-order polynomial, with correlation coefficient 0.78.

cryogenic hygrometer RH measurement (RH_{cryo}) was within $\pm 5\%$ of ice-saturation (RH_i). A temperature-dependent trend is clearly seen in the RH_v measurement error for this particular condition of high ambient RH (if RH_{cryo} is taken as equal to the ambient RH). Figure 1 showed that the measurement error depends not only on temperature but also on the ambient RH. The next section will explore an approach to correct RH_v based on the difference between the ambient RH (RH_{cryo}) and the mean RH_v as represented by the best-fit curve. The large variability in RH_v about the best-fit curve suggests that such a correction would apply only to statistical datasets rather than to individual soundings.

Profiles of RH_v from individual soundings that are known to have passed through clouds based on simultaneous replicator measurements are shown in Fig. 4, for cases of both liquid water clouds (Panel A) and ice clouds (Panel B). In liquid water clouds the peak ambient RH is presumed to be very near 100%, but three different RS80-A sensors show a systematic temperature-dependence ranging from 95% at -11°C to 83% at -28°C . Profiles through deep cirrus layers (Panel B) show a smooth and roughly constant offset from RH_i in the upper portions of the clouds (above the ice-saturated lower regions of cloud where ice crystals fall into dry air and sublimate). These smooth profiles are characteristic of in-cloud measurements and suggest

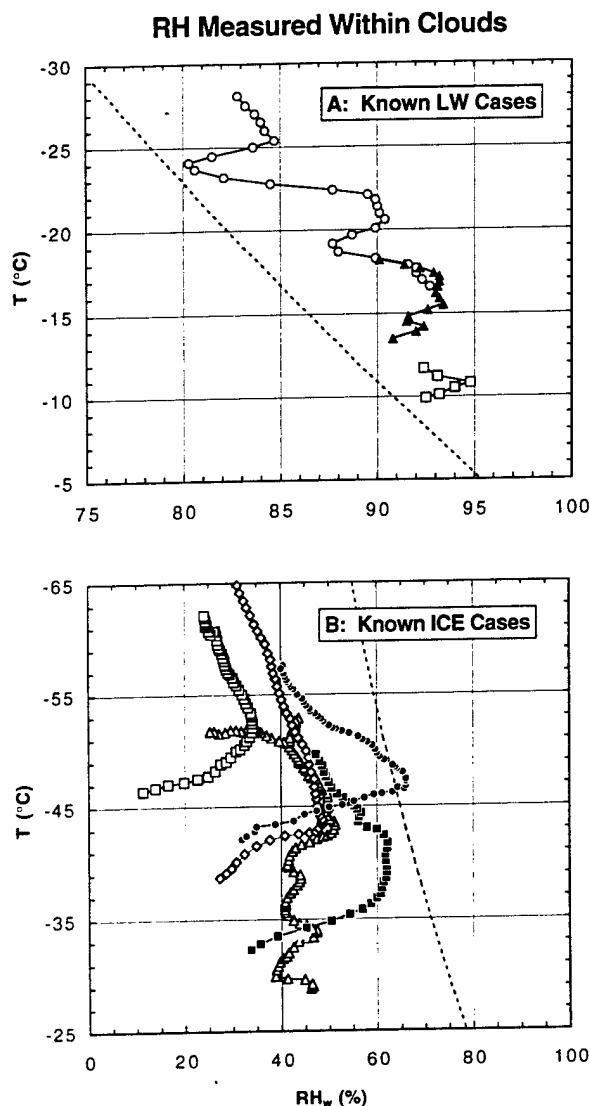


Figure 4. RH vs. temperature profiles from RS80-A sondes which passed through either liquid water clouds (Panel A) or ice clouds (Panel B), based on simultaneous replicator data. Different symbols indicate individual profiles. Dashed curve is RH_i .

that the presence of deep ice clouds can often be inferred from the shape of the RH profile. As in Fig. 1, this relatively constant RH over long periods of time suggests that the time-response of the A-sensor is not a primary factor affecting undermeasurement of high RH conditions. The variability in the magnitude and slope of the offset from RH_i between the various profiles suggests a sensor-to-sensor inaccuracy in the calibration coefficients, similar to the interpretation reported by Anderson (1994). This sensor-to-sensor variability at least partially explains the wide range of measured RH values at a given temperature in Fig. 3 for ambient conditions

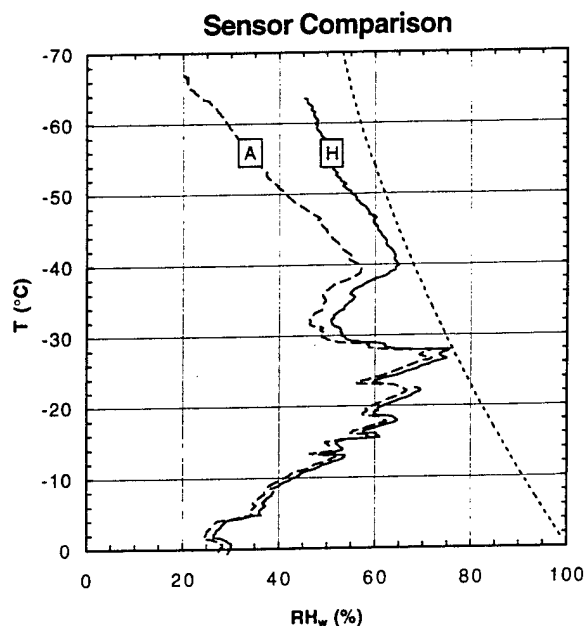


Figure 5. Simultaneous Vaisala RH vs. temperature profiles for a combined launch of an RS80-A (dashed curve) and an RS80-H (solid curve) into an orographic wave cloud on 13 Nov. 1996 near Marshall, Colorado. The short-dashed curve is RH_i .

of $RH_i \pm 5\%$. Even at temperatures above -20°C RH_i measurement errors of 5-10% are seen in liquid water clouds (Fig. 4A), although the trend in the peak RH values roughly parallels the ice-saturation curve and suggests the possibility of sensor icing by supercooled liquid water rather than a calibration problem.

A comparison of simultaneous RH profiles measured in an orographic wave cloud by both an RS80-A and an RS80-H is shown in Fig. 5. Simultaneous replicator measurements showed a deep layer of small, pristine ice crystals whose base was at about the -40°C level, as one might surmise from the shape of either RH profile. The high ice crystal concentrations in this cloud type imply that the RH should be within a few percent of RH_i (Heymsfield and Miloshevich 1993). In this case the H-sensor appears to be substantially more accurate than the A-sensor at cold temperatures, possibly due to improvements in the sensor polymer and/or to a more accurate calibration. The sensors agree within 5% RH from zero to -30°C over the range 25 to 75% RH but increasingly diverge at colder temperatures, further supporting the idea that the second-order calibration curve for the RS80-A may be inadequate at cold temperatures.

3. A CORRECTION TECHNIQUE

Since the offset from RH_i of each individually-calibrated RS80-A sensor is different (Fig. 4B), a general correction that applies to individual profiles may not be possible. Figure 6 illustrates a simple statistical correction approach based on the data shown in Fig. 2. The assumption is made that RH_{cryo} is equal to the ambient RH, and hence this correction can be no more accurate than the frost-point and air temperature measurements.

Each best-fit curve in Fig. 6A represents the set of RH_v measurements for all instances when RH_{cryo} was within $\pm 5\%$ of the labeled value, similar to Fig. 3 for $RH_{cryo} = RH_i$. The difference between a given RH_v on a best-fit curve and the corresponding RH_{cryo} (i.e., the length of the vertical lines in Fig. 6A) is the mean measurement error and the correction required for those particular ambient conditions of RH and temperature. Since the best-fit curves do not overlap (except for ice-supersaturated conditions warmer than -30°C), a unique relationship exists between the measured RH_v and the ambient RH over the temperature

range -10 to -60°C . It also appears possible to retrieve information on ice-supersaturation for temperatures colder than -30 or -40°C .

The RH correction ($\Delta RH = RH_{cryo} - RH_v$) is shown in Fig. 6B as a function of the measured RH_v , for 10°C increments in temperature. The lighter lines show points on the correction curves that yield the ambient RH indicated (given relative to RH_i). The correction generally increases with decreasing temperature and with increasing ambient RH, reaching a maximum for high RH conditions in the upper troposphere. At cold temperatures the correction can be shown to be a substantial fraction of the ambient RH, exceeding a factor of two at -60°C and a factor of 1.5 at -50°C for any ambient RH (down to at least $RH_i - 40\%$). The RS80-A becomes increasingly insensitive to changes in the ambient RH as the temperature decreases, as indicated by the steepening slope of the curves at lower temperatures. Ice-saturation cannot be distinguished from ice-supersaturation at temperatures of about -30°C or warmer, where the correction curves in Fig. 6B become vertical and are therefore ambiguous and not valid.

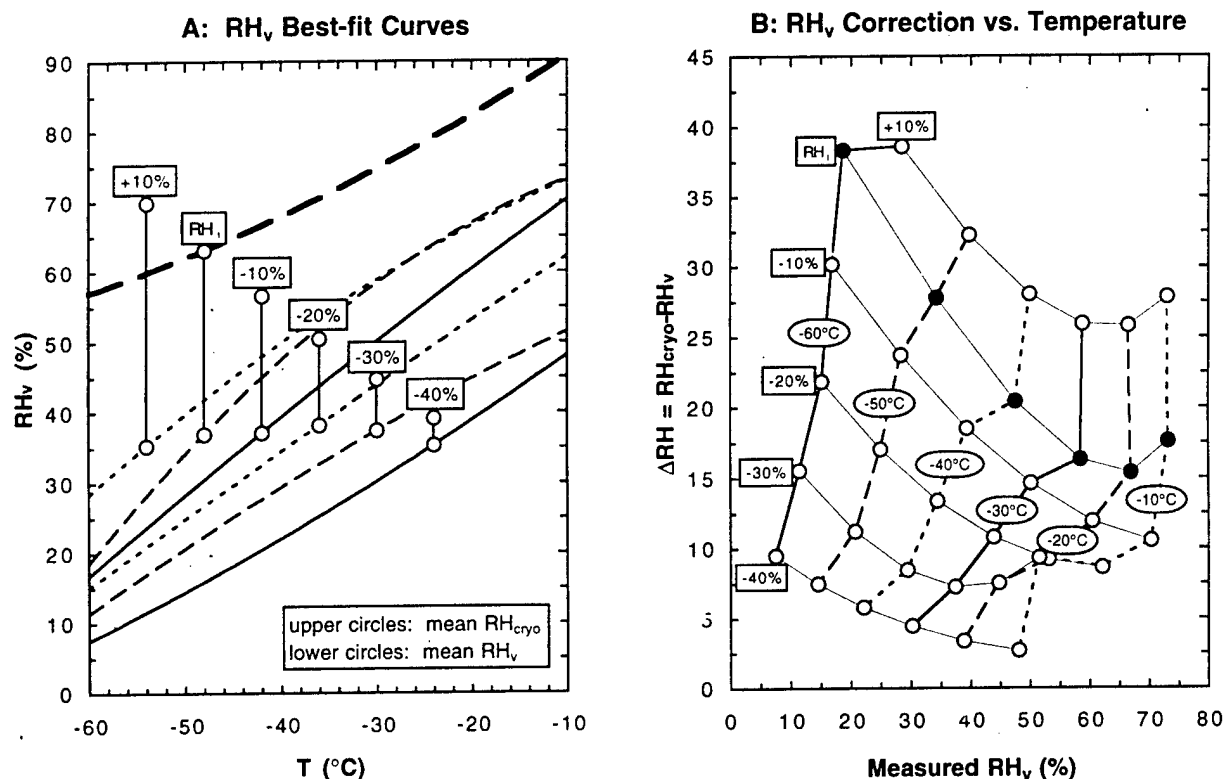


Figure 6. Panel A: Second-order best-fit curves for the RH_v data from Fig. 2, where each curve represents all points when RH_{cryo} was within $\pm 5\%$ of the labeled value (given as an offset from the bold RH_i curve). Vertical lines show the difference between RH_v values (lower points) and the corresponding RH_{cryo} values (upper points); the length of each line is the required correction to RH_v (ΔRH) given for 10°C increments in temperature (curves with oval labels). Lighter lines connect points having a given value of the corrected (ambient) RH (rectangular labels, given as an offset from RH_i).

Several improvements to this correction technique are possible. The variability in the individual RH_i points about each best-fit curve in Fig. 6A is $\pm 10\text{--}15\%$, similar to that shown in Fig. 3 and considerably greater than the $\pm 5\%$ range in the corresponding RH_{cryo} values. Greater accuracy in determining such statistical quantities as mean atmospheric water vapor concentrations would be possible using a more rigorous correction technique based on the probabilistic relationship that a given RH_i corresponds not to a unique ambient RH but to a probability distribution of ambient RH values. Also, a more accurate correction could be developed from an improved (though smaller) subset of the data in Fig. 2, by removing from the analysis points when RH_{cryo} is changing rapidly with time, reducing spread in the data that likely results from differing time-constants of the RS80-A and cryogenic hygrometer sensors. Although the accuracy of any correction approach is limited by the observed sensor-to-sensor variability and the accuracy of RH_{cryo} , the approach shown in Fig. 6 demonstrates that significant improvement in Vaisala RS80-A measurements in the upper troposphere is possible.

4. CONCLUSIONS

This paper has characterized the undermeasurement of RH by Vaisala RS80-A radiosondes at temperatures below about -10°C , based primarily on comparison with simultaneous measurements from the NOAA cryogenic frost-point hygrometer. The measurement error increases with decreasing temperature and with increasing ambient RH, and the RH_i measurements under conditions known to be at or above RH_i exhibit a sensor-dependent offset from the RH_i curve. The measurement error may result in part from an inappropriate extrapolation of the calibration to temperatures below the -20°C limit of validity, and/or from an inadequate treatment of temperature-response in the temperature-compensation electronics or the data processing algorithm.

A temperature-dependent correction approach was illustrated that applies to statistical samples of RH measurements from RS80-A radiosondes, based on the difference between simultaneous RS80-A and cryogenic hygrometer measurements. The measurement error (ΔRH) for ambient conditions of ice-saturation is about 15% at temperatures of -30°C or warmer, and increases with decreasing temperature to 38% at -60°C . The measurement error is also strongly dependent on the ambient RH, varying at -40°C from $\Delta RH=6\%$ when the ambient RH is 28% (i.e., $RH_i=40\%$) to $\Delta RH=28\%$ when the ambient RH is 78% ($RH_i=10\%$). The

large magnitude of this measurement error has potentially significant implications for the research community.

5. ACKNOWLEDGMENTS

This study was supported by NASA/FIRE-III (grant L55549D), the Air Force Office of Scientific Research (grant F49620-96-C-0024), and the Scripps Institute of Oceanography's Center for Clouds, Chemistry and Climate.

6. REFERENCES

- Anderson, P. S., 1994: A method for rescaling humidity sensors at temperatures well below freezing. *J. Atmos. Oc. Tech.*, **11**, 1388-1391.
- Crook, N.A., 1996: Sensitivity of moist convection forced by boundary layer processes to low-level thermodynamic fields. *Mon. Wea. Rev.*, **124**, 1767-1785.
- Heymsfield, A.J., and L.M. Miloshevich, 1993: Homogeneous ice nucleation and supercooled liquid water in orographic wave clouds. *J. Atmos. Sci.*, **50**, 2335-2353.
- , and L.M. Miloshevich, 1995: Relative humidity and temperature influences on cirrus formation and evolution: Observations from wave clouds and FIRE-II. *J. Atmos. Sci.*, **52**, 4302-4326.
- , L.M. Miloshevich, G. Sachse, C. Twohy, and S. Oltmans, 1997: Upper tropospheric relative humidity observations and implications for cirrus ice nucleation. *Geophys. Res. Lett.*, submitted.
- Ivanov, A., A. Kats, N. Kurnosenko, J. Nash, and N. Zaitseva, 1991: WMO International Radiosonde Intercomparison-Phase III. WMO Rep. No. 40, 135 pp.
- Lorenc, A.C., D. Barker, R.S. Bell, B. Macpherson, and A.J. Maycock, 1996: On the use of radiosonde humidity observations in mid-latitude NWP. *Meteorol. Atmos. Phys.*, **60**, 3-17.
- Miloshevich, L.M., and A.J. Heymsfield, 1997: A balloon-borne continuous cloud particle replicator for measuring vertical profiles of cloud microphysical properties: Instrument design, performance, and collection efficiency analysis. *J. Atmos. Oc. Tech.*, **14**, 753-768.
- Salasmaa, E., and P. Kostamo, 1975: New thin film humidity sensor. Preprints, *Third Symposium on Meteorological Observations and Instrumentation*, 33-38.
- Vömel, H., S.J. Oltmans, D.J. Hofmann, T. Deshler, and J.M. Rosen, 1995: The evolution of the dehydration in the Antarctic stratospheric vortex. *J. Geophys. Res.*, **100**, 13919-13926.

Andrew J. Heymsfield, Larry M. Miloshevich, Gregory M. McFarquhar, and Steven M. Aulenbach

National Center for Atmospheric Research,
Boulder, Colorado

1. INTRODUCTION

Cirrus radiative properties reflect the ice crystal shapes and size spectra integrated through the vertical cloud column. Information on the vertical distribution of cloud microphysical properties is needed to advance the representation of cirrus clouds in climate models, and to improve the accuracy of remote sensor retrievals of cirrus properties. While remote sensors have been used extensively to study the variation in cirrus properties in the vertical, in-situ characterizations of cirrus particle size and shape distributions and their variation in the vertical are extremely limited. Heymsfield and Miloshevich (1995) presented a profile of cirrus size and shape distributions in a cirrus sampled by a balloon-borne Formvar ice crystal replicator, but that preliminary analysis was insufficient for examining how the cloud radiative properties depend on the ice crystal size distributions and crystal shapes. In this study, we present analysis of two cirrus microphysical profiles sampled with the replicator, emphasizing the variability in the vertical of the cloud radiative properties and their relation to the ice crystal size distributions and crystal shapes.

2. INSTRUMENTATION

This work is based principally on measurements of ice crystal size and shape distributions acquired with balloon-borne Formvar ice crystal replicators (Miloshevich and Heymsfield 1997), during November and December 1991 near Coffeyville, Kansas, USA during FIRE-II (the First ISCCP (International Satellite Cloud Climatology Project) Research Experiment, Phase II). The replicators measure vertical profiles of ice crystal size distributions and detailed ice crystal habits (shapes) down to sizes of $10\ \mu\text{m}$ (Fig. 1).

The replicator consists of a continuous loop of transparent 35 mm film base that is pulled by a motor past a sample opening. The film base is pre-coated with Formvar (a plastic), and during ascent the Formvar is softened by a solvent just prior to exposure to the airstream, such that impacted cloud particles are preserved as 3-D Formvar replicas when the solvent evaporates. The replicators are launched with a radiosonde to acquire simultaneous meteorological data and to facilitate retrieval of the replicators. The replicator data are imaged with a

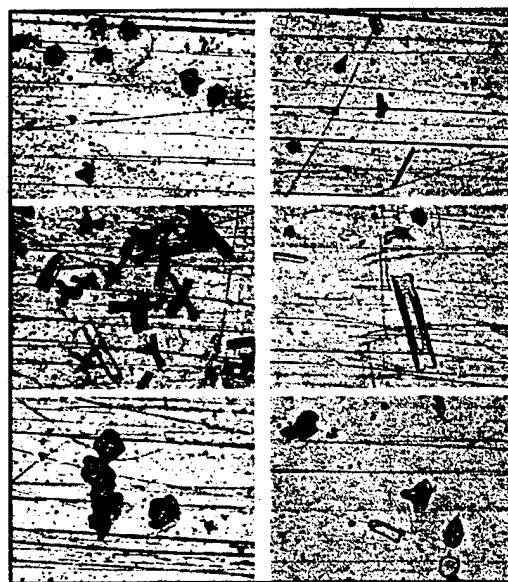


Figure 1. Example images of ice particles collected by a balloon-borne replicator during FIRE-II on 25 Nov. (left) and 5 Dec. 1991. Upper panels are from near cloud top, middle panels from the mid-cloud region, and lower panels from near cloud base.

CCD videocamera mounted on a microscope, then processed using image analysis software to yield particle counts and sizes, and direct measurements of particle cross-sectional area, aspect ratio, and perimeter. For this study, the replicator data were analyzed at intervals corresponding to about 100 m resolution in the vertical.

3. DATA AND ANALYSIS

Figure 1 illustrates that considerable variability is present in the vertical distribution of ice crystal sizes and habits in each profile. In both cases, crystals were small near cloud top, larger and with pristine habits in the mid-cloud region, and rounded with possible aggregation in the lower sublimation region (see Heymsfield and Miloshevich 1995). The pristine crystal habits are dominated by bullet rosettes for the 25 Nov. case and columns for the 5 Dec. case.

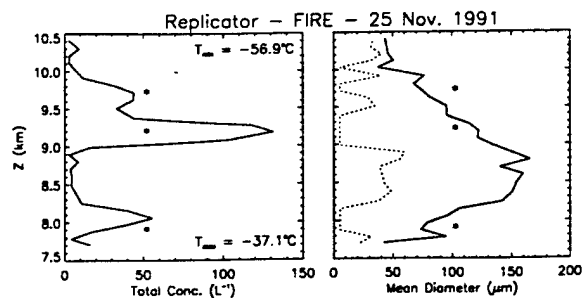


Figure 2. Vertical profiles of concentration (left) and mean and minimum crystal diameter (right) for the 25 Nov. case (diameter refers to the maximum crystal dimension). Asterisks give the locations for the images shown in Fig. 1. Cloud top and cloud base temperatures are also given.

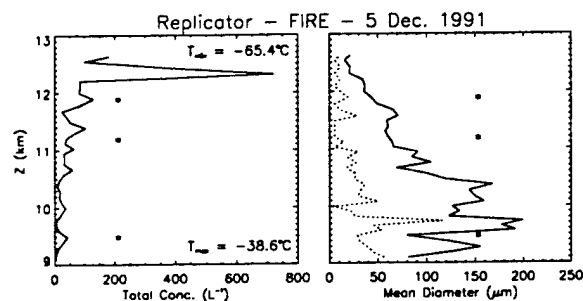


Figure 3. Same as Fig. 2, but for the 5 Dec. case.

The locations of the images in Fig. 1 are shown in Figs. 2 and 3, on vertical profiles of total ice crystal concentration (N) and mean (number-weighted) diameter. Mean particle size increases downward in both clouds, with maximum crystal sizes (not shown) of $600 \mu\text{m}$ near cloud base. Note the high concentrations of small crystals near cloud top in the 5 Dec. case, whose impact on the cloud radiative properties will be seen later.

Ice crystal cross-sectional areas are measured directly from the image data by counting pixels. The "area ratio" (the cross-sectional area of a particle divided by the area of a circle that encloses the maximum dimension (D) of the particle) provides an indication of the circularity of the crystal cross-section, and therefore gives an indication of crystal shape (Figs. 4 and 5). In general, the particles are more circular at the smaller sizes, meaning that for their sizes they contain a relatively larger cross-sectional area compared with the larger particles. Although a distinct trend in the area ratio vs diameter relationship can be seen, the variability is large, suggesting that it may be inadequate to represent cirrus in numerical calculations as being composed of a single crystal shape or aspect ratio.

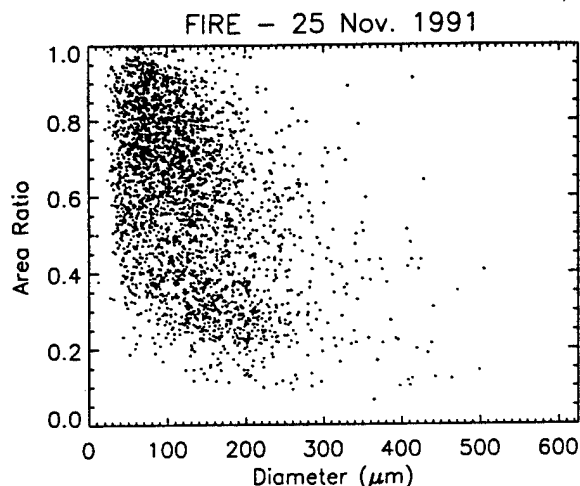


Figure 4. Area Ratio (as defined in the text) for all crystals analyzed for the 25 Nov. case, shown as a function of crystal diameter.

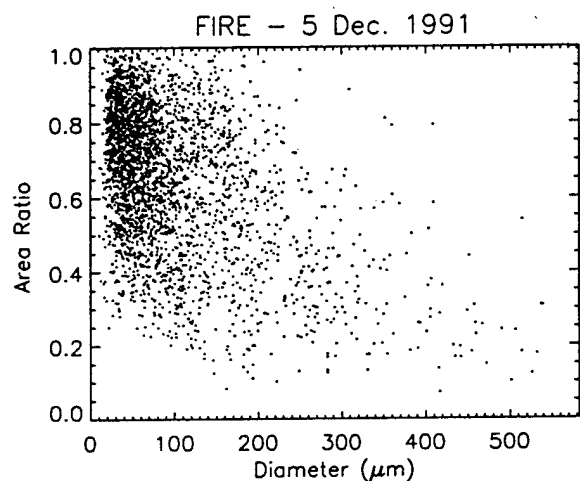


Figure 5. Same as Fig. 4, but for the 5 Dec. case.

The contribution by different crystal sizes to the extinction coefficient (i.e., the distribution of cross-sectional area calculated as a function of particle size, $\Sigma N(D)A(D)$) is indicated as a function of position in the cloud in Figs. 6 and 7. In both clouds, half the extinction at a given level (i.e., the "0.5" curve) is contributed by particles smaller than $50 \mu\text{m}$ in the upper 10% of these clouds and by particles smaller than $100 \mu\text{m}$ in the upper third of the clouds, whereas the bulk of the extinction in the lower two-thirds of each cloud is contributed by particles in the size range $100\text{--}300 \mu\text{m}$.

Although small particles dominate the extinction in the uppermost levels of the clouds, they do not necessarily dominate the extinction in the

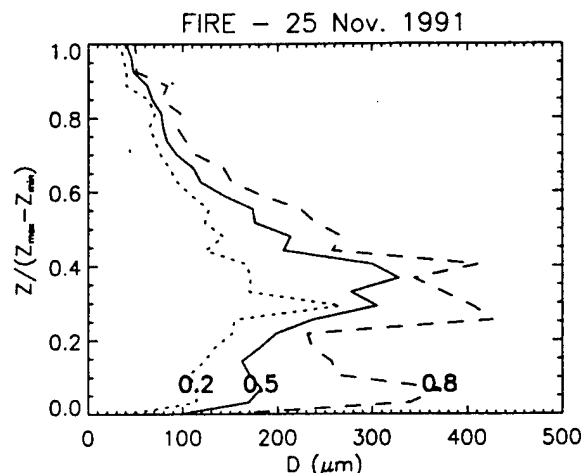


Figure 6. Normalized altitude profile on 25 Nov. of the fraction of total particle cross-sectional area A (as labeled on curves), calculated at each level as the sum of the cross-sectional areas by particle size, $\Sigma N(D)A(D)$.

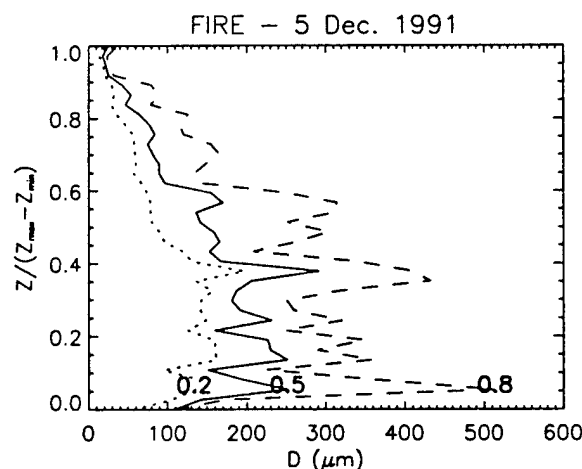


Figure 7. Same as Fig. 6, but for the 5 Dec. case.

clouds as a whole, as seen in Figs. 8 and 9, which shows the contribution of each cloud level to the cloud optical depth (τ , the integration of the extinction coefficient from cloud top downward). In the 25 Nov. case, the upper third of the cloud contributes only about 12% to τ . Even the abundance of small crystals near cloud top in the 5 Dec. case (see Fig. 3) does not dominate the optical properties of the cloud, indicating that the much lower concentrations of larger crystals are radiatively more important than the small crystals. We also note that the optical depth of $\tau=1.1$ on 5 Dec. is in good agreement with simultaneous direct measurements of τ at the surface from a sunphotometer at a wavelength of $0.5 \mu\text{m}$ (Shiobara et al. 1996).

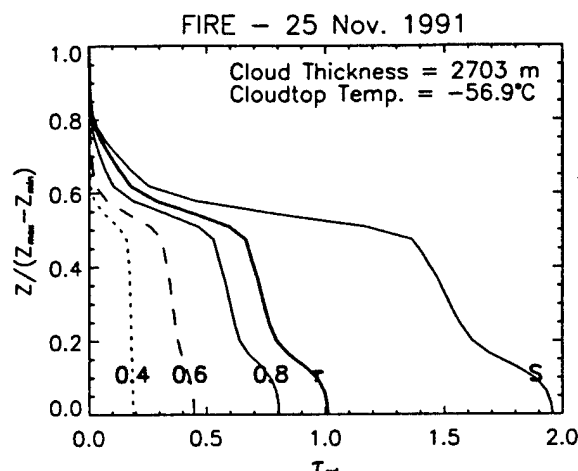


Figure 8. Normalized altitude profile of cloud optical depth (τ) on 25 Nov. Numeric labels show contributions to τ from crystals with area ratios less than the labeled numbers. The curve labeled "S" is calculated from the size distributions as if the particles were spheres.

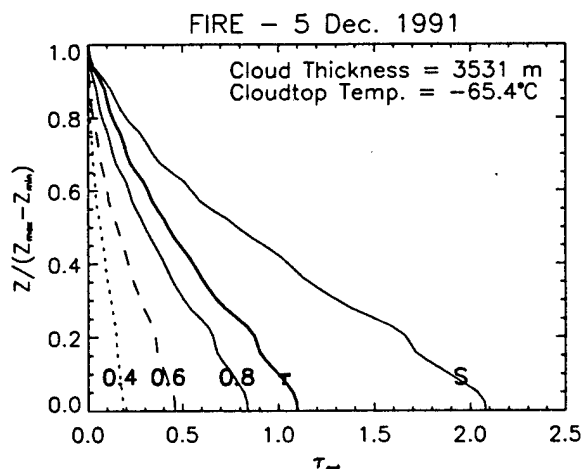


Figure 9. Same as Fig. 8, but for the 5 Dec. case.

The contributions to τ at each level in Figs. 8 and 9 are also partitioned by area ratio, providing some indication of the relative contributions of different crystal shapes or aspect ratios to τ . In the upper third of each cloud, crystals with a somewhat circular effective cross-section (area ratio >0.6) dominate the extinction. However, for the cloud as a whole (i.e., at $Z=0$) crystals with a distinctly non-circular effective cross-section (area ratio <0.6) contribute nearly half to the total extinction. If the area ratio of all particles in the size distribution was 1.0 (i.e., the cross-section is a disk), then the optical depth would have been about twice as large as observed from the directly-measured cross-sectional

areas ("S" in the figures), thus the effective area ratio of the cloud as a whole is about 0.5.

The contribution to τ from different particle sizes is more clearly seen in Figs. 10 and 11, which show the fraction of τ resulting from particles smaller than a given diameter. Particles between 10 μm (the detection threshold of the replicator) and 50 μm contribute minimally to τ (15% on 5 Dec. and 2% on 25 Nov.). About two-thirds of τ is contributed by particles between 50 and 250 μm .

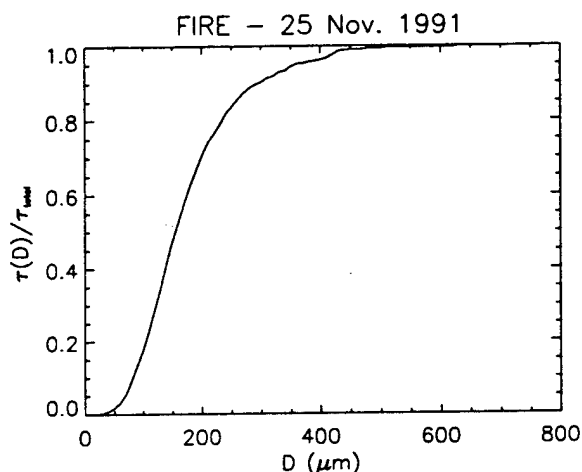


Figure 10. Fraction of the total optical depth (τ) on 25 Nov. contributed by crystals smaller than diameter D .

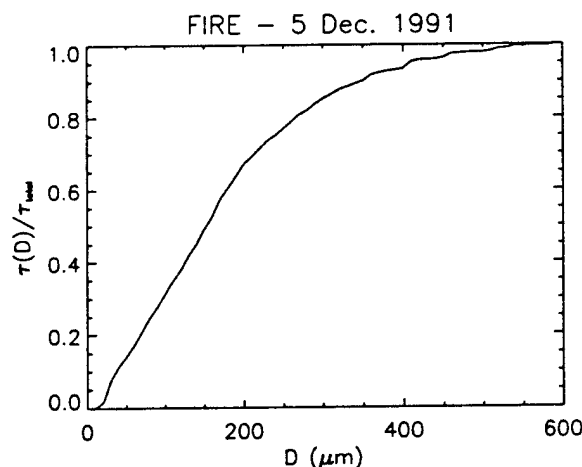


Figure 11. Same as Fig. 10, but for the 5 Dec. case.

4. SUMMARY AND CONCLUSIONS

This article has presented vertical profiles of cirrus microphysical data collected by balloon-borne Formvar ice crystal replicators. We have examined the particle sizes, shapes, and locations in these cirrus clouds that contribute most to the extinction coefficients and cloud optical depth, and

hence to the cloud radiative properties. The main findings of this study are summarized as follows:

- Mean particle size increases downward in both clouds from tens of microns at cloud top to 150-200 μm in the mid-cloud region, with maximum crystal sizes near cloud base of about 600 μm .
- Ice crystal cross-sectional areas were measured directly, and the calculated area ratios showed a tendency toward increasing circularity of crystals with decreasing size. Area ratios varied widely, and so a single crystal shape or aspect ratio may not adequately represent cirrus clouds.
- Sizes contributing most to the extinction coefficients increase downward, from <50 μm at cloud top to >150 μm at mid-cloud and lower levels.
- Most of the contribution to the cloud optical depth occurs in the lower two-thirds of the clouds.
- The cloud optical depth is half what it would be if calculated from the size distributions with the assumption that the crystals had circular cross-sections, so the effective area ratio for each cloud as a whole is about 0.5.
- Particles <50 μm contribute minimally to the total cloud optical depth, and about two-thirds of the contribution to τ in both clouds is from particle sizes in the range 50-250 μm .

Further study will center on similar analysis of additional replicator profiles in cirrus to examine the generality of these results, and on radiative transfer calculations to assess the contribution of particle sizes, shapes, and position in cloud to the cloud albedos.

5. ACKNOWLEDGMENTS

This study was supported by NASA/FIRE-III (grant L55549D), and the Air Force Office of Scientific Research (grant F49620-96-C-0024).

REFERENCES

- Heymsfield, A.J., and L.M. Miloshevich, 1995: Relative humidity and temperature influences on cirrus formation and evolution: Observations from wave clouds and FIRE-II. *J. Atmos. Sci.*, **52**, 4302-4326.
- Miloshevich, L.M., and A.J. Heymsfield, 1997: A balloon-borne continuous cloud particle replicator for measuring vertical profiles of cloud microphysical properties: Instrument design, performance, and collection efficiency analysis. *J. Atmos. Oc. Tech.*, **14**, 753-768.
- Shiobara, M., J.D. Spinhirne, A. Uchiyama, and S. Asano, 1996: Optical depth measurements of aerosol, cloud, and water vapor using sun photometers during FIRE Cirrus IFO II. *J. Atmos. Sci.*, **35**, 36-46.

Upper-tropospheric relative humidity observations and implications for cirrus ice nucleation

Andrew J. Heymsfield, Larry M. Miloshevich, and Cynthia Twohy
National Center for Atmospheric Research, Boulder, CO

Glen Sachse
NASA Langley Research Center, Hampton, VA

Samuel Oltmans
NOAA Climate Monitoring and Diagnostics Laboratory, Boulder, CO

Abstract. Relative humidity (RH) measurements acquired in orographic wave cloud and cirrus environments are used to investigate the temperature-dependent RH required to nucleate ice crystals in the upper troposphere, $RH_{nuc}(T)$. High ice-supersaturations in clear air — conducive to the maintenance of aircraft contrails yet below RH_{nuc} and therefore insufficient for cirrus formation — are not uncommon. Earlier findings are supported that RH_{nuc} in mid-latitude, continental environments decreases from water-saturation at temperatures above -39°C to 75% RH at -55°C . Uncertainty in determining RH_{nuc} below -55°C results in part from size detection limitations of the microphysical instrumentation, but analysis of data from the SUCCESS experiment indicates that RH_{nuc} below -55°C is between 70 and 88%. A small amount of data acquired off-shore suggests the possibility that RH_{nuc} may also depend on properties of the aerosols.

1. Introduction

Uncertainties in the radiation and moisture budgets in climate models result in part from inadequate knowledge of cirrus microphysical properties and the thermodynamic conditions required to nucleate cirrus ice crystals. This study examines the temperature-dependent relative humidity required to nucleate ice crystals in the upper troposphere, $RH_{nuc}(T)$. This condition determines cirrus initiation and frequency of occurrence, influences cirrus microphysical and radiative properties, and thereby influences cirrus effects on climate.

Ice-supersaturation in the upper troposphere has long been inferred from the observation of long-lasting aircraft contrails in otherwise clear air [e.g., Brewer, 1946], but only recently has instrumentation been capable of accurately measuring ice-supersaturation from aircraft at cold temperatures. The contrail shown in Fig. 1 was produced in ascending air upwind of an orographic wave cloud by the NASA DC-8 aircraft during SUCCESS (the "Subsonic aircraft: Contrail and Cloud Effects Special Study" experiment). Some de-

gree of ice-supersaturation must have been present in the clear air to maintain the contrail, but a higher ice-supersaturation must be required to produce ice crystals from the ambient aerosol population.

Heymsfield and Miloshevich [1995, hereafter "HM"] used measurements in orographic wave cloud and cirrus environments from FIRE-II (the First ISCCP Research Experiment, Phase II) to place upper and lower limits on RH_{nuc} in the temperature range -35 to -55°C . Orographic wave clouds are well-suited for studying ice nucleation because the airflow is relatively laminar and the RH increases continuously via vertical lifting toward RH_{nuc} at the upwind cloud boundary. Furthermore, ice crystals in wave clouds are carried downwind rather than falling through the ascending air as in cirrus, allowing the ice nucleation conditions to be sampled repeatedly [Heymsfield and Miloshevich, 1993]. The peak RH observed during penetrations into the upwind edge of wave clouds occurs when the vapor depletion rate from growth of recently-nucleated ice crystals is equal to the vapor supply rate from cooling due to vertical velocities of several m s^{-1} , and represents an upper limit to RH_{nuc} since ice crystals must have nucleated prior to the peak and therefore at a lower RH. HM found that these peak RH values — their empirical " $RH_{hn}(T)$ " curve — varied from water-saturation at temperatures above -39°C to 75% RH (with respect to water) at -55°C . HM also determined a lower bound on RH_{nuc} in the temperature range -35 to -47°C — about 10% below the RH_{hn} curve — based on the maximum RH measured in "clear air" in a non-orographic environment during FIRE-II. In this article we use RH and microphysical data from balloon launches near Boulder, Colorado and from the FIRE-II and SUCCESS experiments to further explore bounds on $RH_{nuc}(T)$, particularly at colder temperatures. Most data presented in this paper represent mid-latitude, continental, non-convective environments.

2. Observed Ice Nucleation Conditions

2.1. Balloon-borne Measurements

Ice-supersaturations of 20-30% have been observed in clear air and in regions of low ice crystal concentration near the tops of cirrus [HM]. RH measurements are shown in Fig. 2 from monthly launches of the NOAA balloon-borne cryogenic hygrometer [Oltmans

Copyright 1998 by the American Geophysical Union.

Paper number 98GL01089.
0094-8534/98/98GL-01089\$05.00

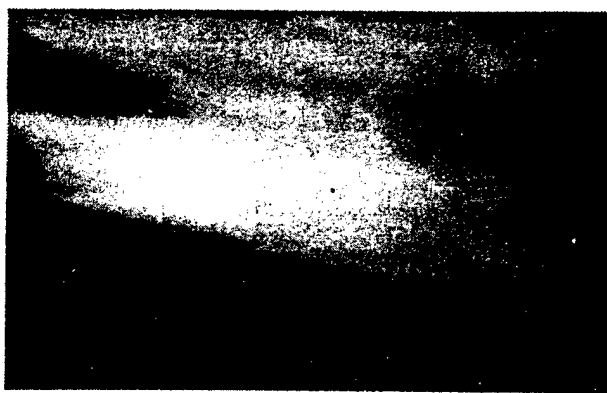


Figure 1. Contrail produced upwind of an orographic wave cloud near Boulder, Colorado on 2 May 1996. Photo courtesy of Dan Breed (NCAR/MMM).

and Hoffman, 1995]. The highest RH points below -40°C are consistent with RH_{hn} , within the instrument's estimated accuracy of 5-10%. Although these launches were preferentially conducted in clear-air conditions, some launches are known to have passed through cirrus and therefore the data does not necessarily represent RH_{nuc} . However, Fig. 2 demonstrates that high ice-supersaturations are not uncommon.

2.2. FIRE-II

Clear-air RH data from FIRE-II (not previously reported by HM) are shown in Fig. 3A, where in this case "clear air" means an absence of ice crystals larger than the $50\text{ }\mu\text{m}$ detection threshold of a Particle Measuring Systems 2D-C probe for at least two seconds prior to and after an accepted data point. Since the detection threshold of the 2D-C probe is so large, data points that lie above the RH_{hn} curve were examined using simultaneous particle collection data from a Video Ice Particle Sampler (VIPS) [McFarquhar and Heymsfield, 1996]. These points were either verified to be free of ice crystals larger than the $5\text{--}10\text{ }\mu\text{m}$ detection threshold of

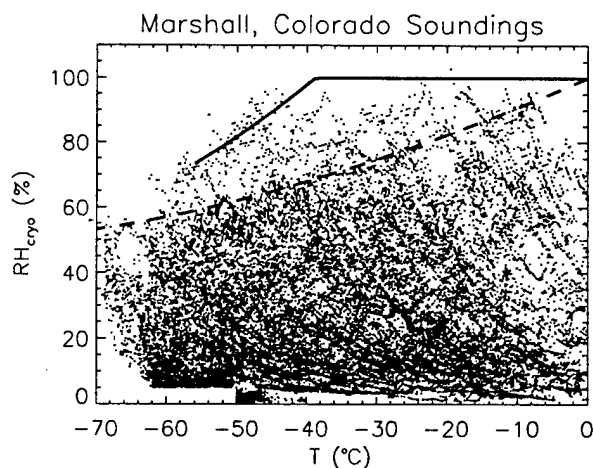


Figure 2. RH measurements from the NOAA cryogenic hygrometer for monthly balloon launches between 1991 and 1996 near Boulder, Colorado, shown as a function of temperature. Solid line is RH_{hn} from HM; dashed line is ice-saturation.

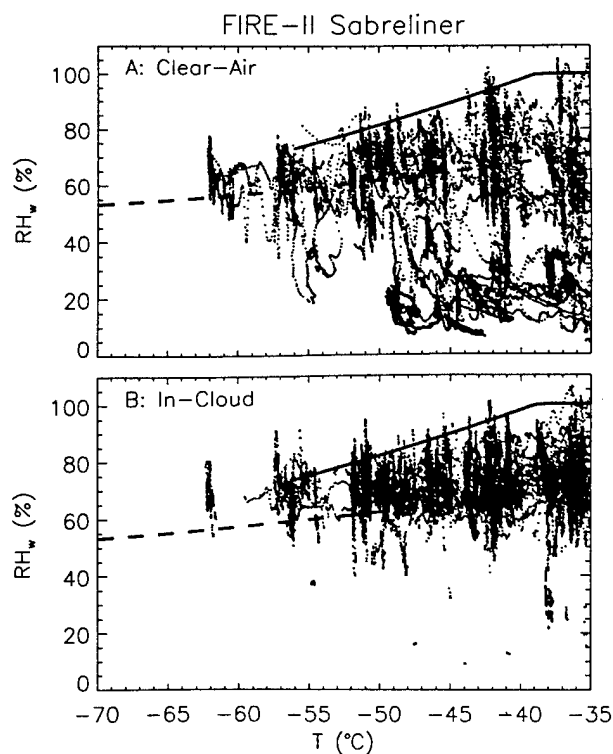


Figure 3. RH measurements from a cryogenic hygrometer on the NCAR Sabreliner aircraft during FIRE-II, shown as a function of temperature. Panel A: clear-air data as determined from 2D-C measurements; Panel B: in-cloud data. Solid line is RH_{hn} ; dashed line is ice-saturation.

the VIPS, or the images showed extremely low ice crystal concentrations. The accuracy of the NCAR cryogenic hygrometer used to make the RH measurements is $\pm 1^{\circ}\text{C}$ in the frost-point temperature, or about 10% in RH at upper-tropospheric air temperatures [HM].

The highest clear-air RH data points are 5-7% above RH_{hn} over the temperature range for which RH_{hn} is defined. The RH at -62°C in Fig. 3A reaches 78%, therefore RH_{nuc} is not given by extrapolation of the RH_{hn} curve below -55°C . However, slow ice crystal growth rates at cold temperatures may have resulted in an erroneous "clear air" classification of some high-RH points since undetectable ice crystals smaller than $5\text{--}10\text{ }\mu\text{m}$ may have recently nucleated. If so, the resulting overestimate of RH_{nuc} should be small relative to wave cloud environments because the vertical velocities are lower and therefore the increase in RH while crystals grow to detectable sizes is less. The in-cloud cirrus data (Fig. 3B) demonstrate that the RH can increase substantially above RH_{nuc} . High in-cloud RH values are more likely to occur when the vertical velocity (and hence the vapor supply rate) is high, or when the ice crystals are small or the temperature is low, both of which result in slow ice crystal growth rates and therefore low vapor depletion rates.

2.3. SUCCESS

Figure 4 shows RH in clear air measured by a diode laser hygrometer (DLH) [Vay et al., 1997] for three flights during SUCCESS, where in this case "clear air"

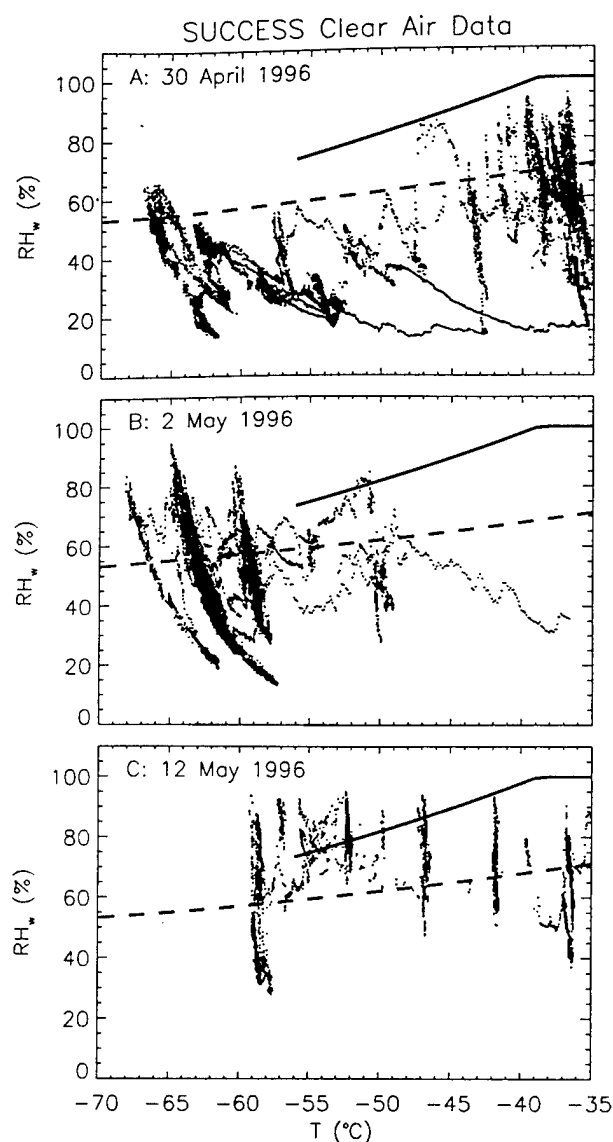


Figure 4. RH derived from DLH water vapor measurements in “clear air” (as determined by the CVI) from three research flights during SUCCESS, shown as a function of temperature. Solid line is RH_{hn} ; dashed line is RH_i .

means an absence of ice crystals detected by a Counterflow Virtual Impactor (CVI) [Twohy et al., 1996] for at least 2 seconds prior to and after an accepted data point. The detection threshold of the CVI varied between 5 and 15 μm diameter depending on the instrument settings, but was usually 5 μm . The accuracy of the RH derived from DLH water vapor measurements and air temperature measurements is estimated to be 6–8%, based on the difference between the derived RH and ice-saturation (RH_i) during penetrations into wave clouds and contrails (where HM calculated that the equilibrium RH in vertical velocities up to several m s^{-1} is within 1–2% of RH_i if the concentration of small ice crystals is several cm^{-3} or greater).

Clear air upwind of orographic wave clouds was sampled on 30 April over eastern New Mexico at temperatures between -35 and -41°C (Fig. 4A). The peak RH values of about 95% were comparable to RH_{hn} , but the

highest RH regions may not have been penetrated since the aircraft was restricted to fly primarily normal rather than parallel to the wind direction, although the data were acquired immediately upwind of the visible cloud edge where the highest RH values would be expected.

The orographic wave environment sampled on the lee side of the Rocky Mountains on 2 May at temperatures between -57 and -65°C (Fig. 4B) showed clear-air RH values approaching water-saturation, seemingly inconsistent with the FIRE-II and balloon-borne measurements. As explored in Section 3, ice nucleation (and RH_{nuc}) likely preceded the peak RH because the vertical velocities are high ($\sim 2.5 \text{ m s}^{-1}$) and ice crystal growth rates at -65°C are very slow (about a factor of 7 slower than at -55°C), implying a relatively rapid increase in RH above RH_{nuc} during the time when newly-nucleated ice crystals grew to detectable sizes.

The off-shore, non-wave environment sampled off the California coast on 12 May (Fig. 4C) provides clear-air data at low temperatures when the vertical velocities were lower than in Fig. 4B (generally $< 1 \text{ m s}^{-1}$), and therefore the degree to which the peak RH exceeds RH_{nuc} should be less severe. The peak RH exceeded 90% and was essentially independent of temperature, much different than the previously-observed consistency with RH_{hn} above -55°C . Measured ice nucleus (IN) and condensation nucleus (CN) concentrations were low on this flight relative to continental measurements on other research days, and the chemical composition of the IN was higher in sulfates than the mineral materials that dominated the continental measurements [P. DeMott, personal communication]. The different characteristics of the IN and CN in this air mass suggest that RH_{nuc} may depend on aerosol properties.

3. Discussion and Implications

The RH data presented in Section 2, with the exception of Fig. 4C, show that $RH_{nuc}(T)$ is generally consistent with HM's $RH_{hn}(T)$ curve at temperatures above -55°C . The high RH values at -60°C and below in Figs. 3A and 4B indicate that RH_{nuc} below -55°C is not an extrapolation of RH_{hn} to colder temperatures. This section will emphasize interpretation of the high RH measurements at cold temperatures, particularly those in Figs. 4B and 4C.

The basis for suggesting that the peak RH in a wave environment at cold temperatures may substantially exceed RH_{nuc} is illustrated in Fig. 5, which shows time series of RH and ice crystal concentration above 5–15 μm diameters for the wave cloud penetration that corresponds to the highest RH values seen in Fig. 4B. The peak RH (labeled “S”) — the point at which vapor depletion from growing ice crystals balances vapor supply from vertical lifting — occurs well before the crystals are detectable by the VIPS, CVI, and a PVM-100. Detection of crystals larger than 2 μm diameter by a Multiangular Aerosol Spectrometer Probe (MASP) confirms that ice nucleation occurred prior to the peak RH, and therefore RH_{nuc} at -65°C must be below 88%.

The average calculated ice crystal growth rate at -65°C for ice crystal diameters between 0.1 and 5 μm is $0.045 \mu\text{m s}^{-1}$ if the RH is 94% (the peak value in Fig. 5), and is $0.03 \mu\text{m s}^{-1}$ at 80% RH and $0.02 \mu\text{m s}^{-1}$ at 70% RH (the RH upwind of the wave). Ice crystals ex-

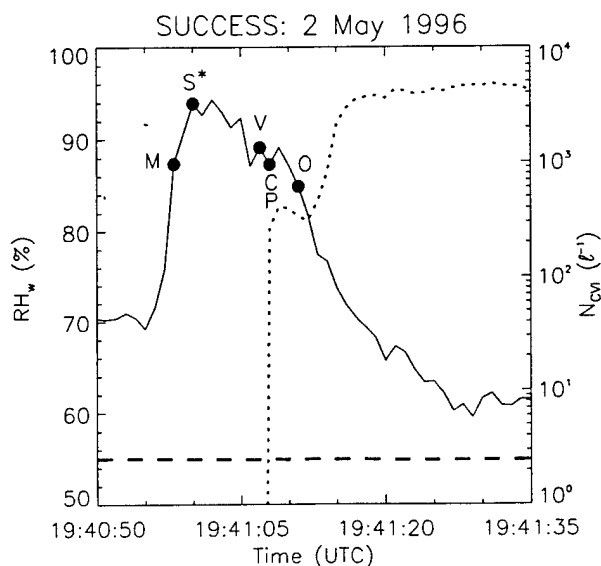


Figure 5. Time series of RH measured by the DLH (solid curve) and ice crystal concentration measured by the CVI (short dashes) for a wave cloud penetration at -65°C . Relative to the peak RH ("S*"), the first detection of ice crystals is indicated from the VIPS ("V"), the CVI ("C"), the PVM-100 ("P"), and the MASP ("M"). Bold dashed line is RH_i .

isted but were smaller than $5\text{ }\mu\text{m}$ for on the order of 150 s (assuming a constant ice crystal growth rate at about 80% RH). Neglecting vapor depletion, for a vertical velocity of 1.5 m s^{-1} the RH would increase above RH_{nuc} by about 20% in 150 s. Unfortunately, it is impossible to estimate RH_{nuc} from such calculations because the aircraft was not flying along the wind direction during this penetration. At the minimum, it is apparent from Fig. 5 that RH_{nuc} at -65°C lies somewhere between 70% and 88%, and is likely below 88% considering the time required for crystals to grow to $2\text{ }\mu\text{m}$.

The very high RH values observed during the 12 May SUCCESS case (Fig. 4C) are somewhat unexpected because the vertical velocities (and vapor supply rates) were relatively low. This case is also inconsistent with RH_{hn} above -55°C , where ice crystal growth rates are faster and instrument detection threshold limitations should be less problematic. We speculate that RH_{nuc} may be greater in this "maritime" environment than in a continental environment as a result of different aerosol properties, based in part on the lower IN and CN concentrations and different IN chemical composition measured on this flight relative to the 2 May flight. Numerous factors could lead to differing aerosol properties in a maritime air mass, such as fewer sources of aerosols (e.g., surface sources of mineral materials and jet aircraft exhaust), or removal of aerosols via fallout of previously-formed ice crystals, such that ice nucleation from the remaining less-numerous or less-effective aerosols requires higher ice-supersaturations.

4. Summary and Conclusions

The RH measurements presented in this paper and in HM indicate that high ice-supersaturations in the upper troposphere are not uncommon, both in clear air and

in clouds. The FIRE-II and balloon-borne data show that the cirrus ice nucleation condition, $RH_{nuc}(T)$, is consistent with HM's $RH_{hn}(T)$ curve in continental environments down to -55°C , but RH_{hn} should not be extrapolated to lower temperatures. The SUCCESS data indicate that RH_{nuc} below -55°C is between 70 and 88%. RH_{nuc} may also depend on characteristics of the aerosols. Perhaps a minimum of two RH_{nuc} relations are needed — representing continental and maritime air masses — but much more data are needed to assess particularly the maritime relation. Uncertainty in observing RH_{nuc} increases at cold temperatures because ice crystal growth rates are very slow and the RH may rise substantially before ice crystals are detectable by most microphysical instrumentation. A well-conceived experiment in orographic wave clouds, with accurate RH measurements and microphysical instrumentation with a submicron detection threshold, may provide a relatively simple dynamical environment for further study of continental ice nucleation conditions.

Acknowledgments. This study was supported by the following programs: NASA FIRE-III grant L55549D; NASA SUCCESS grant A49760D; Air Force Office of Scientific Research grant F49620-96-C-0024.

References

- Brewer, A.W., Condensation trails. *Weather*, 1, 34-40.
- Heymsfield, A.J., and L.M. Miloshevich, Homogeneous ice nucleation and supercooled liquid water in orographic wave clouds. *J. Atmos. Sci.*, 50, 2335-2353, 1993.
- Heymsfield, A.J., and L.M. Miloshevich, Relative humidity and temperature influences on cirrus formation and evolution: Observations from wave clouds and FIRE-II. *J. Atmos. Sci.*, 52, 4302-4326, 1995.
- McFarquhar, G.M., and A.J. Heymsfield, Microphysical characteristics of three anvils sampled during the Central Equatorial Pacific Experiment. *J. Atmos. Sci.*, 53, 2401-2423, 1996.
- Oltmans, S.J., and D.J. Hofmann, Increase in lower stratospheric water vapour at a mid-latitude Northern Hemisphere site from 1981 to 1994. *Nature*, 374, 146-149, 1995.
- Twohy, C.H., A.J. Schanot, and W.A. Cooper, Measurement of condensed water content in liquid and ice clouds using an airborne counterflow virtual impactor. *J. Atmos. Ocean. Tech.*, 14, 197-202, 1996.
- Vay, S.A., B.E. Anderson, G.W. Sachse, J.E. Collins, J.R. Podolske, C.H. Twohy, B.W. Gandrud, B.L. Gary, K.R. Chan, S.L. Baughcum, and H.A. Wallio, DC-8-based observations of aircraft CO, CH₄, N₂O, and H₂O(g) emission indices during SUCCESS. Submitted to *Geophys. Res. Lett.*, 1997.
- A.J. Heymsfield, L.M. Miloshevich, and C. Twohy, National Center for Atmospheric Research P.O. Box 3000 Boulder, Colorado 80307. (e-mail: heyms1@ncar.ucar.edu)
- G. Sachse, NASA Langley Research Center 5 North Dryden Street Hampton, Virginia 23681.
- S. Oltmans, NOAA Climate Monitoring and Diagnostics Laboratory 325 Broadway Boulder, Colorado 80303.

(Received July 18, 1997; revised November 25, 1997; accepted December 5, 1997.)

**Mid-latitude and tropical cirrus
microphysical properties.**

by

Andrew J. Heymsfield and Greg M. McFarquhar

National Center for Atmospheric Research *

Submit to CIRRUS book, Oxford University Press

Corresponding author: Dr. Andrew J. Heymsfield
NCAR/MMM, P.O. Box 3000, Boulder, CO. 80307-3000
heyms1@ncar.ucar.edu

* The National Center for Atmospheric Research (NCAR) is sponsored by the National Science Foundation.

1. Introduction

Cirrus, a principal cloud type that forms at low temperatures in the upper troposphere, are composed almost always of ice crystals (Heymsfield and Miloshevich 1989) and on average cover about 20% of the earth's surface (Hartmann et al. 1992). The purpose of this article is to characterize the microphysical properties of cirrus clouds. The Glossary of Meteorology (Huschke, 1970) defines cirrus clouds as detached clouds in the form of white, delicate filaments, or white or mostly white patches, that are composed of ice crystals. This cloud type forms primarily in the upper troposphere, above about 8 kilometers (25,000 feet), where temperatures are generally below -30°C . There are a number of types of cirrus clouds, with the most frequent ones occurring in layers or sheets with horizontal dimensions of hundreds or even thousands of kilometers. Because horizontal dimensions are much greater than vertical extent, this particular type of cirrus cloud is called cirrostratus. Cirrus can also form in a patchy or tufted shape, when the ice crystals are large enough to acquire an appreciable *fall velocity* (the rate at which ice crystals fall in the vertical) so that trails of considerable vertical extent may form. These trails curve irregularly or slant, sometimes with a comma-like shape, as a result of changes in the horizontal wind velocity with height and variations in the fall velocity of the ice crystals.

A wispy layered cloud that forms at the top of a cumulonimbus cloud, termed an *anvil* because of its shape, is a cirrus that consists essentially of ice debris which spreads outward from the convective parts of the storm. Anvils do not include the white, dense portions of thunderstorms or the active convective column. Anvils can spread to form large, widespread cloud layers. Tropical cirrus clouds are thought to arise primarily from cumulonimbus clouds. Unlike the thin, wispy cirrus typifying midlatitudes, the high altitudes and extensive lateral and vertical development, which often characterize tropical cirrus impose substantial large-scale radiative effects in the atmosphere and at the surface (Hartmann et al. 1992, Collins et al. 1996).

The cirrus-like low-level ice clouds and ice fogs of the Arctic are not considered cirrus. Neither are altocumulus clouds, which form in distinct layers, often less than 100 meters thick, in the mid-troposphere at about 5 to 8 kilometers. They are identified from the ground as sharply outlined clouds reflecting their tendency to a liquid water composition containing rounded, often bubble-like convective elements. Cirrus often merge with altocumulus clouds, producing a deep ice-cloud layer.

In this article, drawing upon microphysical data collected *in-situ* from a variety of sources and in a number of primary cirrus cloud types, the principal microphysical properties of cirrus will be described. The description will include crystal shapes, bulk properties such as ice water content, and general characteristics such as profiles of properties in the vertical.

2. Overview of Principal In-situ Measurements

Figure 1 illustrates locations where *in-situ* microphysical data were collected during field campaigns by a wide variety of investigators using a variety of instruments. The earliest measurements are those of Weickmann (1947), who characterized the shapes of cirrus crystals

above Germany. There have been many other mid-latitude campaigns, including measurements of cirrus and cirrostratus made during the First International Satellite Cloud and Climatology Project (ISCCP) Regional Experiments (FIRE I and FIRE II) over Wisconsin and Kansas (e.g., Heymsfield et al. 1990, Heymsfield and Miloshevich 1995, Arnott et al. 1994), the Environmental Definition Program (EDP) over the continental United States (Heymsfield 1977), the Subsonic Aircraft: Contrail and Cloud Effects Special Study (SUCCESS), and flights over the continental United States between 1979 and 1984 described by Jeck (1988). Mid-latitude measurements made in Europe include those from the European Cloud and Radiation Experiment (EUCREX) (Raschke et al. 1998), the International Cirrus Experiment (ICE) and pre-ICE (e.g., Personne et al. 1990, Raschke et al. 1990, Krupp 1992), observations of young cirrus clouds over southern Germany (Strom et al. 1997), and those made by Mazin and co-investigators over a 20 year period in the former Soviet Union (Mazin 1995). Matsuo et al. (1994), Mizuno et al. (1994) and more recently Murakami and Orikasa (private communication, 1998) have also made observations of cirrus clouds over Japan.

Microphysical knowledge of anvil cirrus is less complete than that of cirrus formed *in-situ* because anvils, particularly their upper regions, are not as accessible to aircraft, and where they are accessible, the ice crystals have often been too small or irregular in shape to be accurately counted and sized with optical cloud particle spectrometers. Nevertheless, measurements of anvil cirrus over Montana during the Cooperative Convection Precipitation Experiment (CCOPE) (Heymsfield 1993) and over Oklahoma and Kansas during PRESTORM (Meitin and Cuning 1985) have been made. Bennetts and Ouldrige (1984), BO in Figure 1, have also described aircraft measurements in the anvil of a winter maritime cumulonimbus near England. More recently, the Texas Florida Underpass (TEFLUN) experiments A and B in Texas and Florida collected data in anvil cirrus.

Measurements of tropical cirrus have been even more difficult to make because these clouds often extend to very high altitudes in locations far removed from aircraft landing sites, and again often consist of small and irregular particles. The measurements made in the Tropics include cirrus sampled in the vicinity of Kwajalein, Marshall Islands (Heymsfield 1986a), cirrus sampled during the Global Atlantic Research Program (GARP) Atlantic Tropical Experiment (GATE) (Griffith et al. 1980), measurements near the tops of thunderstorm cirrus in the vicinity of Panama (Knollenberg et al. 1982), cirrus associated with tropical cyclones and related cloud systems off the northern coast of Australia during the Stratospheric-Tropospheric Exchange Project (STEP) (Knollenberg et al. 1993), cirrus and deep convection sampled during the Tropical Ocean Global Atmosphere/Coupled Ocean-Atmosphere Response Experiment (TOGA-COARE, although the data quality is poor), and outflow anvils characterized during the Central Equatorial Pacific Experiment (Heymsfield and McFarquhar 1996).

Measurements made in Arctic cirrus during the Surface Heat Budget of the Arctic Ocean (SHEBA) Experiment and the Beaufort Arctic Storms Experiment (BASE) are also depicted in Figure 1. Although measurements in cirrus not depicted in Figure 1 have been made, Figure 1 does represent most focused field campaigns. The wide diversity in the measured microphysical properties to be described in Section 6 is presumably due to both natural variability and differences in the characteristics of the instrumentation used. Dowling and Radke (1990)

attempted to summarize the microphysical data from a wide number of projects, but found that the data were widely scattered. The cloud-center altitude ranged from 4 to 20 km, cloud thickness from 0.1 to 8 km, crystal number densities from 10^{-4} to 10^4 liter $^{-1}$, condensed water contents from 10^{-4} to 1.2 g m $^{-3}$, and crystal sizes from 1 to 8000 μ m.

3. Instrumentation

The Particle Measuring System's (PMS) two-dimensional imaging probes, the 2D-C "cloud" probe and to a lesser extent the 2D-P "precipitation" probe, have been the cornerstones for measuring microphysical properties of cirrus clouds. The 2D probes collect electronic, two-dimensional images of particles from about 50 μ m (2D-C) to above 4 mm (2D-P), from which size spectra can be readily obtained and ice crystal shape ("habit") information may be inferred. Hereafter, size refers to dimension, which for the 2D-C and 2D-P is usually the maximum particle dimension either parallel or normal to the aircraft flight direction. The measurement principal and the various configurations of probes are described by Knollenberg (1976), Gordon and Marwitz (1984), Joe and List (1987), Korolev et al. (1998), and Baumgardner and Korolev (1997).

These probes have prevailed because they are relatively reliable, data processing is straightforward and quick, and because spectral moments (e.g. effective radius, extinction coefficient, ice water content, radar reflectivity factor) are readily derived. Possible errors or uncertainties in the moments arise from errors inherent in the measurement of the particle size distributions because of uncertainty in the sampling volume at small crystal sizes and high air speeds (Baumgardner and Korolev 1997), a lack of information on ice crystals below the 2D-C size detection threshold, particle habit determination, and errors or variability in the relationships used to convert size distributions to extinction coefficients and mass. In addition, investigators treat sampling volume and particle sizing differently; for example, the National Center for Atmospheric Research (NCAR) processing routines add one and a half slices to each particle (the probe begins to record data only after a particle fully occults at least one photodiode, and there is additional 1/2 slice uncertainty in particle length) to get the particle's size and accounting for the probe's response time (whereas some other processing routines do not), which in turn affects the sample volume. As detection threshold and probe resolution are an inverse function of aircraft true airspeed, the high airspeeds of some research aircraft (e.g., the NASA DC-8 and Learjets) leads to degradation of performance.

Other probes have been used to measure size distributions of ice crystals. The one-dimensional cloud probe (1D-C) is an earlier version of the 2D-C which gives only a one-dimensional picture of crystals because it lacks the fast response electronics of the 2D-C probe. A forward scattering spectrometer probe (FSSP) measures crystals with diameters between 0.4 and 75 μ m, exact limits depending on the model and probe settings, by interpreting forward scattered light from cloud particles as originating from Mie scatterers. An axial scattering spectrometer probe (ASSP) has also been used. From several passes through a line of cumulus congestus, Gardiner and Hallett (1985) showed that ice particle concentrations measured by an FSSP model 100 were 2 to 3 orders of magnitude larger than the "actual" ice concentrations

measured using a formvar replicator and a 2DC probe. This amplification could have resulted from a variety of factors, most importantly the detection of scattered light from ice particles larger than those which the probe was designed to sense. The recently-developed FSSP-300 has a masked-slit aperture and a laser light source with a Gaussian-shaped intensity distribution, designed to provide a well-determined sample volume and to reduce or eliminate counts produced by ice particles outside the sample volume. The probe appears to measure droplets and ice crystals associated with orographic wave clouds well, where particles are at most tens of microns (Heymsfield and Miloshevich 1995), but there are suggestions that it still responds to the larger ice crystals (e.g., Heymsfield and McFarquhar 1996, Gayet et al. 1996).

In addition to electronic probes, impactor type probes can obtain ice crystal size distributions. These probes are especially important for supplementing the optical probes with information about crystal sizes smaller than $50\text{ }\mu\text{m}$ or so. A Video Ice Particle Sampler (VIPS), developed at NCAR, can be used to obtain images of particles larger than about $5\text{ }\mu\text{m}$ (Heymsfield and McFarquhar 1996) by collecting particles in silicone oil on an 8 mm wide film, and then imaging them with video microscopes at two different magnifications. Collection efficiencies derived from Ranz and Wong (1952) are near unity for particle sizes above $5\text{ }\mu\text{m}$ at aircraft speeds of 200 m s^{-1} . An ice particle replicator developed at the Desert Research Institute (Hallett 1976), DRI, can also size particles down to $5\text{ }\mu\text{m}$ by imaging crystals that impact upon a formvar-coated film. The cloudscope, also developed at DRI, is an imaging microscope detecting particles between 5 and up to a few hundred micrometers (Arnott et al. 1996). Others (e.g., Weickmann 1947) have simply exposed coated slides to determine typical particle habits in cirrus.

In recent years, new instruments for measuring cloud microphysical properties have been developed. These include the Cloud Particle Imager (CPI), which casts an image of a particle on a solid-state, one million pixel CCD camera by freezing the motion of the particle using a 20 ns pulsed, high-power laser diode (Lawson and Jensen 1998); a particle imaging nephelometer, which simultaneously records the particle image and measures the scattering phase function of the imaged particle (Lawson et al. 1998); and a multi-angle scattering probe (MASP), which determines the size and concentration of particles 0.3 to $20\text{ }\mu\text{m}$ diameter by measuring the scattered light from individual particles between 30 and 60° in the forward direction and 120 to 150° in the backward direction (Baumgardner et al. 1996). Use of these probes should considerably enhance knowledge about the microphysical properties of cirrus clouds.

Balloon-borne instruments have also been used to obtain *in-situ* microphysical measurements. For example, Miloshevich and Heymsfield (1997) describe how balloon-borne Formvar ice crystal replicators were used to measure vertical profiles of ice crystal size distributions and detailed ice crystal shapes down to sizes of $10\text{ }\mu\text{m}$. Orikasa and Murakami (1997) have also devised an improved hydrometeor videosonde (HYVIS) which measures vertical distributions of hydrometeors by transmitting particle images, between $7\text{ }\mu\text{m}$ and 5 mm size, obtained by small video cameras by 1.6 GHz microwaves to a ground station.

There are probes that provide a direct measure of the total water content of a cloud without integrating the size distribution. The Nevzarov total water content probe is a hot-

wire type probe, kept at a constant temperature, that evaporates captured crystals. Its shape is designed to allow the capture of droplets and ice crystals. The detection threshold is as low as 0.003 g m^{-3} , and the accuracy of the water content is 10 to 20% when the collection efficiency is known (Mazin 1995). Brown and Francis (1995) have also measured the mass content of cirrus using a total water content (TWC) probe, which evaporates all liquid- or solid-phase water by a heater system and then measures the humidity of the resulting air by a Lyman- α absorption hygrometer; the mass content is obtained by subtracting water vapor obtained from a fast-response Lyman- α fluorescence water vapor sensor. A counterflow virtual impactor (CVI) provides a measure of total water content in the cloud using a Lyman-alpha hygrometer after cloud particles are separated from water vapor and heated within an inlet (e.g., Strom and Heintzenberg, 1994, Twohy et al. 1997). The CVI can also measure crystal number concentration when the size distribution is composed primarily of small ($<50 \text{ }\mu\text{m}$) crystals. The PVM also (Gerber et al. 1994) measures the IWC and surface area of ice crystals directly by using spatial filtering of forward scattering light weighted by the second and third moment of the particle distribution.

4. Cirrus Particle Shapes

Weickmann (1947) first characterized the shapes of cirrus crystals from data collected in a variety of cirrus cloud types. The following relationships between crystal shape, relative humidity, and cloud types were noted in the temperature range -30 to -60°C : for cirrus castellatus, cirrocumulus, cirrus uncinus generating cells, where he inferred that the conditions were close to water saturation, the crystals had prismatic skeleton shapes, occurring in hollow and cluster crystals, called "bullet rosettes" (Fig. 2) or side planes. In cirrus filus and cirrus densus, where crystals grow somewhere between ice and water saturation, Weickmann found the crystals to be prisms (Fig. 2), with air enclosures but not of the typical skeleton shape. In cirrostratus, where relative humidities are somewhere near ice saturation, he found the crystals to be primarily individual and full crystals such as prisms and plates. Heymsfield and Platt (1984) described the crystal shapes in mid-latitude cirrus for three temperature ranges: above -40°C from -40 to -50°C , and below -50°C , subdividing the results according to whether there were cirrus generating cells ("convective" cirrus) or were formed by slow uplift ("stable" clouds). For all situations, hollow columns and hexagonal plates predominated near cloud top, spatial crystals, for example bullet rosettes, were the predominant forms above -40°C , and hollow or solid columns prevailed below -50°C . In the intermediate temperature range -40 to -50°C , convective cirrus contained predominantly spatial crystal forms while stable cirrus contained predominantly hollow columns. More recent studies (e.g., Heymsfield et al. 1990, Kinne et al. 1992, Arnott et al. 1994) have reported on particular aspects of cirrus crystal shapes, including the occurrence of unexpected crystal forms and the habits in specific temperature and relative humidity conditions.

The shapes of ice crystals are poorly known for the Tropics. Some examples of simple columnar and trigonally-shaped ice crystals tens of microns in size, at about -83°C in cirrus at the base of the tropopause have been observed (Heymsfield 1986a). Additionally, Heymsfield and McFarquhar (1996) found lots of examples of highly irregular large crystals in blow-off

anvils associated with deep convection. Crystals smaller than $100\text{ }\mu\text{m}$ measured by the VIPS during CEPEX tended to have a quasi-spherical shape (Heymsfield and McFarquhar 1996), but Heymsfield (1986a) reported an approximately 50% mixture of trigonal plates and columns in thin tropopause cirrus near Kwajalein, Marshall Islands.

More recently, high resolution images of ice crystals have been obtained in anvils with the CPI during TEFLUN-A and TEFLUN-B. Figure 3 shows examples of crystals imaged by the CPI on 13 August 1998 during TEFLUN-B in an anvil between temperatures of -37 and -50°C . Examples of plates, columns, and aggregates of these pristine crystals are seen. For other anvil penetrations during TEFLUN, rimed particles were also seen, frequently in close proximity to the pristine crystals. Ample examples of small crystals, which tend to have quasi-circular shapes suggesting that they may be frozen droplets, are also seen. The complexity and variety of crystal shapes in anvils, also seen during CCOPE (Heymsfield 1986b), is anticipated given the greater amount of moisture available for deposition and the mixing and turbulence associated with the vertical motions (e.g., Lilly 1988).

For radiative transfer modeling and for determining cirrus formation mechanisms, the vertical structure of cirrus needs to be known. It is problematic to obtain such information with aircraft because their high speeds prohibit vertical sampling at the same horizontal location within cloud; vertical profiles derived from gradual ascents or stacked flight legs may not be true vertical profiles due to a cloud's horizontal inhomogeneities. However, during FIRE I, the NCAR King Air penetrated through cirrus in 11 Lagrangian-type spiral descents on seven days, a flight pattern which allowed the aircraft to drift with the same parts of the clouds while descending, thereby capturing the essence of the vertical variation. Cloud top temperatures spanned the range -40 to -45°C . The King Air 2D probe had a minimum detectable size of about $20\text{ }\mu\text{m}$ as a result of the aircraft's low true air speed. Kajikawa and Heymsfield (1989) categorized the habits from each of these spiral descents, and the results of their analyses is depicted in Figure 4 and Table 1. Figure 4 shows the fractional contribution of different habits to the extinction coefficient, an important radiative parameter, for different temperature ranges for different dates. Considerable variability between dates can be noted. For example, columns are more frequent for the cirrus sampled on November 1. On October 19, rosettes are more important to the extinction at higher altitudes than at lower altitudes. Table 1 gives the fractional contributions of different shaped crystals to the total number by integrating particle size spectra over the entire descent. Contributions to number for crystals with maximum dimensions greater than and less than $150\text{ }\mu\text{m}$ are depicted separately. Again, there is large variability between the different dates, and also between the typical shapes of the large and small crystals. Vertical profiles can also be obtained from replicator launches.

5. Overview: Measurements of IWC

Over the past several years increasing attention has focused on the contributions of small particles to cirrus ice water contents. To place the size distribution measurements, which generally begin at 25 to $50\text{ }\mu\text{m}$, into perspective, the contributions and importance of the small crystals will be estimated. Even though the CVI and PVM both measure IWC

directly, they respond to different sizes of ice crystals. Because the CVI measures IWC from all sizes of crystals, whereas the PVM is only sensitive to crystals smaller than about $50\text{ }\mu\text{m}$, a comparison of their IWCs provides information about the spectral distribution of mass. The two probes were used on the NASA DC-8 during SUCCESS to make measurements of contrail cirrus, natural cirrus, and wave clouds. Figure 5 plots the temperature-dependent fraction of $\text{IWC}_{\text{PVM}}/\text{IWC}_{\text{CVI}}$ versus IWC_{CVI} for coincident measurements. The IWCs are larger at higher temperatures and smaller crystals constitute a lower fraction of the IWC for higher total IWC and for higher temperatures. There are fractionally more small crystals for temperatures less than -50°C . The comparison suggests that the size distribution data, from 2D imaging probes, and the related moments to be presented in subsequent sections for temperatures less than -50°C , should be viewed with caution.

6. Size Distributions

Characteristics of cirrus ice particle size distributions and associated spectral moments have been reported in a number of studies (e.g. Heymsfield and Knollenberg 1972; Heymsfield 1975; Varley 1978; Griffith et al. 1980; Sassen et al. 1989; and Heymsfield et al. 1990). The results have been presented in summary form by Liou (1986), Dowling and Radke (1990), and Jeck (1988). Parameterizations of the size-distributions, useful for modeling studies, have been developed by Welch et al. (1980), Heymsfield and Platt (1984) and Kosarev and Mazin (1989) for mid-latitude cirrus and by McFarquhar and Heymsfield (1997) for tropical cirrus.

Figure 6 shows examples of how the concentration of crystals with maximum dimensions larger than $100\text{ }\mu\text{m}$ vary as a function of temperature for different projects at different locations. Because the 2D probes, which have been used in most of the earlier cirrus studies, begin to size particles somewhere between 25 and $50\text{ }\mu\text{m}$ and determine concentrations reliably above about $100\text{ }\mu\text{m}$, we restrict our discussion here the concentrations above $100\text{ }\mu\text{m}$. Ice crystal concentrations (N) fall in the range 10^{-4} to 10^4 liter^{-1} , but are usually from 0.01 to 0.1 per cubic centimeter. There is a wide scatter in the data, both for an individual project and between projects. Some of these differences may be caused by probe calibration differences (e.g., Gayet et al. 1993) and differences in the manner in which the data are processed. The magnitude of the total concentrations of the size spectra are uncertain because of the inability to *reliably* measure ice crystals with maximum dimensions below about $25\text{ }\mu\text{m}$ (Brown 1989, Dowling and Radke 1990, Wielicki et al. 1990, Heymsfield et al. 1990), especially before the advent of recent instrumentation, and fundamental questions about the 2D probe sampling volume (Baumgardner and Korolev 1997).

There is evidence of high concentrations of ice crystals with length below about $25\text{ }\mu\text{m}$, especially at temperatures below about -45°C (e.g., SUCCESS measurements in Figure 5), or when cirrus form in an ice-free region. Using the DRI replicator during FIRE II, Arnott et al. (1994) found the presence of large numbers of ice crystals smaller than $66\text{ }\mu\text{m}$ below the detection threshold of the 2D-C. Strom et al. (1997) found a diameter of mean mass of only $16\text{ }\mu\text{m}$ and high crystal concentrations averaging 2.5 cm^{-3} in cold (-35 to -60°C) young cirrus clouds over southern Germany. Heymsfield and Miloshevich (1993) measured ice crystal concentrations

in excess of 100 cm^{-3} in orographic lenticular wave clouds at temperatures of -37°C and below. In this situation, the high crystal concentrations could be attributed to the homogeneous freezing of solution drops. Homogeneous nucleation may have also been involved in the production of high ice concentrations in the Strom et al. (1997) study and in some of the other studies.

In the Tropics, during STEP, Knollenberg et al. (1993) found particle mass modes at sizes of 20 to 40 μm and rarely found particles larger than 100 μm in the tops of cirrus associated with a typhoon. Heymsfield and McFarquhar (1996) found that small crystals typically dominated over the contributions of larger crystals for cirrus with temperatures lower than -60°C during CEPEX, and Heymsfield (1986a) reported a similar observation in tropical cirrus at about -80°C . However, there is still debate as to the importance of smaller crystals for both mass budgets and for determining the radiative properties of clouds. For example, McFarquhar and Heymsfield (1997) showed that for the majority of tropical anvils in TOGA COARE and CEPEX, small crystals do not dominate the mass and radiative properties of cirrus. Further, Heymsfield et al. (1998) showed that the upper parts of cirrus, where small crystals dominate, cannot alone account for the high optical depths, ice water contents, and albedos for the most climatologically significant population of tropical cirrus. The predominantly large particles in the lower, warmer parts of the cirrus contain at least an order of magnitude greater mass and are dominant in producing the high observed albedos.

The measured particle size distributions in cirrus mirror the variation of the saturation water vapor density with temperature; at low temperatures, particles are smaller and at higher temperatures particles are larger. A secondary factor is ice crystal fallout; the larger crystals at lower temperatures fall to warmer temperatures, depleting the larger crystals at the lower temperatures while adding to the larger crystals at warmer temperatures. In mid-latitudes, number concentrations have been observed to decrease exponentially or in a power-law form with increasing size, and the exponential slope of the size distribution steepens with decreasing temperature (Heymsfield and Platt 1984) meaning that there are fewer of the larger ice crystals on average at lower temperatures. Figure 7 illustrates how the maximum detected particle dimension varies with temperature for many different projects. For temperatures lower than -40°C , substantially more large crystals have been observed in tropical cirrus (McFarquhar and Heymsfield 1997) and in CCOPE anvils (Heymsfield 1986b) than in mid-latitude cirrus. However, in both the Tropics and mid-latitudes, the largest particles in a given size distribution always increase with increasing temperature: when temperatures exceed -40°C , the largest particles often exceed 1 mm in length, while below about -60° they are at most 10 to 100 μm .

7. Cross Sectional Area/Extinction Coefficient

Cross-sectional area is directly measured by the 2D-C, 2D-P, VIPS, CPI, and many other *in-situ* probes from the two dimensional images of crystals. For typical ice crystal sizes and visible wavelengths, the volume extinction coefficient, σ_{ext} is simply twice the cross-sectional area because then extinction efficiency is approximately 2. Integrating extinction efficiency over cloud depth yields extinction optical depth, an important radiative parameter. Scattering cross-sections also depend critically on cross-sectional area. Thus, this second moment of the size distribution

must be known to adequately characterize a cloud's radiative properties.

Figure 8 shows how extinction coefficient, determined as twice cross-sectional area, varies with temperature for cirrus from a wide variety of field projects. Despite some differences between projects, caused by use of varying instrumentation and samplings of different types of cirrus, there is a clear trend of σ_{ext} increasing towards higher temperatures, and consequently, towards the lower levels of cirrus. This is also seen on a case by case base using Heymsfield and Miloshevich's (1995) vertical replicator profiles, the FIRE I Lagrangian descents, and vertical descents through tropopause tropical cirrus (Heymsfield 1986a).

8. Ice Water Content from Size Distributions

The third moment of the size distribution approximately represents the mass or IWC contained within the cirrus clouds. There are greater uncertainties in the estimate of IWC than that of cross-sectional area with most *in-situ* probes because a direct measurement is not obtained. Typically, particle mass is estimated from the maximum dimension and shape or habit of the particle using known relationships between mass, area and dimension. A habit is assigned to each particle based on its dimensions and shape characteristics, such as area ratio, which is the area of a particle compared to that of a circumscribed circle. In the absence of a direct IWC measurement, of which there have been few, it is problematic to determine the accuracy of the IWC calculation. However, comparison studies between different algorithms and different probes and comparisons with radar suggest that IWC is known within a factor of approximately two (Heymsfield and McFarquhar 1996) for the warmer temperatures with larger errors possible for the lower temperatures where small crystals contribute relatively greater IWC percentages.

A summary of ice content data collected in a variety of cirrus types, locations, and time of year are presented in Figure 9. For reference, liquid water content in stratus clouds is typically in the range 0.1 to 0.3 g m^{-3} , while in altostratus it is less than 0.1 g m^{-3} . The ice content in cirrus generally decreases with decreasing temperature, for reasons cited earlier.

The measurements in continental cirrus formed *in-situ* indicate the expected decrease in IWC with decreasing temperature, from as large as 0.1 g m^{-3} above -40°C to about 10^{-4} g m^{-3} below about -60°C (FIRE I, FIRE II, and EDP). The two data sets differ at the higher temperatures because the cirrus in the deeper case, EDP, merged into middle and lower-level clouds while in the shallower case, FIRE, cirrus base and top were well-defined. The EDP data represent averages over about 20 km horizontal distance while the FIRE data span a distance of about 0.5 km.

A study of the water contents of Russian continental clouds of various types during the period 1977–1984 was conducted by Mazin (1995) using data from Nevzarov total water content probe. If it is assumed that all water below -20°C is in the form of ice, distributions of ice water content with temperature can be obtained (see discussion of instrument uncertainties in Section 3). These data are also included in the Figure 9. Differences between the other IWC measurements may be somewhat attributed to the different instruments used to make the measurements.

As a result of the high vertical velocities in convective clouds over the High Plains, the largest ice contents are noted in anvils associated with the High Plains storms (CCOPE). The anvils in the tropics which are known to be associated with weaker updrafts have intermediate ice contents. For penetrations near deep convection in the Tropics, examples of large IWCs have also been noted such as those between -60 and -70°C during CEPEX. Additional measurements in the Tropics, not depicted in Figure 9, have been made. Griffith et al. (1980) found that the ice water content (IWC) estimated from the particle size spectra above about $20\text{ }\mu\text{m}$ ranged from a few hundredths to a few tenths of a g m^{-3} in cirrus sampled between -30 and -60°C during GATE. Knollenberg et al. (1982) measured IWC from particles larger than $40\text{ }\mu\text{m}$ of a few thousandths to a few hundredths of a g m^{-3} at about -70°C near the tops of thunderstorm cirrus in the vicinity of Panama. Using a dual size-range spectrometer, Knollenberg et al. measured IWCs as high as 0.07 g m^{-3} in the tops of cirrus (13 to 18 km , -60 to -90°C) associated with tropical cyclones and related cloud systems off the northern coast of Australia during STEP. These measurements must be viewed with caution as most of the particles were smaller than $30\text{ }\mu\text{m}$, where spectrometers are known to be unreliable. From cirrus sampled in the vicinity of Kwajalein, Marshall Islands, Heymsfield (1993) found a general decrease in IWC with decreasing temperature, with mean values ranging from about 0.2 g m^{-3} at -5°C to 0.0001 g m^{-3} at -85°C .

9. Three Layer Cirrus Conceptual Model

Vertical profiles of microphysical data from aircraft Lagrangian spiral descents during FIRE I and balloon-borne ice crystal replicator launches from FIRE II indicate that average ice crystal sizes increase from cloud top downwards to near cloud base, where they decrease abruptly to produce cloud base. These observations suggest a conceptual view of the formation and development of cirrus clouds. In-situ generated cirrus clouds can be represented by three distinct layers in the vertical: the *nucleation layer* (Layer 1), is the uppermost part of the cloud, composed of small ice crystals, where the relative humidity, RH, exceeds the relative humidity required for ice initiation, and ice production occurs; the *growth layer* (Layer 2), is a thicker layer, composed of pristine ice crystal shapes, where ice-supersaturation sustains crystal growth; and the *sublimation layer* (Layer 3) is a thinner layer, composed of rounded crystals of indistinct shape, where ice-subsaturation causes crystals to sublimate and eventually disappear. There can be variations in the number of layers; for example, cirrus that is initially developing contains no sublimation layer and cirrus that is decaying will have no nucleation layer.

According to this model, nucleation occurs in Layer 1, and may be either discrete or continuous, depending on the vertical velocities and temperature. Layer 2 is a deeper region of ice supersaturation, where ice crystals can grow from tens of microns to hundreds and even a thousand microns. Layer 3 is the sublimation zone, where ice crystals generated aloft fall into dry air, lowering the cloud base and moistening the air below. The thickness of Layer 3 is dependent upon the IWC and particle sizes near the base of Layer 2 and the RH and temperature profiles in Layer 3.

This conceptual model is consistent with earlier observations of ice development in cirrus convective elements or "generating cells". Ludlam (1980) postulated that ascent in the updrafts

of generating cells may lead to ice particles produced by heterogeneous nucleation a little below water-saturation, which represents an ice-supersaturated region several hundred meters deep above the level of ice-saturation. Sassen et al. (1990) noted from lidar observations that cirrus frequently developed in the vertical from particle fallstreaks emanating from generating regions at or near cloud top. Mace et al. (1996) showed that the radar reflectivity factor in wintertime cirrus, roughly proportional to the square of the ice-water content, tends to increase between cloud top and the middle regions of the cloud and then decreases in the lower third of the layer. This is consistent with the trends seen from replicator launches during FIRE II, namely crystal growth occurring in the upper two thirds of moist cirrus layers while the lower third is dominated by sublimation.

10. Summary and Future Problems

In this article, cirrus cloud microphysical data acquired in mid-latitude and tropical locations by many researchers have been summarized, and the principal instruments and measurement techniques used by them to collect the data have been described. Some of the principal findings are outlined below.

- Ice particle shapes vary considerably from one cloud to another. Polycrystals, especially bullet rosettes, are the predominant ice particle form in mid-latitude, in-situ generated cirrus, although columns and single bullets are found frequently. There is some suggestion that columns predominate with cloud top temperatures below -55 or -60°C . Near cloud base, crystal edges round in response to sublimation. Particles in anvils can be aggregated and rimed and shapes can be more complex.
- Cirrus cloud properties, for example, concentration, extinction coefficient, and ice water content, can be highly variable from one cloud to another and within a single cloud. However, there does appear to be a tendency for the mean and maximum crystal size, extinction coefficient and ice water content to increase with temperature.
- Ice crystals below $100\mu\text{m}$ dominate the number concentration, especially near cloud top where the predominant ice particle nucleation occurs. Ice particle size tends to increase downward to near cloud base. The lowermost parts of cirrus tend to be sublimation regions.
- While small ice crystals dominate extinction near cloud top, larger particles in the mid and lower-cloud levels are responsible for most of the cloud optical depth on average. Similar findings are noted for ice water content.
- Parameterizations of the size spectra in terms of the ice water content and temperature have been developed. They are broad averages and cannot represent the variability from one cloud to another.
- Most of the cirrus cloud microphysical data have been acquired with Particle Measuring Systems 2D imaging probes. The concentrations below $100\mu\text{m}$, and the derived microphysical properties from these probes, have been significantly underestimated for temperatures below -55°C . Probes have been developed in recent years to provide habit and concentration information in the smaller sizes.

Future studies of cirrus clouds should focus on the upper parts of tropical and mid-latitude anvils, which are very important for the earth's heat and radiation budget but have been inadequately studied. Studies at high altitudes may require a new generation of cloud physics aircraft with higher altitude sampling capabilities. Impacts of jet aircraft on cirrus cloud coverage and microphysical properties also need to be better defined. While remote sensing techniques for retrieving cirrus cloud properties offer great promise for building global cirrus cloud climatologies, more intercomparisons are needed to evaluate the performance of these techniques. Laboratory studies are needed to determine the ice crystal nucleation rates, the conditions (temperature, relative humidity) when homogeneous versus heterogeneous ice nucleation dominate, and the dependence of ice crystal growth rates and shapes on supersaturation. Modeling studies can yield insight into the conditions when heterogeneous versus homogeneous ice nucleation predominate, as well as concentrations and size spectra in the vertical and horizontal.

11. Acknowledgments

The authors wish to thank Steve Aulenbach, Lesley Smith, and Won-Seok Ryu for their assistance in preparing the manuscript and figures. Several individuals have helped by allowing their data to be included in our investigation, including Larry Miloshevich and Cynthia Twohy from NCAR, Phil Brown and Peter Francis from the U.K. Meteorological Office, Richard Jeck from the Naval Research Laboratory, Ilia Mazin formerly from the Central Aerological Observatory, Pat Arnott and John Hallett from the Desert Research Institute, Hermann Gerber of Gerber Scientific, Paul Lawson of SPEC Inc., and Mike Poellot of the University of North Dakota. The assistance of funding from the Air Force, AFOSR grant number F49620-96-C-0024, is acknowledged.

12. References

- Arnott, W.P., Y. Dong, J. Hallett, and M.R. Poellot, 1994: Role of small ice crystals in radiative properties of cirrus: a case study, FIRE II, November 22, 1991. *J. Geophys. Res.*, **99**, 1371–1381.
- Arnott, W.P., Y. Dong, R. Purcell, and J. Hallett, 1996: Direct airborne sampling of small ice crystals and the concentration and phase of haze particles. *9th Symp Met. Observ. Instr.*
- Baumgardner, D., and A. Korolev 1997: Airspeed corrections for optical array probe sample volumes. *J. Atmos. Ocean. Tech.*, **14**, 1224–1229.
- Baumgardner, D., J.E. Dye, B. Gandrud, K. Barr, K. Kelly, and R.K. Chan, 1996: Refractive indices of aerosols in the upper troposphere and lower stratosphere. *Geophys. Res. Lett.*, **23**, 749–752.
- Bennetts, D.A., and M. Ouldridge, 1984: Observational study of the anvil of a winter maritime cumulonimbus cloud. *Quart. J. Roy. Meteor. Soc.*, **110**, 85–103.

- Brown, P.R.A., 1989: The use of holography for airborne cloud physics measurements. *J. Atmos. Ocean. Tech.*, **6**, 293–306.
- Brown, P.R.A., and P.N. Francis, 1995: Improved measurements of the ice water content in cirrus using a total-water probe. *J. Atmos. Ocean. Tech.*, **12**, 410–414.
- Collins, W.D., F.P.J. Valero, P.J. Flatau, D. Lubin, H. Grassl, and P. Pilewskie, 1996: Radiative effects of convection in the tropical Pacific. *J. Geophys. Res.*, **101**, 14999–15012.
- Dowling, D.R., and L.F. Radke, 1990: A summary of the physical properties of cirrus clouds. *J. Appl. Meteor.*, **29**, 970–978.
- Gardiner, B.A., and J. Hallett, 1985: Degradation of in-cloud forward scattering spectrometer probe measurements in the presence of ice particles. *J. Atmos. Ocean. Tech.*, **2**, 171–180.
- Gayet, J.F., P.R.A. Brown, and F. Albers, 1993: A comparison of in-cloud measurements obtained with six PMS 2D-C probes. *J. Atmos. Ocean. Tech.*, **10**, 180–194.
- Gayet, J.-F., G. Febvre, and H. Larsen, 1996: The reliability of the PMS FSSP in the presence of small ice crystals. *J. Atmos. Ocean. Tech.*, **13**, 1300–1310.
- Gerber, H., B.G. Arends, and A.S. Ackerman, 1994: New microphysics sensor for aircraft use. *Atmos. Res.*, **31**, 235–252.
- Gordon, G.L., and J.D. Marwitz, 1984: An airborne comparison of three PMS probes. *J. Atmos. Ocean. Tech.*, **1**, 22–27.
- Griffith, K.T., S.K. Cox, and R.G. Knollenberg, 1980: Infrared radiative properties of tropical cirrus clouds inferred from aircraft measurements. *J. Atmos. Sci.*, **37**, 1077–1087.
- Hallett, J., 1976: Measurements of size, concentration and structure of atmospheric particulates by the airborne continuous replicator, final report, Cloud particle replicator for use on a pressurized aircraft, 92 pp., I, II, supplementary final report, 151 pp. contract AFGL-TR-76-0149, Air Force Geophys. Lab.
- Hartmann, D.L., M.E. Ockert-Bell, and M.L. Michelsen, 1992: The effect of cloud type on earth's energy balance: Global analysis. *J. Clim.*, **5**, 1281–1304.
- Heymsfield, A.J., 1975: Cirrus uncinus generating cells and the evolution of cirriform clouds. Part I: Aircraft observations of the growth of the ice phase. *J. Atmos. Sci.*, **32**, 799–808.
- Heymsfield, A.J., 1977: Precipitation development in stratiform ice clouds: a microphysical and dynamical study. *J. Atmos. Sci.*, **34**, 367–381.
- Heymsfield, A.J., 1986a: Ice particles observed in a cirriform cloud at -83°C and implications for polar stratospheric clouds. *J. Atmos. Sci.*, **43**, 851–855.
- Heymsfield, A.J., 1986b: Ice particle evolution in the anvil of a severe thunderstorm during CCOPE. *J. Atmos. Sci.*, **43**, 2463–2478.
- Heymsfield, A.J., 1993: Microphysical structures of stratiform and cirrus clouds. *Aerosol-Cloud-Climate Interactions*, P.V. Hobbs, Ed., Academic Press, 97–121.
- Heymsfield, A.J., and R.G. Knollenberg, 1972: Properties of cirrus generating cells. *J. Atmos. Sci.*, **9**, 1358–1366.

- Heymsfield, A.J., and G.M. McFarquhar, 1996: High albedos of cirrus in the tropical Pacific warm pool: microphysical interpretations from CEPEX and from Kwajalein, Marshall Islands. *J. Atmos. Sci.*, **53**, 2424–2451.
- Heymsfield, A.J., and L. Miloshevich, 1989: Evaluation of liquid measuring instruments in cold clouds sampled during FIRE. *J. Atmos. Ocean. Tech.*, **6**, 378–388.
- Heymsfield, A.J., and L. Miloshevich, 1993: Homogeneous ice nucleation and supercooled liquid water in orographic wave clouds. *J. Atmos. Sci.*, **50**, 2335–2353.
- Heymsfield, A.J., and L. Miloshevich, 1995: Relative humidity and temperature influences on cirrus formation and evolution: observations from wave clouds and FIRE II. *J. Atmos. Sci.*, **52**, 4302–4326.
- Heymsfield, A.J., and C.M.R. Platt, 1984: A parameterization of the particle size spectrum of ice clouds in terms of ambient temperature and their ice water content. *J. Atmos. Sci.*, **41**, 846–855.
- Heymsfield, A.J., K.M. Miller, and J.D. Spinhirne, 1990: The 27–28 October 1986 FIRE IFO cirrus case study: cloud microstructure. *Mon. Wea. Rev.*, **118**, 2313–2328.
- Heymsfield, A.J., L.M. Miloshevich, G.M. McFarquhar, J. Goldstein, and S. Oltmans, 1996: A comparison of mid-latitude and tropical cirrus microphysical properties and a conceptual model of cirrus cloud structure. *Proc. 12th Int. Conf. Clouds Precip.*, Zurich, Switzerland, 131–134.
- Heymsfield, A.J., G.M. McFarquhar, W.D. Collins, J.A. Goldstein, F.P.J. Valero, J. Spinhirne, W. Hart, and P. Pilewskie, 1998: Cloud properties leading to highly reflective tropical cirrus: Interpretations from CEPEX, TOGA COARE, and Kwajalein, Marshall Islands. *J. Geophys. Res.*, **103**, 8805–8812.
- Huschke, R.E., 1970: Glossary of Meteorology. *Amer. Meteor. Soc.*, 638 pp.
- Jeck, R.K., 1986: Airborne cloud physics projects from 1974 through 1984. *Bull. Amer. Meteor. Soc.*, **67**, 1473–1477.
- Jeck, R.K., 1988: Federal Aviation Administration report DOT/FAA/CT-89/3.
- Joe, P., and R. List, 1987: Testing and performance of a two-dimensional optical array spectrometer with greyscale. *J. Atmos. Sci.*, **4**, 139–150.
- Kajikawa, M., and A.J. Heymsfield, 1989: Aggregation of ice crystals in cirrus. *J. Atmos. Sci.*, **46**, 3108–3121.
- Kinne, S., T.P. Ackerman, A.J. Heymsfield, F.P.J. Valero, K. Sassen, and J.D. Spinhirne, 1992: Cirrus microphysics and radiative transfer: cloud field study on 28 October 1986. *Mon. Wea. Rev.*, **120**, 661–684.
- Knollenberg, R.G., 1976: Three new instruments for cloud physics measurements: the 2-D spectrometer, the forward scattering spectrometer probe and the active scattering aerosol spectrometer. *Proc. Int. Conf. Cloud Phys.*, Boulder, CO
- Knollenberg, R.G., A.J. Dascher, and D. Huffman, 1982: Measurements of the aerosol and ice crystal populations in tropical stratospheric cumulonimbus anvils. *Geophys. Res. Lett.*, **9**, 613–616.
- Knollenberg, R.G., K. Kelly, and J.C. Wilson, 1993: Measurements of high number densities of ice crystals in the tops of tropical cumulonimbus. *J. Geophys. Res.*, **98**, 8639–8664.

- Korolev, A.V., J.W. Strapp, and G.A. Isaac, 1998: Evaluation of the accuracy of PMS optical array probes. *J. Atmos. Ocean. Tech.*, **15**, 708-720.
- Kosarev, A.L., and I.P. Mazin, 1989: Empirical model of physical structure of the upper level clouds of the middle latitudes. *Radiation Properties of Cirrus Clouds*, Nauka, 29-52.
- Krupp, C., 1992: Holographische Messungen an Eiskristallen in Cirruswolkn wahrend des Internationalen Cirrus Experiments ICE. GKSS 92/E/14, 145 pp.
- Lawson, R.P., and T.L. Jensen, 1998: Improved microphysical observations in mixed phase clouds. *Conf. Cloud Phys.*, Amer. Meteor. Soc., Everett, WA, 451-454.
- Lawson, R.P., A.J. Heymsfield, S.M. Aulenbach, and T.L. Jensen, 1998: Shapes, sizes and light scattering properties of ice crystals in cirrus and a persistent contrail during SUCCESS. *Geophys. Res. Lett.*, **25**, 1331-1334.
- Lilly, D.K., 1988: Cirrus outflow dynamics. *J. Atmos. Sci.*, **45**, 1594-1605.
- Liou, K.N., 1986: Influence of cirrus clouds on weather and climate processes: a global perspective. *Mon. Wea. Rev.*, **114**, 1167-1199.
- Ludlam, F. H., 1980: Clouds and Storms. The Behavior and Effect of Water in the Atmosphere. *The Pennsylvania State University Press*, 407 pp.
- Mace, G.G., T.P. Ackerman, E.E. Clothiaux, B.A. Albrecht, 1997: A study of composite cirrus morphology using data from a 94-GHz radar and correlations with temperature and large-scale vertical motion. *J. Geophys. Res.*, **102**, 13581-13593.
- Matsuo, T., H. Mizuno, M. Murakami, and Y. Yamada, 1994: Ice crystal formation in cirrus cloud. *Nucleation and atmospheric aerosols*, Fukuta, Norihikok, and Wagner, Eds., Deepak Publishing, 283-286.
- Mazin, I. P., 1995: Cloud water content in continental clouds of middle latitudes. *Atmos. Res.*, **35**, 283-297.
- McFarquhar, G.M., and A.J. Heymsfield, 1997: Parameterization of tropical cirrus ice crystal size distributions and implications for radiative transfer: results from CEPEX. *J. Atmos. Sci.*, **54**, 2187-2200.
- Meitin, J.G. Jr. and J.B. Cunning, 1985: Oklahoma-Kansas preliminary regional experiment for storm-central (O-K PRESTORM), VOL. 1, Daily operations summary. National Oceanic and Atmospheric Administration Technical Memorandum (NOAA TM ERL ESG-20), 313 pp.
- Miloshevich, L.M., and A.J. Heymsfield, 1997: A balloon-borne continuous cloud particle replicator for measuring vertical profiles of cloud microphysical properties: Instrument design, performance, and collection efficiency analysis. *J. Atmos. Ocean. Tech.*, **14**, 753-768.
- Mizuno, H., T. Matsuo, M. Murakami, and Y. Yamada, 1994: Microstructure of cirrus clouds observed by HYVIS. *Atmos. Res.*, **32**, 115-124.
- Orikasa, N., and M. Murakami, 1997: A new version of hydrometeor videosonde for cirrus cloud observations. *J. Meteor. Soc. Japan*, **75**, 1033-1039.
- Personne, P., C. Duroure, C. Isaka, and H. Isaka, 1991: Geometrical characteristics of cirrus ice crystals. *IAMAP Program and Abstracts*, Villeneuve D'Ascq, France, 3 pp.

- Ranz, W.E., and J.B. Wong, 1952: Impaction of dust and smoke particles. *Ind. Eng. Chem.*, **44**, 1371-1381.
- Raschke, H., J. Schmetz, J. Heintzenberg, R. Kandel, and R. Saunders, 1990: International Cirrus Experiment. *ESA Bull.*, **14**, 113-119.
- Raschke, E., P. Flamant, Y. Fouquart, P. Hignett, H. Isaka, P.R. Jonas, H. Sundquist, and P. Wendling, 1998: Cloud-radiation studies during the European cloud and radiation experiment (EUCREX). *Surveys Geophys.*, **19**, 89-138.
- Sassen, K., D.O'C. Starr, and T. Uttal, 1989: Mesoscale and microscale structure of cirrus clouds: three case studies. *J. Atmos. Sci.*, **46**, 371-396.
- Sassen, K., C.J. Grund, J.D. Spinhirne, M.M. Hardesty, and J.M. Alvarez, 1990: The 27-28 October 1986 FIRE IFO cirrus case study: a five lidar overview of cloud structure and evolution. *Mon. Wea. Rev.*, **118**, 2288-2311.
- Strom, J. and J. Heintzenberg, 1994: Water vapor, condensed water, and crystal concentration in orographically influenced cirrus clouds. *J. Atmos. Sci.*, **51**, 2368-2383.
- Strom, J., B. Strauss, T. Anderson, F. Schroder, J. Heintzenberg, and P. Wendling, 1997: In situ observations of the microphysical properties of young cirrus clouds. *J. Atmos. Sci.*, **54**, 2542-2553.
- Twohy, C.H., A.J. Schanot, and W.A. Cooper, 1997: Measurement of condensed water content in liquid and ice clouds using an airborne counterflow virtual impactor. *J. Atmos. Ocean. Tech.*, **14**, 197-202.
- Varley, D.J., 1978: Cirrus particle distribution study, Part I. Tech Rep. AFGL-TR-78-0192, Air Force Geophysical Laboratory, Hanscom Air Force Base, MA, 71 pp.
- Weickmann, H., 1947: *Die Eisphase in der Atmosphere.*, Royal Aircraft Establishment, 96 pp.
- Welch, R.M., S.K. Cox, and J.M. Davis, 1980: *Solar Radiation and Clouds. Meteor. Monogr.*, No. 39, Amer. Meteor. Soc., 93 pp.
- Wielicki, B.A., J.T. Suttles, A.J. Heymsfield, R.M. Welch, J.D. Spinhirne, M.-L. C. Wu, D. O'C. Starr, L. Parker, and R.F. Arduini, 1990: The 27-28 October 1986 FIRE IFO cirrus case study: Comparison of radiative transfer theory with observations by satellite and aircraft. *Mon. Wea. Rev.*, **118**, 2356-2376.

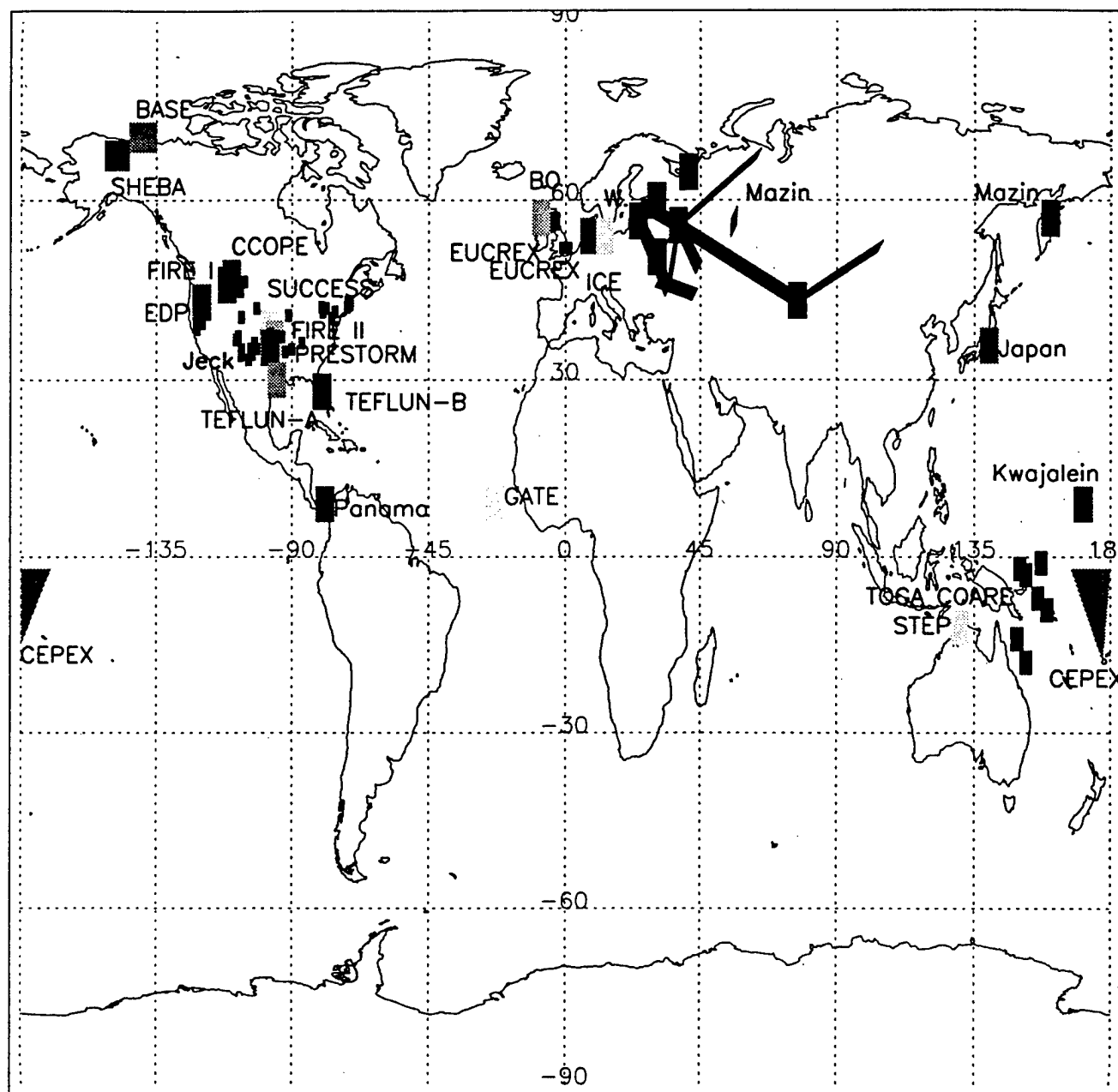
TABLE CAPTIONS

Figure 1: Percentage of different habits observed during Lagrangian-style descents during FIRE
1. Habits obtained by integrating over entire descent, using habits identified by Kajikawa and Heymsfield (1989). Contributions for large and small crystals depicted separately.

FIGURE CAPTIONS

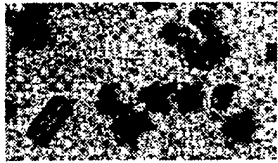
- Figure 1: Locations where *in-situ* microphysical measurements of cirrus have been made. Acronyms of projects defined in text, labels listed in approximate chronological order. Measurements not identified by project name listed by location (e.g., Japan, Kwajalein), or principal investigator (e.g., Jeck, Mazin).
- Figure 2: Examples of crystals collected by Weickmann (1947) in variety of cirrus.
- Figure 3: Crystal images recorded by CPI on 13 August 1998 during TEFLUN-B in anvil at temperatures between -37 and -50°C.
- Figure 4: Percentage of different habit crystals, identified by Kajikawa and Heymsfield (1989), contributing to extinction coefficient obtained during 4 Lagrangian-type spiral descents through cirrus during FIRE 1.
- Figure 5: Fraction of IWC measured by PVM to IWC measured by CVI against IWC measured by CVI for all coincident measurements during SUCCESS in 1996, plotted for different temperature ranges.
- Figure 6: Concentration of crystals with maximum dimension greater than 100 μm as function of temperature for different projects. Acronyms described in text. Symbol represent median values, horizontal bars span quartiles of the distributions. Data obtained from optical array probes.
- Figure 7: Maximum detected particle dimension as function of temperature. Symbols and horizontal bars represent median value and quartiles of distributions. Data obtained from optical array probes and replicators.
- Figure 8: Volume extinction coefficient as function of temperature. Symbols and horizontal bars represent median value and quartiles of distributions. See text for details.
- Figure 9: IWC as function of temperature for different projects. Symbols and horizontal bars represent median value and quartiles of distributions. See text for details.

Heymsfield and McFarquhar, Fig. 1, top

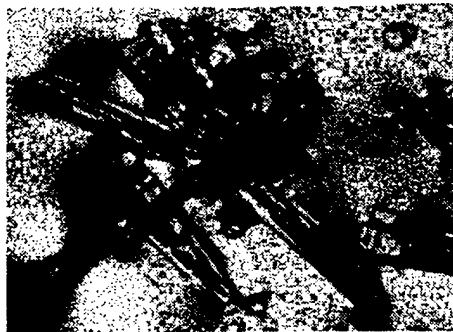


Weickmann	Kwajalein	EDP	GATE	Mazin	Jeck
BO	Panama	CCOPE	PRESTORM	FIRE I	ICE
Japan	STEP	FIRE II	TOGA COARE	EUCREX	CEPEX
BASE	SUCCESS	SHEBA	TEFLUN-A	TEFLUN-B	

CIRROCUMULUS



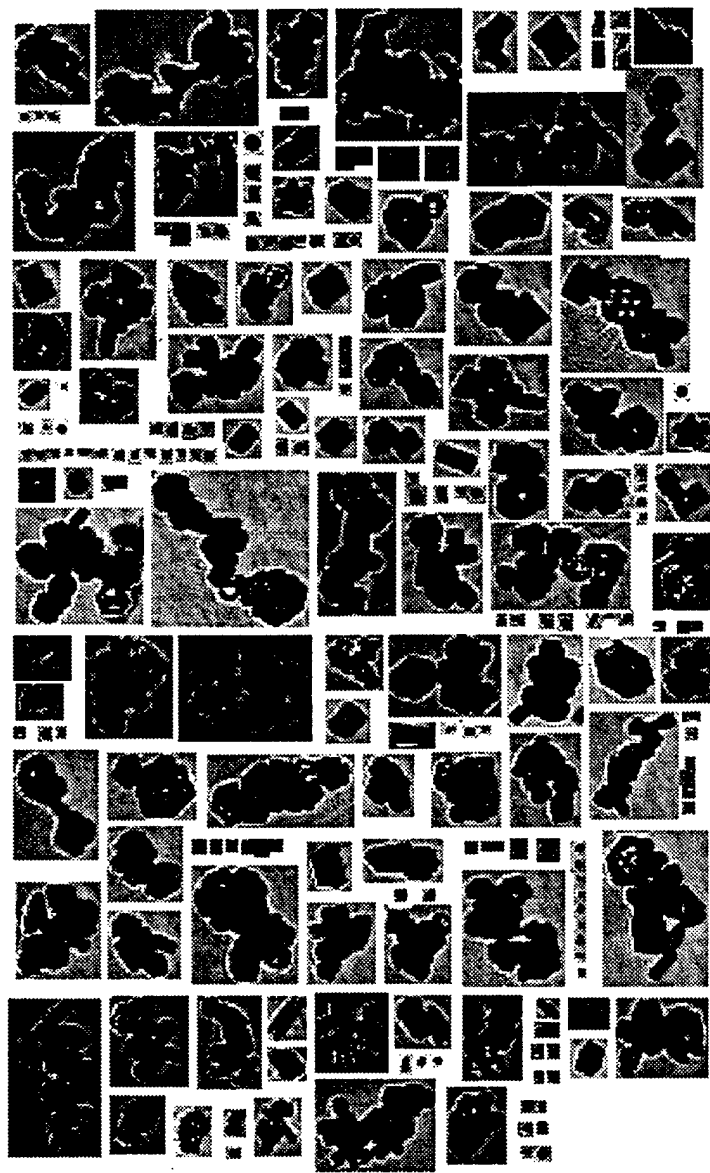
CONVECTIVE CIRRUS

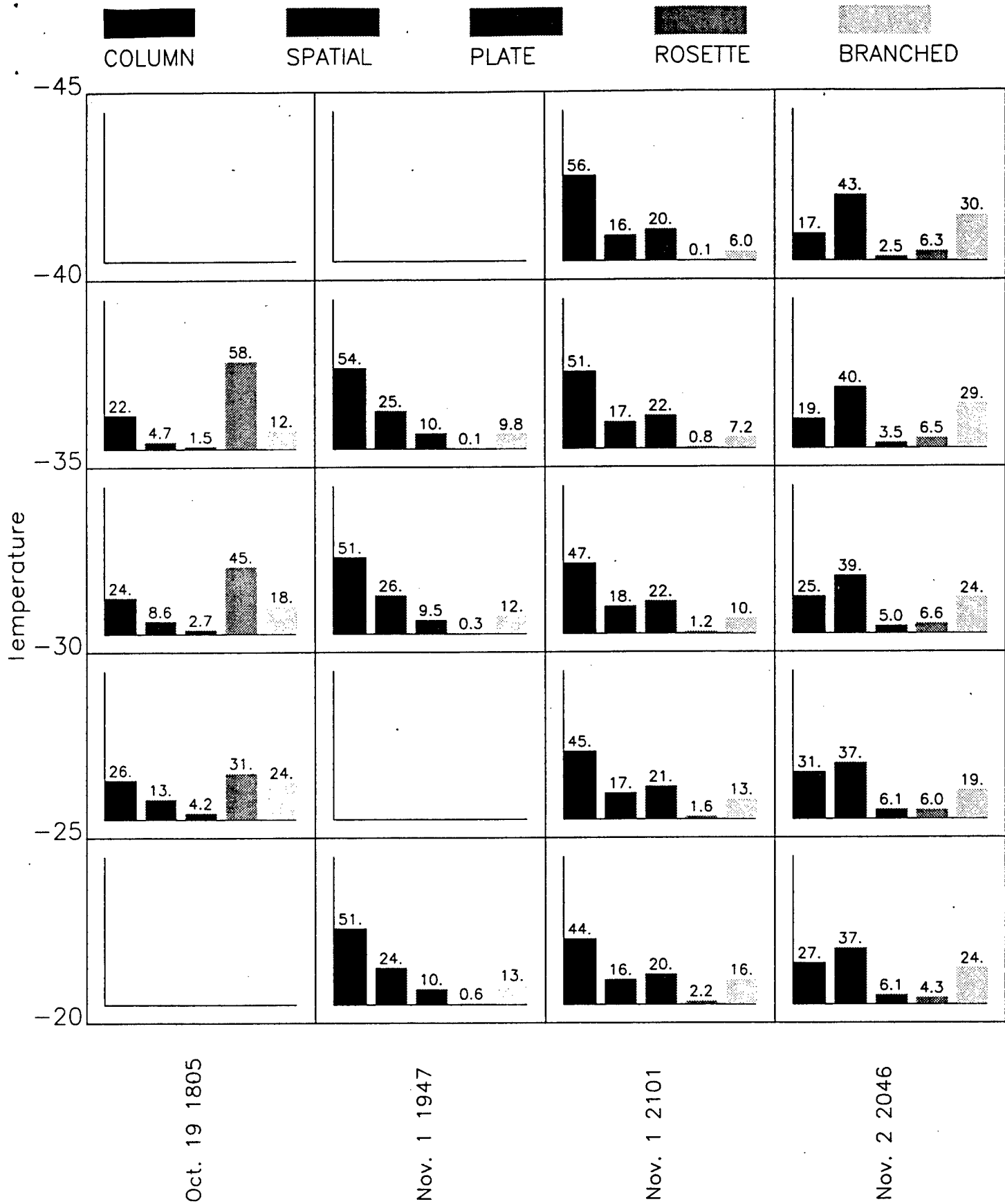


CIRRUS DENSUS



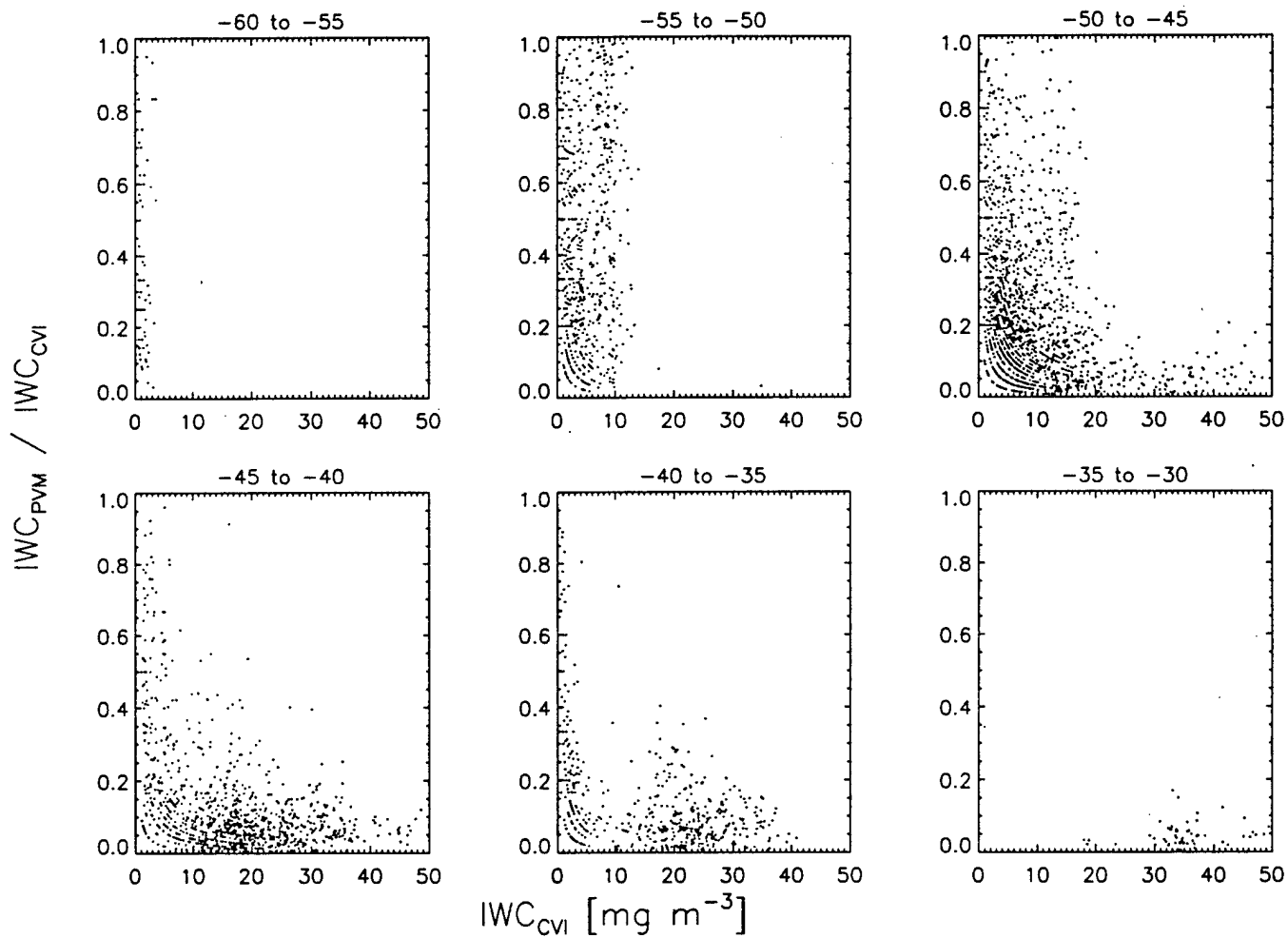
Heymsfield and McFarquhar, Fig. 3, top

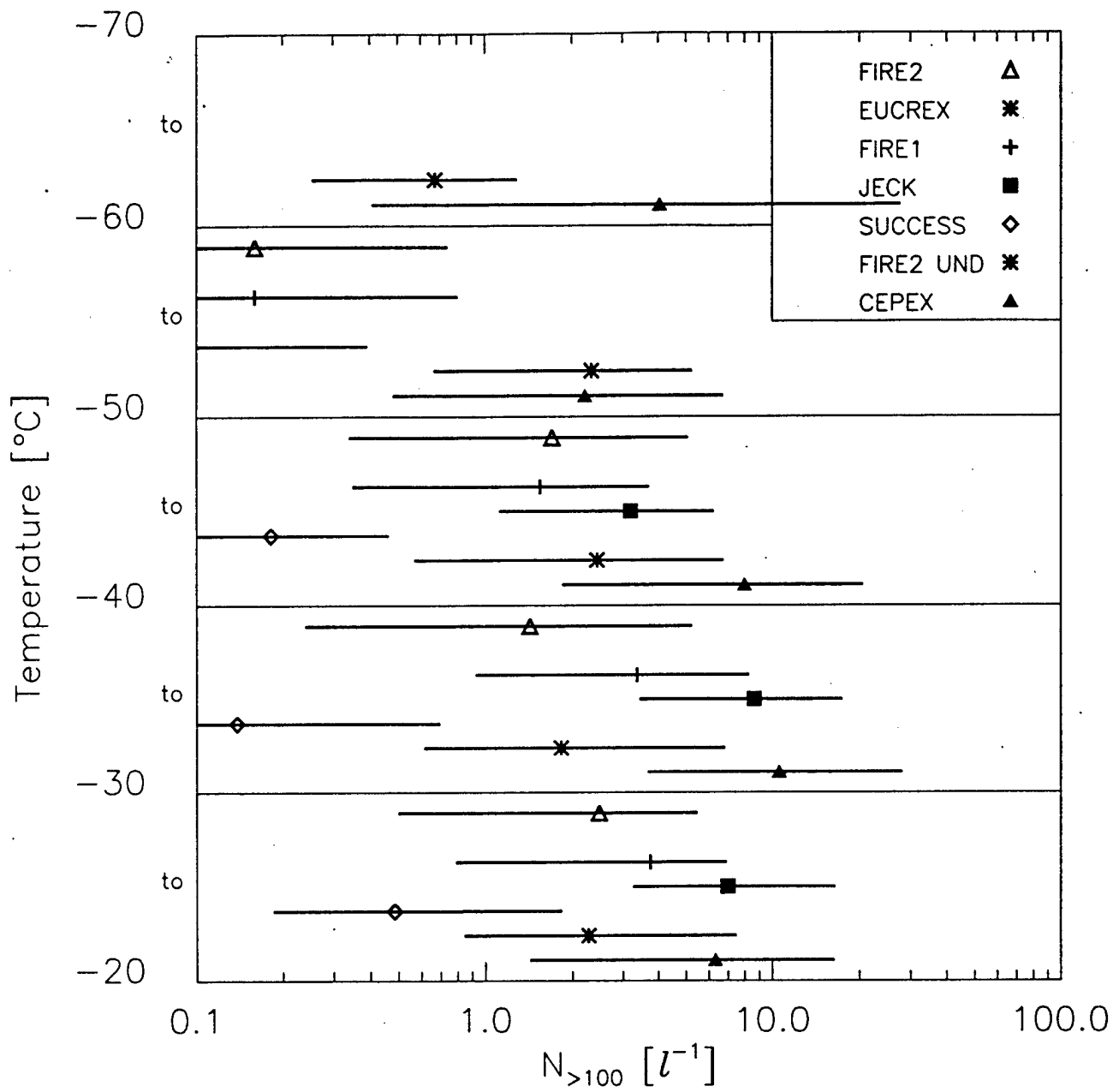




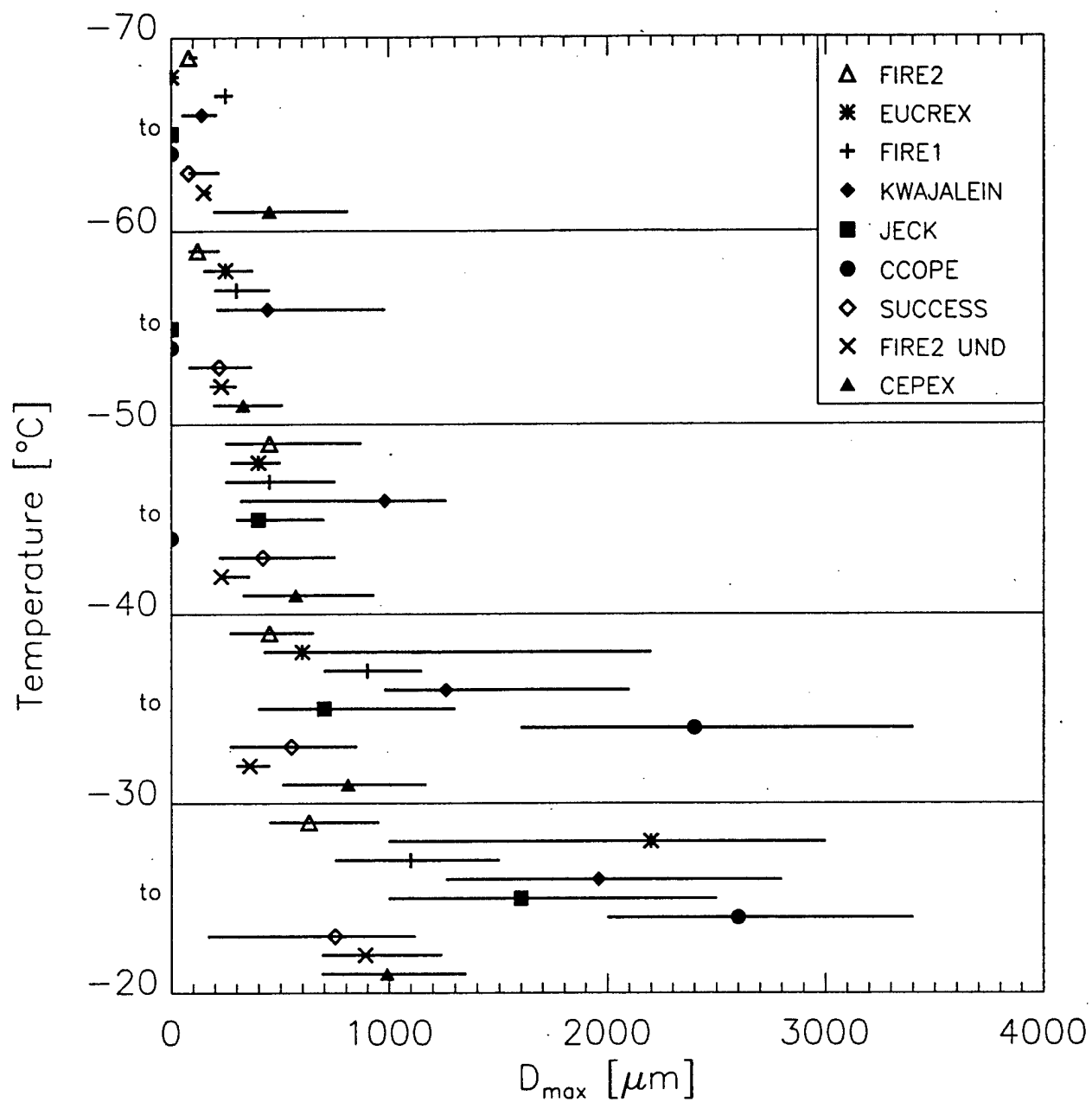
Heymsfield and McFarquhar, Fig. 4, bottom

Heymsfield and McFarquhar, Fig. 5, top

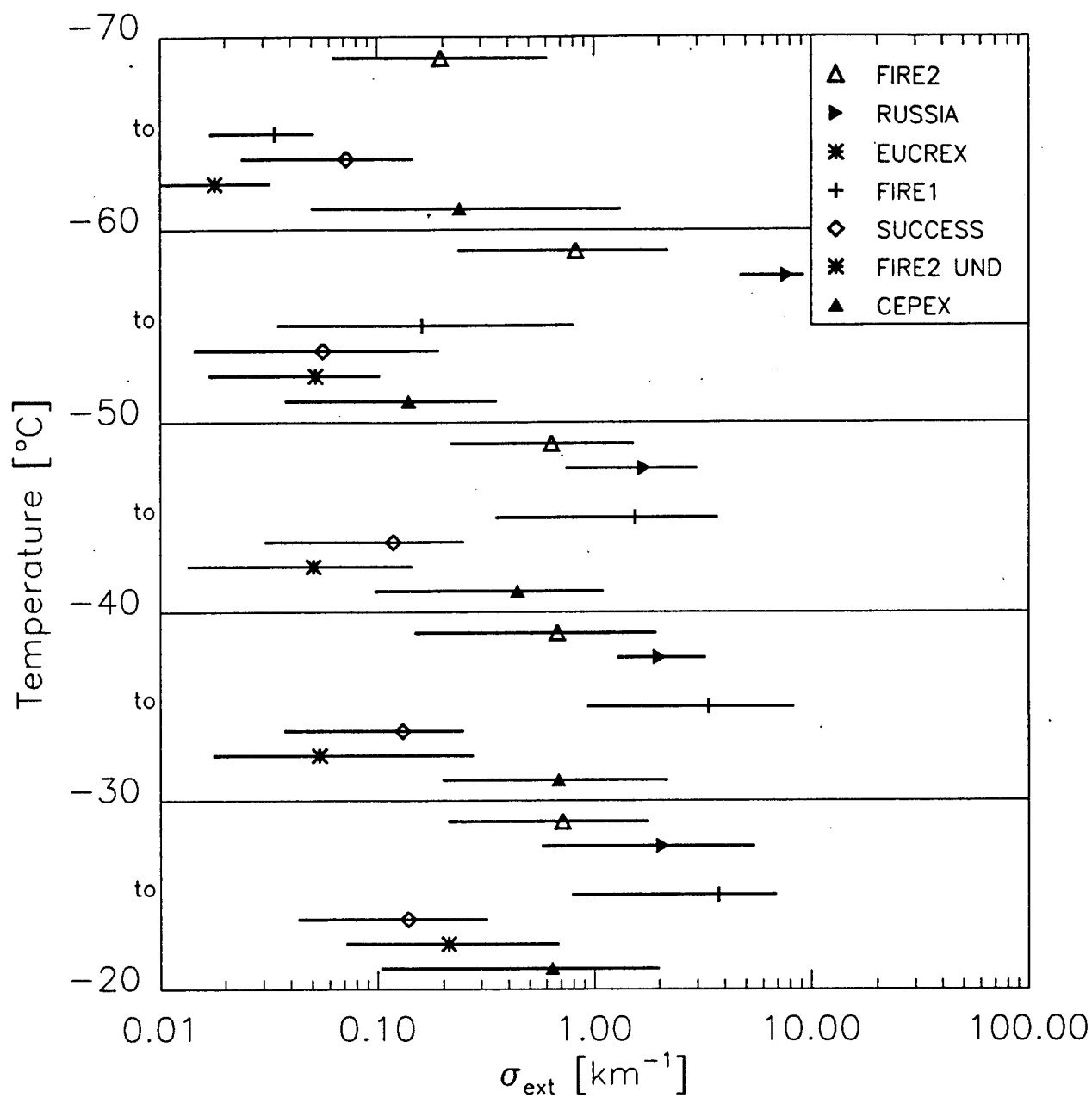




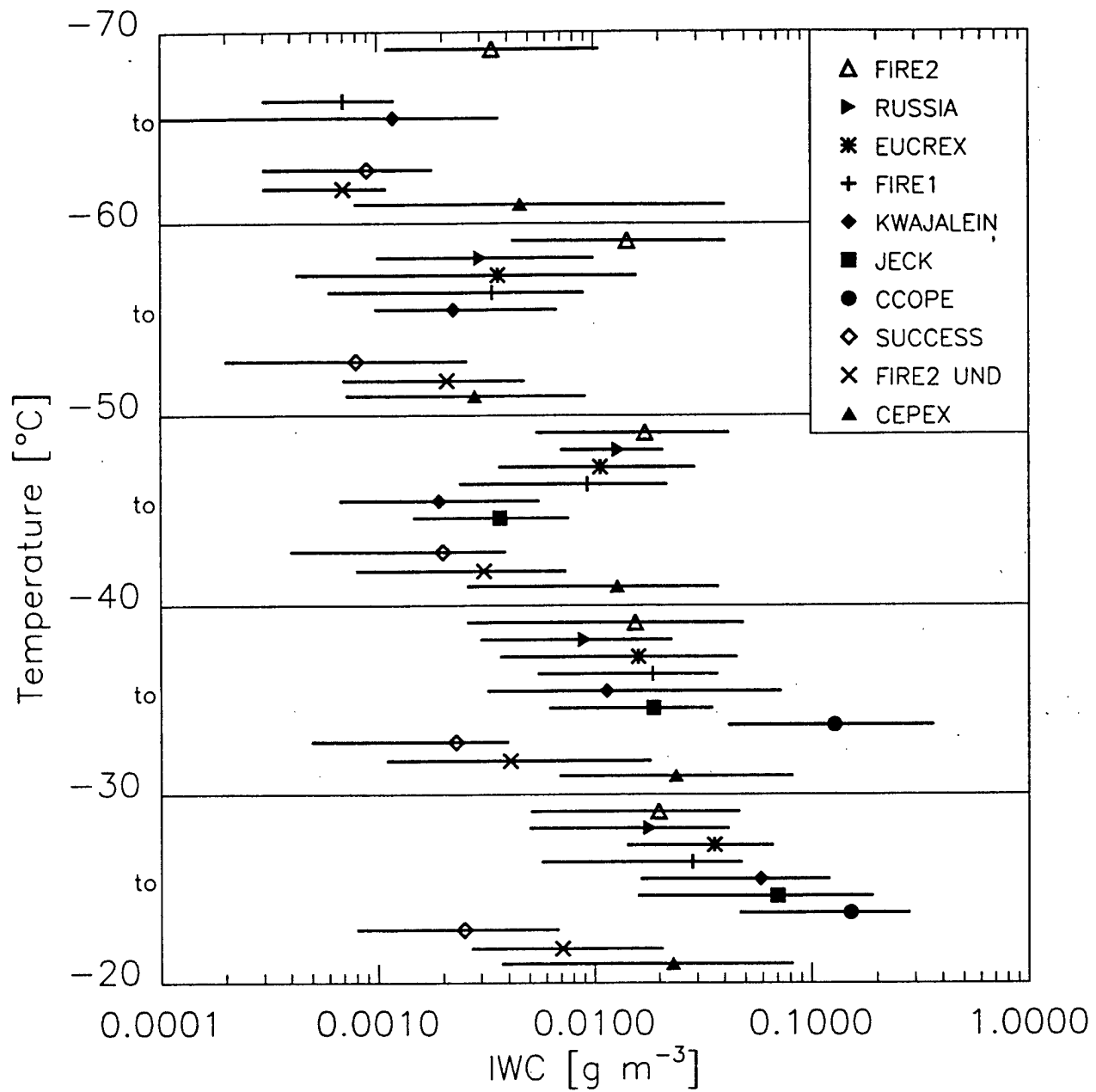
Hegmsfield and McFarquhar, Fig. 6, bottom



Hegmsfield and McFarquhar, Fig. 7, bottom



Heymsfield and McFarquhar, Fig. 8, bottom



Heymsfield and McFarquhar, Fig. 9, bottom

Table 1

Date	Crystal Sizes	%Columns	%Plates	%Compact	%Branched	%Bullet
					Spatial	Rosettes
Oct. 19 1986	D < 150 μm	70	0	30	0	0
	D > 150 μm	25	5	10	25	30
Oct. 22 1986	D < 150 μm	70	0	30	0	0
	D > 150 μm	20	5	30	35	10
Oct. 25 1986 14:36	D < 150 μm	70	0	30	0	0
	D > 150 μm	25	5	20	35	10
Oct. 25 1986 19:55	D < 150 μm	70	0	30	0	0
	D > 150 μm	20	10	40	30	0
Oct. 28 1986	D < 150 μm	15	0	85	0	0
	D > 150 μm	5	0	40	30	20
Nov. 1 1986 19:47	D < 150 μm	55	0	45	0	0
	D > 150 μm	50	15	10	20	0
Nov. 1 1986 21:01	D < 150 μm	75	0	25	0	0
	D > 150 μm	40	25	15	15	0
Nov. 2 1986	D < 150 μm	70	0	30	0	0
	D > 150 μm	20	5	40	25	10

On the Theory of Exhaust Jet Aircraft Condensation Trails

Ilia P. Mazin,¹

Central Aerological Observatory, Russian Hydrometeorological Service, Moscow, Russia

Andrew J. Heymsfield²

National Center for Atmospheric Research, P.O. Box 3000 Boulder, Colorado 80307

Ilia P. Mazin,¹ Andrew J. Heymsfield,²

Short title: CONTRAIL FORMATION CONDITIONS

Abstract. The theory of aircraft contrail formation originally developed in the 1950's is generalized. The Appleman contrail factor C is transformed into the contrail condensation parameter (CCP) which is equal $k = \frac{100}{f} \frac{C}{\epsilon}$, where epsilon is the energy loss coefficient, and $f\%$ is minimum relative humidity with respect to water at which the processes of condensation begins in a plume. Appleman's threshold formation temperatures T_{th} is estimated to increase by about 9°C . The condition $T_a < T_{th}$, where T_a is the air temperature is necessary but not sufficient for the formation of visible and in particular persistent contrails; another requirement is that the ambient vapor density is equal to or exceeds ice saturation. Some problems and objectives of further contrail investigations are discussed. When considering possible inadvertent antropogenic influence upon the climate, one of the most important task is to study the statistics of the existence of layers in the upper troposphere that are supersaturated with respect to ice.

1. Introduction

Aircraft condensation trails may be faint or rather bright, persisting in the sky for a long time. In favorable conditions they may be transformed into cirrocumulus clouds and cover a large part of the sky. In this article we will consider three aspects concerning the problem of contrail formation. The main one is determining the conditions necessary for contrail formation. This problem is considered in the next section. The second aspect refers to conditions necessary to form rather long and stable contrails – it will be discussed in the third section. The third aspect to be considered in the paper, that is, the microstructure of contrails (sizes and concentration of ice particles), and how and when contrails may be transformed into cirrocumulus clouds, is also discussed in the 3rd section. Until now, the mechanism of contrails transforming into upper layer clouds has not been discussed in the literature, though we consider it to be rather important and not very obvious. In the conclusions, the main results and some recommendations for purposes of further investigations are formulated.

2. Bases of the Theory of the 1950's

The basis of the theory which is applied to the formation of contrails was developed as early as in the 50's. By that time, it was known that contrails commonly appear in the upper part of the troposphere at rather low temperatures and consist of droplets directly behind aircraft. These droplets freeze as they move more than 100 m from the aircraft *Weickmann* [1947].

The exhaust gases contain water vapor and are warmer than the surrounding air. It was suggested that the plume may become visible during mixing with the ambient air if the mixture becomes supersaturated with respect to water and the excess water vapor condenses on the condensation nuclei supplied by the aircraft engine exhaust. *Appleman* [1953] suggested that when fuel is combusted, heat is released, and exhaust

gases including water vapor are ejected into the atmosphere and their specific amounts per unit of mass of burned fuel G (hereafter m_g , and m_v) do not depend on the engine parameters or flight regime. At further distances from the aircraft, the exhaust gases mix with the ambient air and a mass fraction of vapor (q_N) in the mixture of one part of the exhaust gases with N parts of air ($N \gg 1$) increases by value.

$$\Delta q_N = \frac{m_v}{m_g(N+1)} \cong \frac{m_v}{m_g N}. \quad (1)$$

The plume is warmer than the air by the value:

$$\Delta T_N = \frac{G}{m_g C_p N}. \quad (2)$$

Here C_p is air heat capacity at constant pressure. It follows from (1) and (2) that the relation $\Delta q_N / \Delta T_N$ does not depend on N , namely,

$$\frac{\Delta q}{\Delta T} = \frac{m_v C_p}{G} = C(K^{-1}). \quad (3)$$

Appleman named the parameter C the "Contrail factor" and following from known parameters of the fuel (kerosene) he found that $C = C_a = 3.36 \times 10^{-5} K^{-1}$. *Sadovnikov* [1955] and *Khrgian and Mazin* [1955] took into account the fact that only a part of the fuel that is released when the fuel burns exhausts into the atmosphere and is not used. In this case the equation (3) takes the form *Borovikov et al.*, [1963]; *Mazin* [1996].

$$\frac{dq}{dT} = \frac{m_v C_p}{\varepsilon G} = \frac{C}{\varepsilon}. \quad (4)$$

The parameter ε is called the *energy loss coefficient* (ELC). When developing the theory of contrails it is more convenient to consider the partial pressure of vapor in the contrail e , that relates q and pressure P by the relation: $e \approx \frac{P}{0.63} q$. Hence,

$$\frac{de}{dt} = \frac{P}{0.63} \frac{C}{\varepsilon}. \quad (5)$$

At further distances from the aircraft, the temperature of the mixture decreases and the relative humidity $f = 100 \times (e/E_w)$ ($E_w(T)$ is the water saturation vapor pressure at temperature T) increases to the maximum value $f_{\max} \geq f_a$, that is attained at a certain point $M(T_{\max})$ and drops further to relative humidity of the atmosphere f_a , if $f_{\max} > f_a$.

In Fig. 1, in the case (i), the state of the atmosphere in coordinates (T, e) is represented by the point $M^{(i)}_a(T_a, e_a)$. The state of the mixture $M^{(i)}(T, e)$ further from the aircraft changes along a straight line from p . $M^{(i)}_1$ to p . $M^{(i)}_a(T_a, e_a)$, the slope of which equals $\text{tg}\beta = \frac{P}{0.63} \frac{C}{\epsilon}$. In Fig. 1 it is shown as an example that $P_a = 300$ mb and $\text{tg}\beta = \frac{300}{0.63} 3.36 \times 10^{-5}$ (mb/K). If a straight line that passes through a point $M^{(3)}_a(T_a^{(3)}, e_a^{(3)})$ with the slope $\text{tg}\beta$ lies to the right of the water saturation curve $E(T)$, than the maximum relative humidity $f^{(3)}_{\max}$ in the mixture is attained at a certain temperature $T^{(3)}_{\max} = T_{f_1}(f_1)$. At the $p \times M(T_{f_1}(f_1))$ the straight line contacts and the curve $0.01 \times f_1 E(T)$, where $f_1 = f_{\max}$. The value f_{\max} is a increasing function of f_a and P_a and a decreasing function of T_a . Thus, when $_aT$ and P_a are preset, the maximum values f_{\max} of relative humidity are attained when $f_a = 100\%$.

Appleman [1953] in his theory of condensation trails has assumed that the new droplets or ice crystals appear in the plume only in the case if water saturation is attained in the plume ($f_{\max} \geq 100\%$). The maximum value of f is attained at the point of contact of the straight line describing the state of the mixture with the corresponding water vapor pressure curve $e_{\max} = f_{\frac{\max}{100}} E_w(T)$ (see Fig. 1). The temperature T_{th} corresponding to the point of contact is the threshold temperature above which ($T_a > T_{th}$) in the atmosphere at the humidity f_a the humidity f_{\max} cannot be reached.

Let us denote $f_{\max}(T_a, P_a, f_a)$ as the maximum relative humidity attained in the plume of exhaust gases in the process of its mixing with the ambient air, the temperature of which is T_a , pressure P_a , and humidity f_a . The maximum value f_{\max} is reached at the point of tangent of a straight line that describes the state of the mixture with the corresponding curve of relative humidity $e_{\max} = 0.01 \times f_{\max} E_w(T)$ (see Fig. 1).

Temperature T_{th} corresponding to the tangent point is the threshold temperature. If the temperature of the atmosphere $T_a > T_{th}$, and humidity is equal to f_a , then the humidity f_{max} in the mixture cannot be attained. If $f_a = 100\%$ the threshold temperature is a maximum that is $T_{th}(f_a = 100) = T_{fmax}(100)$. If $T_a > T_{100}$ then water supersaturation in the plume is not attained ($f_{max} < 100$), and condensation (and hence, the appearance of contrails) is impossible by definition. We denote as $T_{100}(P_a, f_a)$ the maximum air temperature at which 100% of relative humidity with respect to water is still reached when the air pressure is P_a and relative humidity is f_a . That is

$$f_{max}(P_a, T_{100}, f_a) = 100\%. \quad (6)$$

The value $T_{100}(P_a, 100)$ is found from the equation

$$\left. \frac{dE(T)}{dT} \right|_{T=T_{100}(P_a, 100)} \frac{P_a}{0.63} \frac{C}{\varepsilon} \quad (7)$$

Here $E(T)$ is saturated pressure of water vapor at temperature T . Having found from (7) the value of $T_{100}(P_a, 100)$, we may easily find the maximum temperature $T_{100}(P_a, f_a)$, above which in the atmosphere at pressure P_a and humidity f_a , condensation in the plume cannot occur ($f_{max}(T_a, f_a) < 100\%$ if $T_a > T_{100}(P_a, f_a)$). In fact, $\Delta T = T_{100}(P_a, 100) - T_{100}(P_a, f_a)$ is found from the relation (8), where $e_a = 0.01 f_a E(T_a)$, and $\text{tg} \beta = \frac{P_a}{0.63} \frac{C}{\varepsilon}$.

$$e_a + \text{tg} \beta \Delta T = E(T_{100}(P_a, 100)), \quad (8)$$

The diagram in Fig. 2 shows the results of calculations with equations (7) and (8) when $C = C_a = 3.36 \cdot 10^{-5} K^{-1}$. In the legend of Fig. 2 it is shown how to apply the diagram with any value of the parameter C , other than C_a . To illustrate how the values of threshold temperature T_{100, f_a} depend on C , the values T_{100, f_a} when $C = 7 \cdot 10^{-5} K^{-1}$ are also shown in Fig. 2 (dashed lines). It is seen that twofold increase of C leads to higher threshold temperatures by approximately 9°C .

Let us recall that the theory presented is based on the assumption that vapor condensation in the contrail starts at attaining 100% humidity with respect to water. Special experiments made in the nineties *Shumann et al.*, [1996] have shown that exhaust gases contain great quantities of solution droplets and soot particles covered with sulfuric acid. Water vapor starts to condense on the particles of this kind far before reaching 100% humidity with respect to water. Even in the atmosphere the process of vapor condensation may start with the humidity $f < 100\%$ *Heymsfield and Miloshevich* [1995]. Evidently if the process of vapor condensation in the plume starts when $f < 100\%$ the beginning of vapor condensation leads to the increase of threshold temperature, that is, $T_f(P_a, f_a) > T_{100}(P_a, f_a)$.

The above theory may be generalized for the case when the process of vapor condensation in the plume starts at an arbitrary humidity f . In principle, it is possible to calculate the maximum humidity reached in the plume when we know the parameters of the atmosphere T_a , P_a and f_a and the value $\text{tg}\beta$ is preset. However, to find the conditions sufficient to start condensation in the plume, we may do this more simply. In fact, condition (6) for the start of condensation yields the condition:

$$f_{\max}(P_a, T_a, f_a) = f\%. \quad (9)$$

When $f = 100\%$ the value of $T_{f,\max}(P_a, 100)$ may be found from the relation (10), analogous to relation (7), that was obtained when $f_a = 100\%$.

$$\left. \frac{d(\frac{f}{100}E(T))}{dT} \right|_{T=T_f(P_a, 100)} = \frac{P_a}{0.63} \frac{C}{\varepsilon}. \quad (10)$$

From (10) it follows that

$$\left. \frac{d(E(T))}{dT} \right|_{T=T_f(P_a, 100)} = \frac{100}{f} \frac{P_a}{0.63} \frac{C}{\varepsilon}. \quad (11)$$

Thus when determining the threshold (maximum) value of the air temperature at

which water vapor condensation in the plume is still possible, decreasing the humidity at which the process of condensation starts from 100% to $f\%$, is equivalent to increasing the parameter of contrail C or decreasing the energy loss coefficient ε by $100/f$ times. In other words, if we call the parameter $k = \frac{100}{f} \frac{C}{\varepsilon}$ the *condensational parameter of a contrail* (CPC), then the decrease of f is equivalent to a corresponding increase of the CPC. According to the latest data *Detwiler*, [1996] $C/\varepsilon \cong 5 \times 10^{-5} K^{-1}$, and, say, when $f = 70\%$, CPC is equal to $k = \frac{100}{f} \frac{C}{\varepsilon} \cong 7 \times 10^{-5} \times K^{-1}$, that leads to the increase of the threshold temperature (as it follows from the diagram in Fig. 2) by approximately $9^\circ C$ as compared to Appleman's values for $k = C_a$.

3. Formation of Visible Contrails

The theory developed for a preset pressure P_a and humidity f_a permits us to determine the temperature conditions when water vapor condensation in the plume is possible. In order that the plume becomes visible, this condition is necessary but not sufficient. The plume may be visible if the optical thickness of the mixture is sufficiently large. The optical thickness of the contrail depends both on the water content and on the particle sizes. The combustion of 1 kg of fuel forms 0.1–1 g of soot particles with diameters of 0.01 to 0.1 μm *Schumann et al.*, [1996]. Hence, $10^{14} - 10^{16}$ particles are formed for 1 kg of fuel. The particles may be covered with sulphuric acid, and droplets of the acid that were formed in the exhaust gases may serve as condensation nuclei. The sizes of the CN may be noticeable larger at a short distance from the aircraft (10–30 m) and the plume becomes visible *Schumman et al.*, [1996]; *Mazin* [1996]. We leave aside the point of droplet freezing and ice particle formation. This process is evidently rather rapid and at the distance of hundreds of meters from the aircraft, the contrail becomes ice *Weickmann* [1947].

There is much uncertainty in this problem from a quantitative viewpoint. No doubt, if the humidity in the atmosphere is below ice saturation, then growing ice

particles soon stop their growth (as estimations show, the process of aggregation is inconsequential) and the contrail is quickly visible and then quickly ceases. Such short contrails are commonly observed and they persist from seconds to minutes and cannot exert much influence on the radiation balance of the atmosphere. *Long lived visible contrails are possible only in the condition that the humidity in the atmosphere exceeds ice saturation.*

Detailed studies of the microstructure of contrails started in the 1990's. For example, *Schumann et al.*, [1996] has shown that particle concentration in the visible contrail at a distance of 1–2 km is 10^4 cm^{-3} , and their sizes in general do not exceed $0.1 \mu\text{m}$ and their optical thickness does not exceed 0.1–0.2. The water content is extremely small (no more than 10^{-4} g/m^3).

The mass water vapor excess in the plume may be estimated from the following. Let the humidity in the atmosphere be equal to ice saturation, that is $e_a = E_i(T_a)$ and ice particles grow only due to supersaturated vapor in the exhaust gases. If for 1s, M_g of fuel is combusted, then along the way V (V here is aircraft speed), $m_v M_g$ grams of water vapor are ejected into the atmosphere. For a 4-engine aircraft like the DC-8 for one kilometer distance, 10–20 kg of water vapor are ejected into the atmosphere. If we assume that the lateral size of the plume equals 100 m, then the liquid water content will be of the order of magnitude 10^{-3} g/m^3 .

Long-lived contrails with higher water contents evidently consist of larger particles and may exist, as mentioned, only when humidity in the atmosphere is higher than ice saturation. This indicates that the question of where, when and how often long existing contrails appear is really a question of where, when and how often in the upper layers of the troposphere zones with high humidity are formed (when $e_a > E_i$). At present rawinsonde measurements of the humidity at low temperatures (lower than -40°C) are now very reliable and the statistics of frequencies of occurrences of the zones with $e_a > E_i$ in the upper troposphere is absent. Preliminary evaluations *Katz and*

Mazin [1995] show for example, that in the Polar Arctic these conditions are observed approximately in 5% of cases in winter at the heights of 5.5–6.5 km, and in 2% of the cases in spring and autumn. The thickness of these layers is hundreds of meters. The given cited estimates no doubt need more thorough tests, and the problem of humidity at low temperatures remains one of the important tasks in modern aerology.

Of great importance is the aspect of the possible sizes of ice particles in the contrails. It is known that in cirrocumulus particle sizes may be tens and hundreds of microns. We may think that in the cases when cirrocumulus are formed from contrails, there are also particles of similar sizes there. V. Shugaev (private communication) has observed particles of sizes up to 100 μm in the contrail (the age of the contrail in the measured point was about 1.5 min). The evaluations show that neither aggregation nor condensation is able to provide such a rapid growth of particles, even if humidity is as high as saturation with respect to water. We think that the presence of the particles of sizes of the order of 100 μm may be related to one of the reasons: either large ice particles existed in the atmosphere before the appearance of these contrails, forming ice crystal haze which is invisible from the ground (the contrail turns out to be visible due to the presence of large quantity of small particles), or preexisting large particles are introduced into the plume with the exhaust gases, or both possibilities exist. In either case, a single contrail cannot extend over a large area. To cover the sky with upper-layer clouds, it is needed for a large number of contrails to be formed, that is, intense air traffic in the region. The SUCCESS experimental data may evidently allow us to test our concepts.

The last question worth attention is the influence of exhaust gases on the aerosol medium and, primarily, on ice nuclei concentrations. If we consider that in the upper part of the troposphere the IN concentration is small, then in principle there are situations when the humidity may be above ice saturation. Inadvertent antropogenic increase in IN concentration in the upper troposphere during civilian and military flights

decreases the probability of the presence of such layers and may stimulate increases in the cirrus cloudiness. The latter may affect radiation processes in the atmosphere and climate.

More detailed consideration of this aspect as well as the problems associated with the influence on the chemistry of the atmosphere is beyond the scope of this article.

4. Conclusion

In the present work the theory of aircraft contrails is generalized for the case when processes of condensation in the plume of exhaust gases start when the relative humidity with respect to water $f < 100\%$. Condensational parameter of the contrail k is increased by $100/f$ times. The analog to Appleman's contrail parameter C is the parameter k equaling

$$k = \frac{100}{f} \frac{C}{\varepsilon}. \quad (12)$$

The increase of k compared to $C_a = 3.36 \times 10^{-5} K^{-1}$ is $7 \times 10^{-5} K^{-1}$, ($f_1 = 70\%$, $\varepsilon = 0.7$)¹ and leads to the increase of threshold temperature of the atmosphere T_f providing yields in condensation in the plume of exhaust gases by 8–9°C.

The atmospheric conditions necessary for the appearance of visible contrails is more fixed because the plume of exhaust gases may remain invisible even when $T_a < T_f$, if the atmospheric humidity is small ($e < E_i(T_a)$) or if turbulence is large. The authors think that long existing extended contrails and moreover upper-layer clouds associated with contrails may be formed only in conditions when the humidity in the surrounding atmosphere is higher than ice saturation. In this connection, studying the statistics of the frequency of occurrence and duration of existence of layers with high humidity ($e_a > E_i(T_a)$) in the upper troposphere acquires significance when considering possible

¹With developing the aircraft the ELC ε will diminish.

antropogenic influences or climate.

The microstructure of contrails (ice particles sizes and concentration) and their growth into cirrus clouds depends on the state of the atmosphere. If there are no ice particles in the surrounding atmosphere, then in the mixture of exhaust gases and environmental air, ice particles in the first 10–20 minutes cannot be not over several tens of microns, if larger particles were originally absent in the plume. If ice particles were present in the air but their concentration was small (for instance, as in a haze invisible for a ground observer), then the particle size spectrum in the contrail may contain large (up to 100 μm and larger) particles. In-site data on the microstructure of contrails is needed for this evaluation.

In the literature, the instances of the appearance of visible contrails at temperatures above the threshold ones (defining by Appleman) were noted on occasion. The generalization of the theory expressed by the relation (12) eliminates this conflict. In order to test the theory developed here, it is necessary to have detailed and reliable experimental data from SUCCESS and future experiments.

References

- Appleman, J., The formation of exhaust condensation trails by jet aircraft, *Bull. Am. Meteorol. Soc.*, *34*, 14-20, 1953.
- Borovikov, A. M., et al., Aircraft condensation trails, *Cloud Physics*, *57b* (in Russian), 294-301, 1961.
- Detwiler, A.G., Evaluation of engine-related factors influencing contrail prediction. Final report for: *Summer Faculty Research Program* 20 pp., Phillips Laboratory, 1996.
- Heymsfield, A., and L.M. Miloshevich, Relative humidity and temperature influences on cirrus formation and evolution: Observation from wave Clouds and FIRE-II, *Journal of Atmospheric Sciences* 4302-4326, 1995.
- Katz, A.P., and I.L. Mazin, On the antropogenic influence of the Arctic atmosphere on the aerosol-cloud component (in Russian), paper presented at the International Workshop Aerosol, Cloudiness and Radiation in the Arctic Region, St. Petersburg, Russia, October 10-12, 1995.
- Khrgian, A.Kh., and I.P. Mazin, Condensation trails in the atmosphere, *Trudi CAO* (in Russian) *017*, 3-19, 1995.
- Mazin, I.P., Aircraft condensation trails. *Atmospheric and Oceanic Physics, ser. Fizika atmosfery i Okeana* *32*, 1-13, 1996.
- Sadovnikov, A.V., Causes for the formation of aircraft contrails, chimney fogs and similar phenomena, *Trudi Voennogo Gydrometeorologicheskogo Faculteta* (in Russian) *11*, 44-75, 1995.
- Schumann, U., J. Strom, et al., In-situ observation of particles in jet aircraft exhausts and contrails for different sulphur-containing fuels, *J. Geophys. Res.*, *101*, 6853-6869, 1996.

Pervomaiskaya 3, Dolgoprudny Moscow, Russia 141700.

Andrew J. Heymsfield, National Center for Atmospheric Research P.O. Box 3000
Boulder, Colorado 80307.

Received January 3, 1996; revised February 27, 1996; accepted March 31, 1996.

¹Central Aerological Observatory. Russian Hydrometeorological Service, Moscow,
Russia.

²National Central for Atmospheric Research, Boulder, Colorado.

To appear in the *Geophysical Research Letters*, 1997.

Figure 1. The lines from points $M^{(i)}_1$ to $M^{(i)}$ show changes in partial pressure of water vapor in the mixture of exhaust gases with atmospheric air that state is described by points $M^{(i)}_a$. Shown in the figure are the cases when $T^{(1)}_a < T_{100}(0)$ ($i = 1$), $T^{(2)}_a = T_{100}(f_1)$ ($i = 2$) and $T^{(3)}_a = T_{f_1}(f_2)$ ($i = 3$). In the cases (1) and (2) maximum relative humidity in the plume is equal to 100%. With the growth of $\text{tg}\beta = \frac{100}{f_1} \frac{P}{0.63} \frac{C}{\varepsilon}$ (with the growth of P or decrease of f_1 or ε) the point of contact moves to the right and the threshold temperature grows

Figure 2. Diagram for determining maximum temperature of the atmosphere at which water vapor condensation is possible in the mixture of the exhaust with the air. Solid lines according to Appleman $k = 3.36 \times 10^{-5} K^{-1}$, ($f_1 = 100\%$, $\varepsilon = 1$) dashed lines for the cases when $k = 7 \times 10^{-5} K^{-1}$, ($f_1 = 70\%$, $\varepsilon = 0.7$). Each line $\text{RH} = 0; 40; 80$ and 100% divides all the area into two parts: left one where the processes of vapor condensation with given humidity take place and the right part where vapor condensation with given humidity of the atmosphere is impossible.

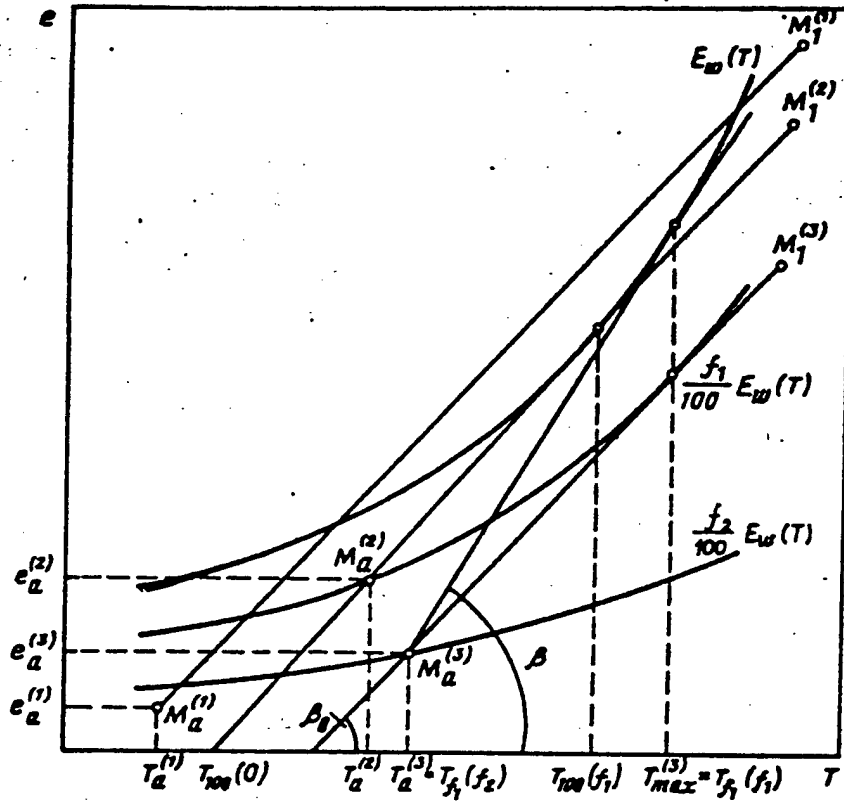


Figure 1. The lines from points $M^{(i)}_1$ to $M^{(i)}$ show changes in partial pressure of water vapor in the mixture of exhaust gases with atmospheric air that state is described by points $M^{(i)}_a$. Shown in the figure are the cases when $T^{(1)}_a < T_{100}(0)$ ($i = 1$), $T^{(2)}_a = T_{100}(f_1)$ ($i = 2$) and $T^{(3)}_a = T_{f_1}(f_2)$ ($i = 3$). In the cases (1) and (2) maximum relative humidity in the plume is equal to 100%. With the growth of $\text{tg}\beta = \frac{100}{f_1} \frac{P}{0.63} \frac{C}{\epsilon}$ (with the growth of P or decrease of f_1 or ϵ) the point of contact moves to the right and the threshold temperature grows

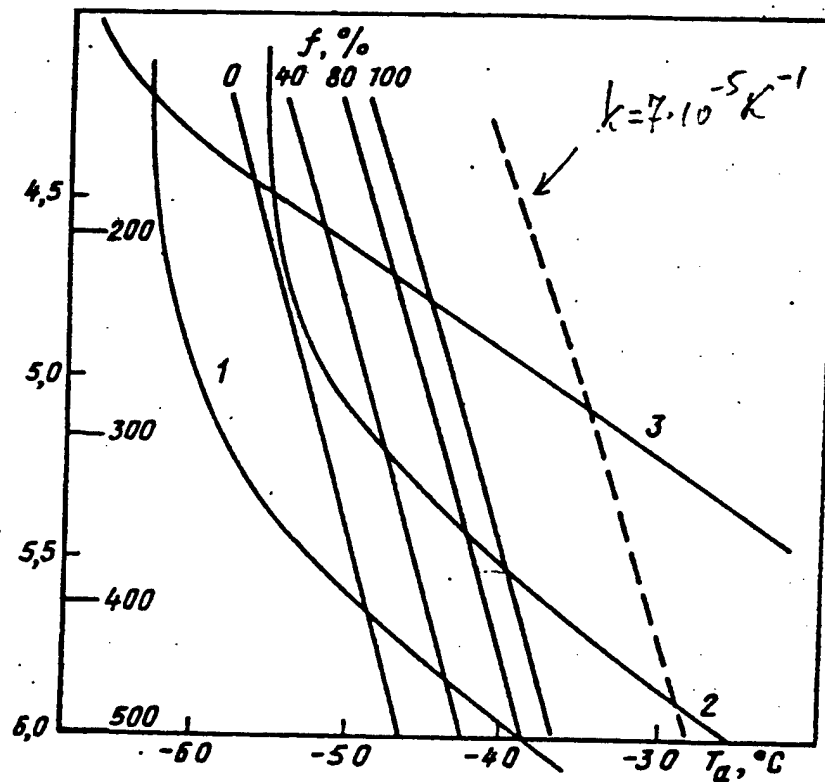


Figure 2. Diagram for determining maximum temperature of the atmosphere at which water vapor condensation is possible in the mixture of the exhaust with the air. Solid lines according to Appleman $k = 3.36 \times 10^{-5} K^{-1}$, ($f_1 = 100\%$, $\varepsilon = 1$) dashed lines for the cases when $k = 7 \times 10^{-5} K^{-1}$, ($f_1 = 70\%$, $\varepsilon = 0.7$). Each line $RH = 0; 40; 80$ and 100% divides all the area into two parts: left one where the processes of vapor condensation with given humidity take place and the right part where vapor condensation with given humidity of the atmosphere is impossible.